

**DESIGN AND OPTIMIZATION OF END MILLS WITH SPECIAL
GEOMETRIES FOR HIGH PRODUCTIVITY AND THEIR USE IN
DIFFERENT APPLICATIONS**

by

FARAZ TEHRANIZADEH

Submitted to the Graduate School of Engineering and Natural Sciences
in partial fulfillment of
the requirements for the degree of Doctor of Philosophy

Sabancı University

JULY 2021

**DESIGN AND OPTIMIZATION OF END MILLS WITH SPECIAL
GEOMETRIES FOR HIGH PRODUCTIVITY AND THEIR USE IN
DIFFERENT APPLICATIONS**

Approved by:

Approval Date:

Faraz Tehranizadeh 2021 ©

All Rights Reserved

ABSTRACT

DESIGN AND OPTIMIZATION OF END MILLS WITH SPECIAL GEOMETRIES FOR HIGH PRODUCTIVITY AND THEIR USE IN DIFFERENT APPLICATIONS

FARAZ TEHRANIZADEH

MANUFACTURING ENGINEERING PH.D. DISSERTATION, SEPTEMBER 2020

Dissertation Supervisor: Prof. Dr. ERHAN BUDAK

Machining processes, especially milling operation, are widely used in production due to high flexibility, quality, versatility, repeatability, precision and efficiency. The manufacturing industry is demanding shorter delivery times, competitive prices and higher product quality. In order to meet these requirements in a machining process, increased material removal rate (MRR), dimensional accuracy, limited form and surface tolerances during stable cutting conditions should be reached. In order to achieve these goals, lower cutting forces and stable cutting conditions are the significant constraints. In milling process, reduction in cutting forces and having stable cutting condition, improves the efficiency and part quality. For this purpose, it is important to be able to design the cutting tool geometry (end mill) with respect to the process mechanics, dynamics and geometrical properties. At this point, special tools can provide significant advantages. These tools are used rarely in industry for higher productivity purposes. Moreover, the design basis of special geometry tools is usually based on user experiments rather than process analysis in term of mechanics and dynamics. Recently, there are plenty of research works on enhancement of milling processes, higher productivity and optimization of cutting conditions. However, there are a few works focusing on the design and application of special geometry milling tools and there are significant gaps in this field.

The aim of this project is the development of design methodology and investigation of optimized geometry for special milling tools used in milling operations. The designed milling tools will be used in different kinds of milling operations and achievements will be presented within the study.

In this study, the mechanics and dynamics of the special milling tools (serrated and crest cut end mill) will be investigated in detail. The developed models will be verified by experimental studies. Considering the results from all these models, the behavior of the tools in different conditions will be examined and efficient end mills will be designed by employing optimization methods. An important contribution of the study is the development of methods for optimizing the geometry of special milling tools. Thus, for any milling condition, a specific tool can be designed and implemented. With the models to be developed in this project, the possible problems regarding the special end mills can be predicted and more systematic and efficient solutions can be offered for each operation. Moreover, the application of the special end mills in different processes and operations such as robotic milling, turn-milling, and thin-wall machining will be investigated in this study. The adaption of the obtained models to these processes can be used to predict cutting forces and the stability of the operations. These models can be used to improve the efficiency and productivity of operations by selecting proper tools.

Keywords:

Special End Mills, Serrated End Mills, Crest-Cut End Mills, Cutting Forces, Chatter, Stability, Mechanics of Milling, Dynamics of Milling

ÖZET

ÖZEL GEOMETRİLİ FREZE TAKIMLARININ YÜKSEK VERİMLİLİK İÇİN TASARIMI, OPTİMİZASYONU VE FARKLI UYGULAMALARDA KULLANIMI

FARAZ TEHRANIZADEH

ÜRETİM MÜHENDİSLİĞİ DOKTORA TEZİ, EYLÜL 2020

Tez Danışmanı: Prof. Dr. ERHAN BUDAK

Talaşlı imalat süreçlerinden olan frezeleme, yüksek esneklik, arttırılmış geometrik erişilebilirlik, tekrarlanabilirlik, hassasiyet, verimlilik ve çok yönlülük gibi avantajlarıyla çeşitli endüstrilerde yaygın kullanılan bir üretim sürecidir. İmalat sanayii daha kısa teslimat süreleri, rekabetçi fiyatlar ve yüksek ürün kalitesi talep etmeye devam etmektedir. Bu gereklilikleri yerine getirmek için frezeleme süreçlerinde yüksek Malzeme Kaldırma Oranı (MKO), hassas boyutsal doğruluk, düşük form ve yüzey toleransları kısıtları altında yüksek verimlilik elde edilmesi gereklidir. Bu hedef için en önemli sınırlamaların başında süreç sırasında ortaya çıkan yüksek kesme kuvvetleri ve tırlama titreşimleri gelmektedir. Frezeleme kuvvetlerinin azaltılması ve süreç kararlılığının arttırılması, imalat verimliliği ve parça kalitesinin arttırılmasını sağlayacaktır. Bu amaca ulaşabilmek için kesici takım geometrisinin ilgili sürecin mekanik, dinamik ve geometrik şartlarına göre tasarlanması büyük önem taşımaktadır. Bu noktada özel geometrili frezeleme takımları önemli avantajlar ve fırsatlar sunabilir. Endüstride bu yönde uygulamalar olsa da hem kısıtlıdır hem de süreçlerinin analiz ve modellenmesi yoluyla tasarım yerine tecrübeye dayalı yöntemlerle tasarım esas alınmıştır. Günümüze kadar frezeleme süreçlerinin iyileştirilmesi, yüksek verimli kesme koşullarının bulunması için çok sayıda çalışma yapılmıştır ancak özel geometrili freze takımlarının tasarımı ve uygulanması konusundaki çalışmaların sınırlı kaldığı, literatürde ve uygulamada önemli boşluklar olduğu görülmektedir.

Önerilen bu projenin amacı, yüksek imalat performansına ulaşabilmek yolunda önemli bir potansiyele sahip özel geometrili frezeleme takımlarının eniyi tasarımı için yöntemler geliştirilmesidir. Tasarlanan takımlar, çeşitli frezeleme süreçlerinde uygulanarak elde edilen kazanımlar gösterilecektir.

İlk adım olarak özel frezeleme takımlarının (kaba frezeleme ve crest-cut takımlar) mekaniği ve dinamiği detaylı bir şekilde incelenecektir. Geliştirilen modeller deneysel çalışmalarla doğrulanacaktır. Tüm bu modellerden elde edilen sonuçları kullanılarak takımların değişik koşullardaki davranışları incelenecektir ve eniyileme yöntemleri kullanarak verimli takımlar tasarlanacaktır. Önerilen projenin önemli bir özgün katkısı, bu takımların geometrilerinin eniyi tasarımı için yöntemlerin geliştirilecek olmasıdır. Böylece değişik frezeleme koşullarına uygun özel takımlar tasarlanabilecek ve uygulanabilecektir. Projede geliştirilecek olan modeller sayesinde özel takımların kullanılması sırasında ortaya çıkabilecek problemler de önceden tahmin edilebilecek ve değişik uygulamalar için daha sistematik ve verimli çözümler elde edilebilecektir.

Ayrıca, bu çalışmada robotik frezeleme, torna frezeleme ve ince duvar işleme gibi farklı proses ve operasyonlarda özel parmak frezelerin uygulamaları araştırılacaktır. Elde edilen modellerin bu işlemlere uyarlanması, kesme kuvvetlerinin ve operasyonların kararlılığının tahmin edilmesinde kullanılabilir. Uygun takımlar elde edilen modellerin yardım ile seçilerek, operasyonların verimliliği artırılabilir.

Anahtar Kelimeler:

Özel Parmak Frezeler, Tırtıklı Parmak Frezeler, Crest-Cut Parmak Frezeler, Kesme Kuvvetleri, Chatter, Stabilite, Frezeleme Mekaniği, Frezeleme Dinamiği

ACKNOWLEDGEMENTS

First and foremost, I would like to express my sincere appreciation to Dr. Erhan Budak, my research supervisor, for helping me follow my study in MRL and for his vital advice, guidance, and support throughout my graduate study. Words can neither qualify nor quantify the role he has on my life. I appreciate him for not only being my supervisor but also for behaving like one of my family members, and his support is valuable for me during my life in Turkey. It has been a great pleasure and privilege to be his student.

I would also like to thank the members of my committee: Dr. Emre Özlü, Dr. Bekir Bediz, Dr. Orkun Özşahin, and Dr. Umut Karagüzel for their excellent comments.

Zahra, my love, has always been emotional support during the difficult moments of my Ph.D., without her spiritual support, this journey would not have been possible. She always is my driving force in my academic career since 2005, and I never can be in this position without her.

It has been a pleasure to work in the Manufacturing Research Laboratory in a world-class environment. I want to express my gratitude to all of my colleagues, including past members of MRL, whose cumulative knowledge was significantly utilized throughout the dissertation. It was a priceless opportunity for me to work with amazing people from different cultures. I would like to thank Kaveh Rahimzadeh, Arash Ebrahimi, Milad Azvar, Yaser Mohammadi, Esra Yüksel, Hamid Jamshidi, Amin Bagherzadeh, Hayri Bakioğlu, Mert Gurtan, Mehmet Albayrak, Samet Bilgen, Gozde Bulgurcu, Turgut Köksal, Hassan Yaqoob, Mert Kocaefe and Saltuk Yıldız for their genuine friendship and support. I would also like to thank Dr. Emre Özlü, Dr. Taner Tunç, Dr. Emel Kuram, and other MRL scholars for their contributions and advice at various phases of the dissertation.

Also, I wish to acknowledge the support received from technicians of MRL and Maxima R&D: Suleyman Tutkun, Ertuğrul Sadıkoğlu, Muharrem Sedat Erberdi, , Ahmet Ergen Esmâ Baytok, Veli Nakşiler, Tayfun Kalender, Dilara Albayrak and Anıl Sonugür.

We had successfully created a great friendly atmosphere in Sabanci that made a great environment for me throughout my Ph.D. journey. Special thanks go to Sina, Ali, Naeimeh, Amin, Sahand, Vahid, Mohammadreza, Pegah, Navid, Mahsa, Meysam, Deniz, and Yigit.

Finally, I am deeply thankful to my family for their continuous and unconditional support, encouragement, love, and absolute confidence in me throughout my life. My dear mother, Asiyeh, my father, Khosrow, and my sister, Aysan, I am grateful to have you all. Also, I appreciate the kindness and support of Jalil Barzegar, Akram Talebi, Ali Barzegar, and Farzin Mehrjou, who are the reason for my happiness and motivation in my life.

*To My Best Friend,
My Favorite Collaborator,
My Wife,
Zahra*

TABLE OF CONTENTS

ABSTRACT.....	iv
ÖZET.....	vi
ACKNOWLEDGEMENTS.....	viii
TABLE OF CONTENTS	1
LIST OF TABLES	4
LIST OF FIGURES.....	5
1. INTRODUCTION.....	9
2. LITERATURE REVIEW	12
2.1. Milling Force Models.....	13
2.2. Modeling of Chatter Stability.....	14
2.3. Special End Mills.....	16
3. CREST-CUT END MILLS	20
3.1. Geometry of Crest-cut End Mills	20
3.1.1. Wavy Edge Geometry	21
3.1.2. Local oblique angle.....	23
3.2. Force Modelling of Crest-cut End Mills	25
3.2.1. Chip Thickness Calculation.....	26
3.2.2. Total Forces in x, y, and z Directions	26
3.2.3. Experimental Verification of Force Model	27
3.3. Chatter Stability of Crest-cut End Mills.....	30
3.3.1. Semi Discretization Method for Delayed Differential Equations.....	31
3.3.2. Chatter Stability	37
3.3.3. Experimental Verification	43
3.4. Stability Analysis Based on Crest-cut Tools Geometry.....	47

3.4.1.	Effects of Edge Wave Shape on Chatter Stability	48
3.4.2	Selection of Optimal Geometry for Crest-cut Tools.....	51
3.5.	Conclusions	54
4.	SERRATED END MILLS	56
4.1.	Geometry of Serrated End Mills.....	56
4.1.1.	Discretized End Mill Envelope Geometry	57
4.1.2.	Case1: Cylindrical End Mills.....	58
4.1.3.	Case 2: Tapered End Mills	59
4.1.4.	Case 3: Ball and Round End Mills.....	60
4.1.5.	Local Radius	60
4.1.6.	Sinusoidal Serration	61
4.1.7.	Circular Serration.....	64
4.1.8.	Trapezoidal Serration Form.....	65
4.1.9.	Edge Point Position Vectors	67
4.1.10.	Axial immersion angle.....	68
4.1.11.	Local rake and oblique angles.....	69
4.2.	Force Model of Serrated End Mills	71
4.2.1.	Uncut Chip Thickness Calculation	72
4.2.2.	Total Forces in x, y and z Directions	75
4.2.3.	Experimental Verification	76
4.3.	Serration Parameters Effects on The Cutting Forces and Optimization	77
4.3.1.	Effects of Local Rake and Oblique Angles	78
4.3.2.	Experimental Verification of the Effect of Phase Shift Direction	79
4.3.3.	Optimization of Serration Wave Parameters	81
4.3.4.	Genetic Algorithm.....	82
4.3.5.	Results of Optimization.....	84
4.3.6.	Efficiency of Optimization in Different Conditions	87
4.3.7.	Effects of Cutting Parameters on Optimum Serration Shape	90
4.4.	Chatter Stability of Serrated End Mills.....	91
4.5.	Conclusions	94

5. APPLICATION OF SPECIAL TOOLS IN DIFFERENT PROCESSES.....	96
5.1. Special End Mills in Robotic Milling	96
5.1.1. Optimization of Variable Pitch Tools for Robotic Milling	97
5.1.2. Case Study	104
5.1.3. Application of The Crest-cut End Mills in Robotic Milling	110
5.2. Application of Special Tools in Thin Wall Machining.....	112
5.2.1. Case Study: Thin-wall milling.....	113
5.3. Application of Serrated End Mills on Turn-Milling Process	119
5.3.1. Force Calculation of Turn-Milling with Serrated Tools	119
5.3.2. Experimental Verification	120
5.4. Conclusions	122
References.....	124

LIST OF TABLES

Table 3.1. Material database for Al7075-T6 Alloy.....	28
Table 3.2. Tool and process parameters in cutting force experiments	28
Table 3.3. Statical comparison of the prediction and experimental results.....	30
Table 3.4. Modal parameters of the system used in the chatter test of the crest-cut tool	44
Table 3.5. Crest-cut end mill parameters in the chatter test	44
Table 4.1. Tool and process parameters in experiments.	76
Table 4.2. Tool parameters for tests of phase shift effect.....	80
Table 4.3. Process and corresponding optimum end mill parameters.....	84
Table 4.4. Optimum tools with different serration types for same condition.....	87
Table 4.5. Modal parameters of the investigated system	92
Table 5.1 Model parameters of the robot	104
Table 5.2. Modal parameters of the thin-wall.....	114
Table 5.3. Crest-cut end mill parameters in the chatter test	115
Table 5.4. The geometrical parameters of the end mill used in experiments	121
Table 5.5. Cutting parameters of experiments	122

LIST OF FIGURES

Figure 1.1. Different types of special end mills.....	10
Figure 3.1. Wavy edge of crest-cut end mill and axial elements.....	21
Figure 3.2. Schematic and unfolded view of a sample crest-cut end mill.....	22
Figure 3.3. Local oblique angle variation along tool axis for crest-cut end mill.....	23
Figure 3.4. Local pitch angle variation along tool axis for crest-cut end mill.....	24
Figure 3.5. The schematic view of the milling with crest-cut end mill.....	26
Figure 3.6. Measured and simulated milling forces for different conditions given in Table 3.2.....	29
Figure 3.7. Approximation of the delayed term by polynomial of degree q (Tamás Insperger and Stépán 2011)	33
Figure 3.8. Approximation of the lag term with the 1st order Lagrange polynomial (Tamás Insperger and Stépán 2011).....	35
Figure 3.9. Two degrees of freedom milling dynamic system	38
Figure 3.10. Hammer test before the stability experiments with crest-cut tools	44
Figure 3.11. Schematic and unfolded view of the tool used in chatter tests.....	45
Figure 3.12. Stability lobes and chatter test results for crest-cut end mill	46
Figure 3.13. Sound Spectrum and cut surface of the different cases	47
Figure 3.16. Comparison of two different crest-cut end mill	48
Figure 3.17. Stability lobe diagrams for different edge wavelengths	49
Figure 3.18. Stability lobe diagrams for different edge wave amplitudes.....	49
Figure 3.19. Stability limit of crest-cut end mill with different shapes b) comparison of optimum crest-cut end mill ($wa=1\text{mm}$, $wl=22\text{mm}$) and variable pitch tool in 3000 rpm	52
Figure 3.20. a) Stability limit of crest-cut end mill with different shapes b) comparison of optimum crest-cut end mill ($wa=1.3\text{mm}$, $wl=31\text{mm}$) and variable pitch tool in 4000 rpm	52

Figure 3.21. a) Stability limit of crest-cut end mill with different shapes b) comparison of optimum crest-cut end mill ($wa=1.5\text{mm}$, $wl=20\text{mm}$) and variable pitch tool in 5000 rpm	53
Figure 4.1. Axial elements of the end mill	57
Figure 4.2. Tool envelop parameters for different types of end mills.....	58
Figure 4.3. Engagement of cutting teeth and workpiece, and the marks left on the cut surface.....	61
Figure 4.4. a) Parameters of sinusoidal serration b) Serration angle definition	61
Figure 4.5. Local radius variation along axis for end mill with sinusoidal serration.....	62
Figure 4.6. Schematic view of serrated (a) Flat end mill (b) Tapered end mill (c) Tapered ball end mill with sinusoidal serration	63
Figure 4.7. Parameters of circular serration waves	64
Figure 4.8. Schematic view of the end mill with circular serration	65
Figure 4.9. Parameters of trapezoidal serration waves	66
Figure 4.10. Axial immersion angle and position vector of element i on the j^{th} edge	68
Figure 4.11. Variation of axial immersion angle (κ) along tool axis	69
Figure 4.12. Local rake and oblique angles on the serration wave for each element	70
Figure 4.13. Local rake angle variation along end mill cutting edge.....	71
Figure 4.14. Differential cutting forces in axial, radial and tangential direction.....	72
Figure 4.15. Steps of chip thickness calculations	74
Figure 4.16. Chip thickness calculations for different types of serrations.	75
Figure 4.17. Setup of experiments	76
Figure 4.18. Comparison of measured and simulated cutting forces in experimental and simulation results for different conditions given in Table 1: a) 1, b) 2, c) 3 and d) 4	77
Figure 4.19. Maximum F_{xy} for different sinusoidal serration shapes	78
Figure 4.20. Serrated end mill with a) forward phase shift b) reverse phase shift and its engagement with workpiece	79
Figure 4.21. Comparison of milling forces for Tool 1 and Tool 2 (Table 4.2) with $f_t=0.05\text{mm/tooth}$ in a) x and b) y direction.....	80
Figure 4.22. Comparison of milling forces for Tool 1 and Tool 2 (Table 4.2) with $f_t=0.1\text{mm/tooth}$ in a) x and b) y direction.....	81
Figure 4.23. Genetic algorithm flowchart	82
Figure 4.24. Force Simulation Results for optimum, standard serrated and normal end	

mills for different conditions given in Table 3: a) 1, b) 2, c) 3 and d) 4	85
Figure 4.25. Difference between a) cutting forces and b) cutting areas in milling with serrated tools having forward and backward phase shifts.	86
Figure 4.26. Cutting forces with the optimum tools having different serration types given in Table 4.4 a) x and b) y direction.....	87
Figure 4.27. Plots of cutting condition parameters main effects on the efficiency of the optimization	88
Figure 4.28. Plots of cutting condition parameters interaction effects on the efficiency of the optimization.....	88
Figure 4.29. Unbalanced Force in cutting low depth of cut with high serration wave length	89
Figure 4.30. Main and interaction effects of cutting parameters on serration wave shape	90
Figure 4.31. Two orthogonal degree of freedom system and dynamic chip thickness ...	92
Figure 4.32. Comparisons of stability diagrams ($f_t=0.05\text{mm/tooth}$) a) 3000-8000 RPM b) 8000-21000 RPM.....	93
Figure 4.33. Comparisons of stability diagrams ($f_t=0.15\text{mm/tooth}$) a) 3000-8000 RPM b) 8000-21000 RPM.....	93
Figure 4.34. Stability comparison of different optimized serration profiles	94
Figure 5.1 Stability diagram for the robotic milling system.....	96
Figure 5.2. r value for 2-flute end mill with linear pitch variation.....	100
Figure 5.3. r value for 3-flute end mill with linear pitch variation.....	101
Figure 5.4. r value for 4-flute end mill with linear pitch variation.....	101
Figure 5.5. Feasible area for choosing pitch variation in 800 rpm for the 2-flute tool with the natural frequency of 40Hz.....	103
Figure 5.6. Feasible area for choosing pitch variation in 400 rpm for the 2-flute tool with the natural frequency of 40Hz.....	104
Figure 5.7. Optimum pitch variation for each spindle speed using the 4-flute end mill	105
Figure 5.8. Stability lobes for normal end mill with four cutting edge.....	106
Figure 5.9. Stability lobes for variable pitch 4-flute end mill optimized for 150RPM.....	106
Figure 5.10. Stability lobes for variable pitch 4-flute end mill optimized for 350RPM	107

Figure 5.11. Optimum pitch variation for each spindle speed using the 4-flute end mill	108
Figure 5.12. Stability lobes for variable pitch 3-flute end mill optimized for 130RPM	108
Figure 5.13. Stability lobes for variable pitch 3-flute end mill optimized for 200RPM	109
Figure 5.14. Variation of the optimum pitch for each spindle speed in different chatter frequencies.....	109
Figure 5.15. Stability lobes for crest-cut end mills with different wave amplitudes (half immersion).....	110
Figure 5.16. Stability lobes for crest-cut end mills with different wave amplitudes (0.1 immersion).....	111
Figure 5.17. Simplified model of the thin wall machining.....	113
Figure 5.18. FEM results of the modal analysis of the thin-wall a)1 st mode b)2 nd mode	113
Figure 5.19. Frequency response function of thin-wall and its real and imaginary parts	114
Figure 5.20. Stability diagram for the standard end mill (Tool 1 of Table 3.3)	115
Figure 5.21. Stability diagram for the variable pitch end mill (Tool 2 of Table 3.3) ...	116
Figure 5.22. Stability diagram for the variable pitch end mill (Tool 3 of Table 3.3) ...	116
Figure 5.23. Stability diagram for the semi-crest-cut tool (Tool 4) – 1 st mode	117
Figure 5.24. Stability diagram for the semi-crest-cut tool (Tool 4) – 2 nd mode	117
Figure 5.25. Stability diagram for the semi-crest-cut tool (Tool 4) – 1 st mode	118
Figure 5.26. Stability diagram for the semi-crest-cut tool (Tool 4) – 2 nd mode	118
Figure 5.27. The experiment setup for validating the force model of turn-milling with serrated tools	121
Figure 5.28. Comparison between test results and simulations	122

1. INTRODUCTION

Milling is one of the most important processes in the industry, used in different manufacturing sectors. The parts that can be made with milling operations include a wide variety of items. Milling can be used to create complex 3D parts in the automotive, aerospace, civil defense, medical, and energy industries, such as turbine engines, aircraft wing structures, and jet engine compressors.

The efficiency of this process decreases due to vibrations and high cutting forces occurring during the operation. These issues can lead to decreased parts quality, reduced productivity, damage to the workpiece, cutting tool, and even the machine, and can also cause various problems that affect the process. Reducing cutting depths, feed rates, etc., are the general approaches for solving these problems, however, at the cost of reduced material removal rate (MRR) and productivity. On the other hand, the production industry in today's competitive marketplace needs high-quality parts manufactured in shorter times at low costs. Therefore, decreasing MRR is not a satisfying solution to reduce cutting forces and avoid chatter vibrations in milling processes. In order to fill this gap and overcome the above problems. The use of special end mills can be an effective solution; however, special tools must be designed and selected properly, considering process conditions in order to decrease cutting forces and suppress chatter vibrations. The main idea and motivation behind this study is the development of methods to design and optimize special end mills to increase the performance in milling operations under different conditions.

Cutting tools in milling operations have different geometrical properties such as pitch and helix angles, cutting edge profile, etc. Special end mills can be classified based on these geometrical characteristics in four main categories:

- Variable pitch and/or helix end mills: end mills that have non-constant pitch angles, non-constant helix angles, or a combination of these.
- Serrated end mills: cutting tools with wavy edges which have undulations on their flank faces.

- Crest-cut end mills: cutting tools with wavy edges due to undulations on their rake faces.
- Hybrid end mills: combination of the tools listed above.

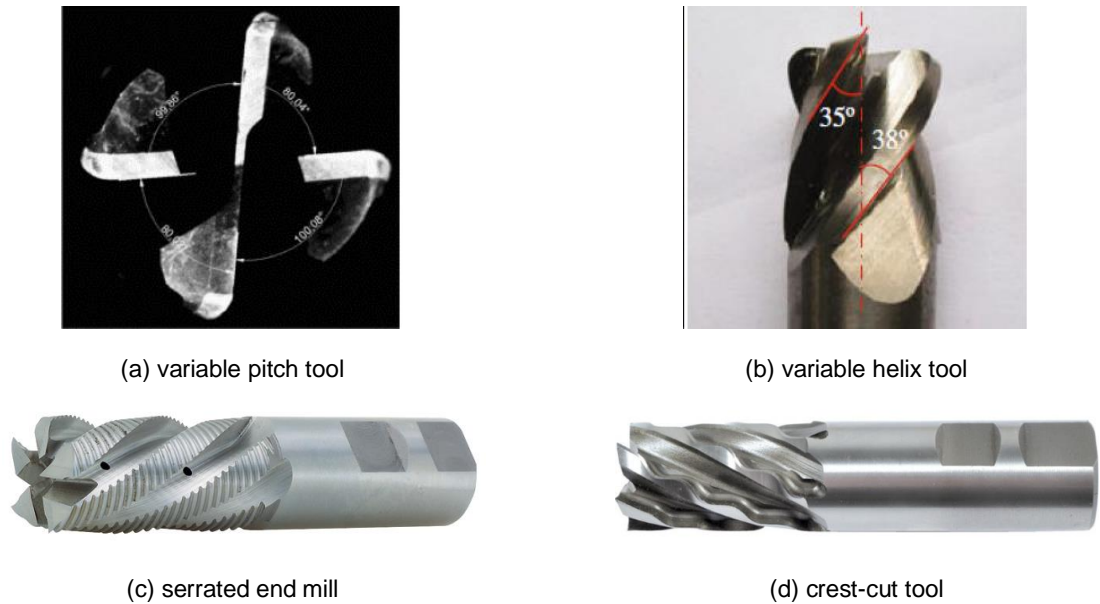


Figure 1.1. Different types of special end mills

This study mainly focuses on the modelling of mechanic and dynamic of the milling with crest-cut and serrated tools. Moreover, the effect of these tools geometry on their performance are analyzed, in order to provide helpful guidelines and information on the use and design of special end mills.

The chapter of the thesis are organized as follow:

The literature on milling geometry, milling force modeling, and chatter stability is reviewed in Chapter 2. When the method or approaches are used in the following chapters, detailed reviews are provided.

The geometry, mechanics and dynamics of the milling using crest-cut

In chapter 3, a geometric model is presented for crest-cut end mills to be used in the simulations. The mechanics of the process with crest-cut end mills is simulated and verified experimentally through force measurements. Later, the dynamics of the process are formulated and the stability diagrams are obtained using the semi-discretization method. The stability limit predictions are verified by chatter tests carried out at different

conditions. Then, the effects of the wave amplitude and length along the cutting edges on the stability limits are investigated for the first time in the literature. Based on the simulation results which are verified experimentally, guidelines are established for selection of crest-cut tool geometries for increased stability.

In chapter 4, a method to analyze mechanics of milling with different types of serrated end mills is presented. Tools with variable helix or/and pitch with different serration geometries and different types of end mills are also considered in the investigation. The geometric model of the cutter and model of the mechanics of milling with these tools to predict cutting forces are presented and verified experimentally. In the proposed method a novel and accurate way to calculate the chip thickness is presented. For the first time in the literature, effects of serration wave geometry and cutting conditions on effectiveness of serrated tools are investigated resulting in optimized serration shapes for given milling conditions. As an important factor, effects of the phase shift direction on the serration waves are also investigated. Finally, chatter stability performance of the designed optimum serrated end mills is compared with standard end mills.

The use of special end mills in various operations and processes is investigated in Chapter 5. The use of variable pitch and crest-cut tools in robotic milling, as well as their potential benefits, are discussed in the first section of the chapter. In the following section, the stability simulation model for milling flexible plates with special end mills is presented, and the effect of each tool type is investigated. In the last section, the force model of the milling with serrated end mills is modified and applied to the turn-milling operation, and the simulation results are verified experimentally.

2. LITERATURE REVIEW

Special end mills (like variable helix and/or pitch, serrated end mills, and crest-cut tools) are being used in industry relatively more often to improve the performance in milling operations. Tool manufacturers, on the other hand, are eager to expand their knowledge of these tools in order to produce unique characteristics that make them highly effective in the process. Studies and publications about special end mills, specially serrated and crest-cut tools, are limited, and there is a great gap in the modeling of the geometry, mechanics, and dynamics of these tools in the field.

Mechanics and dynamics of milling with special end mills require inter-disciplinary solutions involving fundamental theories. These issues are described and cited in related sections of the dissertation. In this section, a brief literature review about the mechanics and dynamics of milling using special tools is presented to show the state-of-the-art.

The first comprehensive and scientific work about metal cutting is published by Taylor (1907), which included different aspects of metal cutting processes. The next remarkable study in this area was done by Merchant (1944), introducing the first cutting process model. Following these pioneering studies in the field of metal cutting, numerous studies have been conducted to model metal cutting processes and forecasting different aspects of the process. Moreover, in the last decades, the number of studies on dynamics and stability of milling has significantly increased. These research efforts can be found in some basic textbooks in machining (Tobias 1965; Astakhov 1998; Koenigsberger and Tlustý 1967; Armarego and Brown 1969; Knight and Boothroyd 2019). Over time with the increasing use of machining in industry, in order to have efficient operations, the need for detailed study of machining processes has increased. Understanding details of metal cutting processes along with new techniques and technologies in CAD/CAM, monitoring, and fault detection systems can increase the efficiency and productivity of the machining industry.

2.1. Milling Force Models

Prediction of milling forces has great importance in forecasting the torque and power needed for the process. Moreover, it helps process planners to determine deflections and errors during the operation in order to compensate or reduce them. Therefore, there is a need to model the mechanics of milling to predict forces during operation. Because of the large number of variables involved in milling geometry, empirical study of milling force necessitates a large amount of data. (Hastings, Mathew, and Oxley 1980; Kahles 1987). As a result, analytical and semi-analytical milling force prediction is critical.

In initial works, the forces were predicted by only taking the geometry of the process into account (Sabberwal, A.J.P. 1961; Koenigsberger and Sabberwal 1961). The analytical force model of Sabberwal and Koenigsberger was based on the assumption that is cutting force coefficients have exponential relation with chip thickness and can be obtained experimentally. This method is known as the mechanistic model, which was used later in different studies of the milling process (Tlustý and MacNeil 1975; Devor, Kline, and Zdeblick 1980; Kline, DeVor, and Lindberg 1982; Fu, DeVor, and Kapoor 1984; Altintas, Spence, and Tlustý 1991). Another approach in the mechanistic model is considering the edge forces separately to eliminate their effects on the cutting force coefficients (Armarego and Epp 1970; Armarego and Whitfield 1985; Budak, Altintas, and Armarego 1996).

Budak et al. (1996) proposed the novel method. In this model, cutting force coefficients are determined using an experimentally obtained orthogonal cutting database. This method eliminates the necessity for the calibration of each tool geometry required in the mechanistic approach. Moreover, it can be utilized for the prediction of cutting forces with complex milling tool shapes. Non-constant edge shapes in special end mills result in variable local cutting angles (rake, oblique, chip flow, shear, and friction), which affect cutting force coefficients directly. The predicted milling force coefficients from orthogonal cutting data can be used to consider the effect of these differences on cutting forces in the suggested models (Budak, Altintas, and Armarego 1996) for any combination of these parameters. The cutting forces for ball end mills (Lee and Altintas 1996; Lazoglu and Liang 1997) and general milling cutters (Engin and Altintas 2001;

2001) were predicted using the orthogonal database and mechanistic model.

In the present study, the method presented by Budak et al. (1996) is used to predict forces in different conditions.

2.2. Modeling of Chatter Stability

Chatter is one of the major problems which appeared in machining operations. One hundred fourteen years ago, Taylor (1907) faced chatter problems and believed that it was the most obscure problem in machining. Moreover, he stated that it was probably impossible to find a way to predict stable cutting conditions. Arnold (1946) was the first one who explained the mechanism of chatter vibrations. He believed that self-inductive influence originates from the negative slope of cutting forces vs. cutting speed curve, which implies a negative damping coefficient in the equation of the motion. However, Hahn (1953) invalidated the theory of Arnold and illustrated that the relation between cutting force and cutting speed is not sufficient to explain the self-inductive behavior of chatter vibration. Later, other studies showed that the occurrence of the self-exciting chatter vibration was related to structural dynamics of machine tools and the vibration phase differences between two consecutive machined surfaces. Chatter is caused by the dynamic interaction between the machine tool and the workpiece during the chip generation process, according to the study conducted by Tlustý and Poláček (1963). They introduced the following basic equation according to their study in order to calculate the limit depth of cut (a_{lim}) for chatter stability considering cutting force coefficient (K_s) and the real part of the transfer function of the structure (G).

$$a_{lim} = -\frac{1}{2K_s Re[G]_{min}} \quad (2.1)$$

Stability lobe diagrams were later found by Tlustý et al. (1967) by taking into account the effect of spindle speed on chatter stability limits. They pointed out the stable lobes (pockets) in high spindle speeds. These lobes have a significant effect on the machining industry because they make it possible to have stable operations with a high depth of cut and cutting speeds providing higher productivity.

In milling operation, directional coefficients are not constant and vary with time as the cutting tool rotates and has multiple cutting teeth. These periodically variable coefficients make milling stability complicated in comparison with orthogonal cutting. Due to this complexity, Tlustý et al. (1981) suggested that the best way to obtain SLDs (Stability lobe diagrams) is through time-domain simulations. Minis et al. (1990; 1993) used a numerical approach considering the Nyquist criterion to obtain stability limits. The first analytical approach to find stability lobe diagrams for milling operation was proposed by Budak et al. (1995; 1998a; 1998b). In this method, time-varying dynamic cutting force coefficients are approximated by their Fourier series components, and there is no need to use iterative numerical solutions to generate stability lobe diagrams which are obtained in a fast and reliable way.

From the mathematics point of view, regenerative chatter vibration can be formulated and solved using Delay Differential Equations (DDE). The major part of the methods and techniques used to analyze Ordinary Differential Equations (ODE) can be extended and utilized in DDE problems (Michiels and Niculescu 2007; Tamás Insperger and Stépán 2011; Diekmann et al. 2012; Bellen and Zennaro 2007) as discussed before there are three main approaches to obtain stability lobe diagrams: frequency domain, time domain, and discrete-time methods. Semi discretization method is one of the discrete-time based methods which is introduced by Insperger and Stepan (Tamás Insperger and Stépán 2002; 2011). For stability analysis of delay differential equations with time-periodic coefficients, this method can be used. In this method, the past solution of the system is discretized and approximated by finite number of ODEs. Using this method, the system's principal period is divided into N discrete time increments. For these discrete time intervals, time dependent coefficient matrices are estimated with their average values and the system's infinite dimensional monodromy matrix is approximated by a finite matrix. According to Floquet theory, the system's stability is determined by the eigenvalues of the obtained approximated monodromy matrix. They also proposed the Full-Discretization Method, which discretizes both delayed terms and current-time terms (Tamas Insperger 2010).

When the system has multiple delays instead of a single one, an explicit equation for the chatter frequency and spindle speed cannot be obtained from eigenvalues equations, and the solution must be determined using numerical time domain or discrete-time solutions. In the case of the special end mills, these tools introduce multiple delays to the system

according to their non-uniform shapes. Therefore, they cannot be analyzed using frequency domain solutions. In this study, the Semi-Discretization method will be used to investigate chatter stability of milling using these special end mills and to extract stability lobe diagrams.

2.3. Special End Mills

Modeling of mechanics and dynamics of the milling process is important for forecasting cutting forces during metal cutting, power and torque requirements, workpiece quality, and chatter vibrations. Selecting proper conditions for the process plays a significant role in achieving the desired part quality. One of the important factors is the cutting tool which can affect cutting forces and chatter stability during milling. Different special end mills are used in the milling process in order to reduce cutting forces and eliminate chatter. There have been several studies on the mechanics and dynamics of special end mills and their benefits in the literature. As a first and pioneer study in the field of special end mills, Slavicek (1965) demonstrated that variable pitch cutters can suppress chatter vibration in milling. He analyzed the effect of irregular tooth pitches where Tlustý's chatter model (Tlustý and Polacek 1963) is extended to cutters with non-constant pitches. In this study, first the pitch selection criteria are defined, and it is demonstrated that the optimal pitch to improve the stability for a cutting speed depends on the chatter frequency. The results show that it is not possible to improve the stability in all speeds with specific pitch variation pattern. Opitz et al. (1966) investigated variable pitch end mills with two different pitch angles. Their simulation and test results illustrated significant improvement in the stability limit using tools with variable pitches. In his study, Vanherck (1968) studied different pitch change patterns and produced simulation results showed the effect of pitch variation on the stability limit. By considering the results of these studies in 1960s the use of milling cutters with irregular pitch was accepted as an alternative solution for increasing chatter stability of milling processes. Tlustý et al. (1982; 1983) studied the influence of special end mills such as variable pitch and serrated tools on the process dynamics in the following years. Their methods are based on pure time domain simulations which are time consuming. Due to the pioneering studies showing clear advantages of special end mills, additional works have been carried out on

different types of special end mills such as variable helix and/or variable pitch and serrated end mills in the following years. Shirase et al. (1999) demonstrated that end mills with variable pitch angles can reduce surface error. Altintas et al. (1999) presented an analytical method for predicting stability lobes in milling with variable pitch end mills. In this study, time-varying directional coefficients were transformed to time-invariant constants. Moreover, multiple regenerative time delay for variable pitch cutters is considered in the formulations. It is hard to obtain optimal pitch variations for a given condition by simulating the stability for different pitch sets, especially using time-consuming numerical time-domain solutions. Considering this problem, Budak (2003b; 2003a) proposed an analytical design method for variable pitch end mills. In this study, between the stability limit and pitch angle variations, an explicit relationship is established, leading to a simple equation for determining optimal pitch angles. The efficiency of this method was illustrated in different industrial applications. The results of studies on variable pitch tools show the importance of these tools in improving the productivity of milling operations. However, these tools have some limitations. First of all, variable pitch tools can only increase chatter stability in a narrow spindle speed range considering the chatter frequency and tooth passing frequency. Moreover, if the tooth passing frequency is high compared to the frequency of the critical mode, the optimum pitch variation also becomes high resulting in overloading of some edges and difficulties in chip evacuation. On the other hand, for low tooth passing frequencies, the optimum pitch variation angle can be very small which may bring limitations in manufacturing of these tools depending on the achievable precision (Iglesias et al. 2019).

Olgac and Sipahi (2007) adopted a mathematically novel paradigm to obtain the stability lobe diagrams analytically. This method is known as the Cluster Treatment of Characteristic Roots, CTCR. Turner et al. (2007) used average values of helix angle for calculating equivalent variable-pitch model of variable helix tools. Moreover, in this study, the optimum values for helix and pitch angles are obtained using evolutionary optimization algorithms. Dombovari and Stepan (2012) modeled chatter stability of variable helix end mills using the semi-discretization method and investigate the performance of these tools in different spindle speeds. Hayasaka et al. (2017) proposed a method to design and optimize variable helix end mills to suppress chatter vibration. Their novel method was verified by milling experiments. However, their method is applicable only on the end mills with high values of helix angles. The stability and dynamic behavior

of the variable pitch and helix tools were investigated by Çomak and Budak (2017). In this study, a new optimization method is proposed for variable pitch end mills by extending Budak's (2003a; 2003b) original method considering chatter frequency variations with the introduction of varying tooth pitches.

In the 2000s, serrated end mills were in the spotlight because of their significant effect on force reduction in the milling process. Enhancement of process stability was also demonstrated by Campomanes (202AD) in roughing process using serrated cutters with sinusoidal cutting edges. Merdol and Altintas (2002) studied the mechanics and dynamics of the serrated end mills with sinusoidal wave shape on edge. They fitted a cubic spline on the edge of the tool and used orthogonal to oblique cutting mechanics transformation in order to calculate the cutting forces. The experimentally tested model was able to predict cutting forces and stability lobes in the time domain. In the next years, they extended their model (2004) for calculating cutting forces of cylindrical and tapered end mills. Other works about the mechanics and dynamics of cutting with the serrated end mills were done in these years (Zhang et al. 2003; Junz Wang and Yang 2003) to improve the accuracy of the existing models with different methods. Later, Dombovari et al. (2010) analyzed the dynamics of serrated end mills by using the Semi-Discretization Method. In these studies, the effect of feed rate on stability limits is investigated, and results show that by increasing feed rate, stability limits are decreased as the material contact along with the serrated flutes increases. In the study of Hosseini et al. (2011), serrated cutting edges are modeled as a B-spline curve, proposing a new approach for calculating the chip thickness. Effects of serrations on milling forces and chatter stability of the process were investigated by Koca and Budak (2013). Grabowski et al. (2014) predicted cutting forces and stability limits for cylindrical end mills with sinusoidal serrations and showed that serration parameters have a significant impact on the stability limits.

As another type of special end mills, crest-cut end mills have non-constant helix angles with harmonic variations along their axis, unlike variable helix tools, which have constant helix angles on each tooth. Considering the demonstrated performance of variable pitch and helix tools in chatter suppression by the previous research, crest-cut end mills which have both effects, i.e., variable pitch and helix, integrated into their cutting edges, have the potential to eliminate chatter vibrations in milling processes. However, these tools are not widely known, unlike other special end mills. Their application in the industry has

been very limited due to very few producers of these tools with no guidance available for their design and application. Due to the continuous changes of the delay in the regeneration caused by the periodic variations in helix and pitch angles along their cutting edges, these tools can improve the process stability substantially and in wider ranges if they are designed properly. Yet, the research on these tools has been very limited, and there is no information available for the design of wave geometry. The stability of crest-cut tools was investigated by Dombovari et al. [21] for the first time in the literature by applying the semi-discretization method using distributed delays. The authors concluded that using these tools large stable lobes could be achieved at lower spindle speeds while they lose this effect at higher speeds [16]. As a technical brief to this article, Sanz et al. [22] used the previous model for investigating different case studies without experimental validations. In a recent study, T. M. Gomez et al. [23] extracted the geometry of crest-cut end mills using a 3D scanner and predicted their dynamic behavior using time-domain simulations. Although limited studies on serrated and crest-cut tools exist, they are all focused on analysis for a specific geometry. However, investigating the effect of the geometry of tools on the mechanics and dynamics of the process and choosing the best geometry of the tool for a specific application is a more critical issue. On this subject, there is a knowledge gap. Another important point to remember about special tools is that they can be used in other applications such as robotic and turn-milling processes. On this subject, no research has been done. These issues are the main motivations of this study. This thesis presents a model to predict the cutting forces and stability lobe diagrams of serrated and crest-cut end mills. Moreover, this study analyses the effect of the tool's geometry on their performance and provides a guideline to select the proper tool shape. Furthermore, the application of special tools in robotic milling, thin-wall machining, and turn-milling process are investigated in the last chapter.

3. CREST-CUT END MILLS

Crest-cut end mills are used to eliminate chatter vibrations during milling processes; however, they are not widely known and applied in the industry yet. These tools have not been investigated in detail, although they have been in the market for some time. Crest-cut tools can affect the process positively if they are designed and applied properly.

In this chapter, a geometric model is presented for crest-cut end mills. Moreover, the mechanics and dynamics of milling with crest-cut end mills are modeled and verified with experiments. Then, the effects of wavy edge shape on cutting forces and chatter stability limits are investigated, and the effectiveness of these tools in improving productivity is demonstrated.

3.1. Geometry of Crest-cut End Mills

As illustrated in Figure 3.1, unlike normal milling tools, crest-cut end mills have wavy rake surfaces. These waves usually have sinusoidal shapes causing phase differences with subsequent cutting edges. As a result, the helix angle becomes variable along the cutting edges, where pitch angles between consecutive teeth also become variable along the tool axis (as shown in Figure 3.1 A-A section). As a result, crest-cut tools can improve the dynamic performance of the process provided that their geometry is selected properly (Dombovari, Altintas, and Stepan 2010).

The first step in modeling milling with crest-cut end mills is defining the geometry of these tools. To that end, the tool is discretized into small disc elements along its axis, as shown in Figure 3.1. The position of each edge along the tool axis is calculated in addition to the local pitch and oblique angles that are obtained for each edge in every element. This is required due to the variation of oblique and pitch angles along the tool axis.

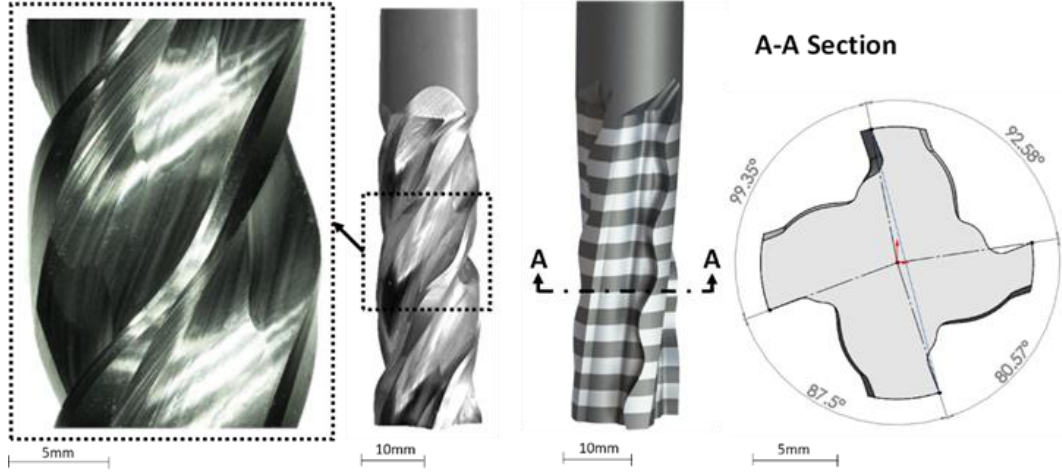


Figure 3.1. Wavy edge of crest-cut end mill and axial elements

3.1.1. Wavy Edge Geometry

In order to develop a mathematical model to represent the wavy cutting edges, the polar coordinates of an arbitrary point $\mathcal{P}_{i,j}$ defining the position in the i^{th} axial element on the edge of the j^{th} tooth are used. The angular position of each point ($\varphi_{i,j}$) in polar coordinates is a function of the accumulated pitch and lag angles ($\psi_{i,j}$):

$$\varphi_{i,j} = \Theta_j - \psi_{i,j} \quad j = 1, 2, \dots, N \quad (3.1)$$

where Θ_j is the accumulated pitch angle of the j^{th} tooth which is the function of the nominal pitch angles (p_j):

$$\begin{cases} \Theta_j = 0 & j = 1 \\ \Theta_j = \sum_{n=1}^{j-1} p_n & j = 2, \dots, N \end{cases} \quad (3.2)$$

As shown in Figure 3.2, the lag angle $\psi_{i,j}$ is defined as the angle between the tip of tooth j and the point i on the same tooth and can be calculated by the following equation:

$$\psi_{i,j} = 2\pi \frac{\text{mod}(d_{i,j}, P)}{P} \quad (3.3)$$

where P is the perimeter of the tool. $d_{i,j}$ is evaluated by conditional function in equation (3.4) which depends on the height of the edge including the straight part l_j . It is to be noted that, some of the existing crest-cut tools in the market contain a straight part l_j , as shown in Figure 3.2, for manufacturing convenience.

$$d_{i,j} = \begin{cases} (R\theta_j) - z_{i,j} \tan(\gamma_j) & \text{if } \frac{z_{i,j}}{\cos(\gamma_j)} \leq l_j \\ (R\theta_j) + u_{i,j} - \frac{A_j}{\cos(\gamma_j)} & \text{if } \frac{z_{i,j}}{\cos(\gamma_j)} \geq l_j \end{cases} \quad (3.4)$$

where R_t is the radius of the end mill, $z_{i,j}$ is the axial height of the element, γ_j is the helix angle of the j^{th} tooth, A_j is the amplitude of the edge wave of the j^{th} tooth. $u_{i,j}$ is calculated by solving the following implicit equation of rotated sine wave for the corresponding $z_{i,j}$:

$$u_{i,j} \cos(\gamma_j) + z_{i,j} \sin(\gamma_j) + \lambda_j \sin \left[\left(\frac{2\pi}{\lambda_j} \right) \cdot ((-u_{i,j} \sin(\gamma_j) + z_{i,j} \cos(\gamma_j)) + \theta_j) \right] = 0 \quad (3.5)$$

where λ_j is the wavelength on the j^{th} edge whereas θ_j represents its phase shift starting from the tip, i.e., if the phase shift is zero the sine curve starts at the tooltip (last edge in Figure 3.2).

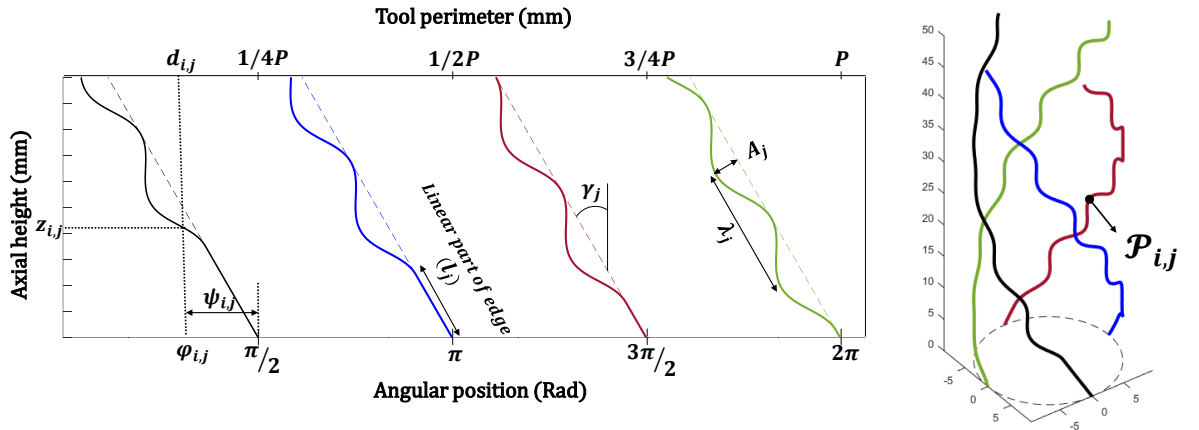


Figure 3.2. Schematic and unfolded view of a sample crest-cut end mill.

The position vector of each point on the cutting edge in Cartesian coordinates can be defined as follows:

$$\mathcal{P}_{i,j} = (R_t \cos(\varphi_{i,j})) \vec{i} + (R_t \sin(\varphi_{i,j})) \vec{j} + z_{i,j} \vec{k} \quad (3.6)$$

3.1.2. Local oblique angle

Because of the harmonically varying rake surfaces, the helix angle also varies along the cutting edges. Thus, a tooth assumes a different oblique angle within each axial element. The oblique angle has a significant effect on the cutting force coefficients (Brown and Armarego 1964; E. Budak, Altıntaş, and Armarego 1996; Aksu, Çelebi, and Budak 2016). Therefore, the local oblique angle should be identified for each element along the cutting edges. By using the geometrical relationships, the oblique angle of the i^{th} element on the j^{th} tooth ($\eta_{i,j}$) can be calculated as follows,

$$\eta_{i,j} = \tan^{-1}\left(\frac{d_{i+1,j} - d_{i,j}}{z_{i+1,j} - z_{i,j}}\right) \quad (3.7)$$

As an example, the local oblique angle variation on one of the teeth of a crest-cut end mill with 16 mm diameter and different edge wave shapes are shown in Figure 3.3 for two different nominal helix angles. As can be seen, the local oblique angle oscillates around the nominal helix angle where the oscillation amplitude depends on the edge wave geometry as defined in Equations 5 - 7. For tools with smaller nominal helix angles, the minimum local oblique angles may become too small and even be negative (Figure 3.3) depending on the edge wave geometry.

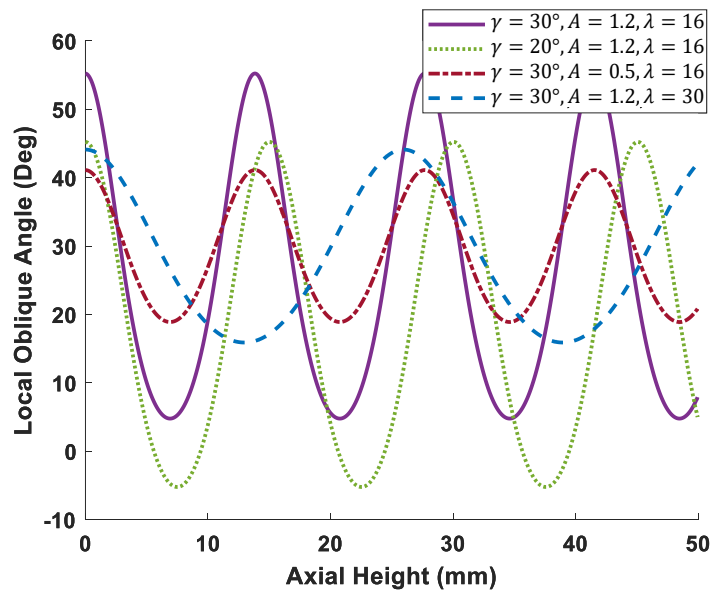


Figure 3.3. Local oblique angle variation along tool axis for crest-cut end mill

Moreover, harmonic variations of the edge profiles result in changes in pitch angles between subsequent cutting teeth at each axial height. Non-constant pitch angles affect the chip thickness in every element and should be calculated for each edge, individually:

$$\Delta\varphi_{ij} = \varphi_{ij+1} - \varphi_{ij} \quad (3.8)$$

Local pitch angle ($\Delta\varphi_{i,j}$) variation for the first tooth of a 4-fluted crest-cut end mill with 16mm diameter having different edge wave shapes and helix angles is shown in Figure 3.4 along its axis. Unlike standard milling cutters, for crest-cut tools, pitch angles vary periodically along the tool axis due to wavy edges. In Figure 3.4, the local pitch angle variation for the considered crest-cut tool is illustrated (the constant pitch angle for the four teeth tool is 90° shown with a dashed line). As can be seen, the maximum and minimum pitch angles are not symmetrical about the nominal pitch angle due to the helix. On the other hand, for a crest-cut tool with zero helix angle, the variation of pitch angle along the tool axis is symmetrical about the nominal pitch angle.

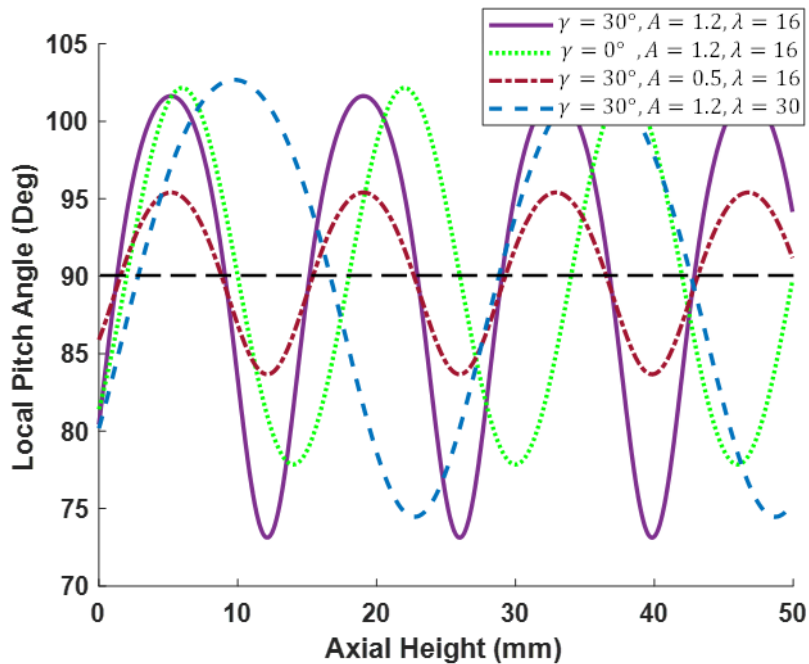


Figure 3.4. Local pitch angle variation along tool axis for crest-cut end mill

3.2. Force Modelling of Crest-cut End Mills

In this study, the linear edge force model (E. Budak, Altıntaş, and Armarego 1996) is used in order to formulate milling forces. In order to determine cutting forces for each angular increment of the tool, differential forces in tool coordinates (Figure 3.5) are calculated in each axial element (i) on each tooth (j) for the rotational position (ϕ) in one full revolution of the cutting tool as follows:

$$\begin{aligned}
 \varphi_{i,j}(\phi) &= \varphi_{i,j} + \phi \\
 dF_r(i,j,\phi) &= g(\varphi_{i,j}(\phi)) [K_{re} + K_{rc}(i,j)h_{i,j}(\phi)]dz \\
 dF_t(i,j,\phi) &= g(\varphi_{i,j}(\phi)) [K_{te} + K_{tc}(i,j)h_{i,j}(\phi)]dz \\
 dF_a(i,j,\phi) &= g(\varphi_{i,j}(\phi)) [K_{ac}(i,j)h_{i,j}(\phi)]dz
 \end{aligned} \tag{3.9}$$

where K_{rc} , K_{tc} and K_{ac} are the cutting force coefficients calculated using the oblique cutting force model together with the orthogonal cutting data (E. Budak, Altıntaş, and Armarego 1996) considering local oblique angles in each element. K_{re} , K_{te} and K_{ae} are the edge force coefficients which are usually identified from the cutting tests; however, they can also be predicted using thermo-mechanical models applied to the third zone (Erhan Budak et al. 2016). In the calculation of the force coefficient, the rake angle on the cutting edges is assumed to be constant; however, depending on the manufacturing process of these tools, it may also be variable along the cutting edges in some cases. In those cases, the local rake angle should be used in the calculation of the force coefficients (Tehranizadeh, Koca, and Budak 2019; Özlü, Ebrahimi Araghizad, and Budak 2020). $g(\varphi_{i,j}(\phi))$ is a binary function which is equal to 1 when the element is in cut (i.e. $\varphi_{start} \leq \varphi_{i,j}(\phi) \leq \varphi_{exit}$ ()) and 0 otherwise. $\varphi_{i,j}(\phi)$ is the angular position of each point on the edge when the angle of the rotation for the tool is ϕ . dz is the thickness of each axial element.

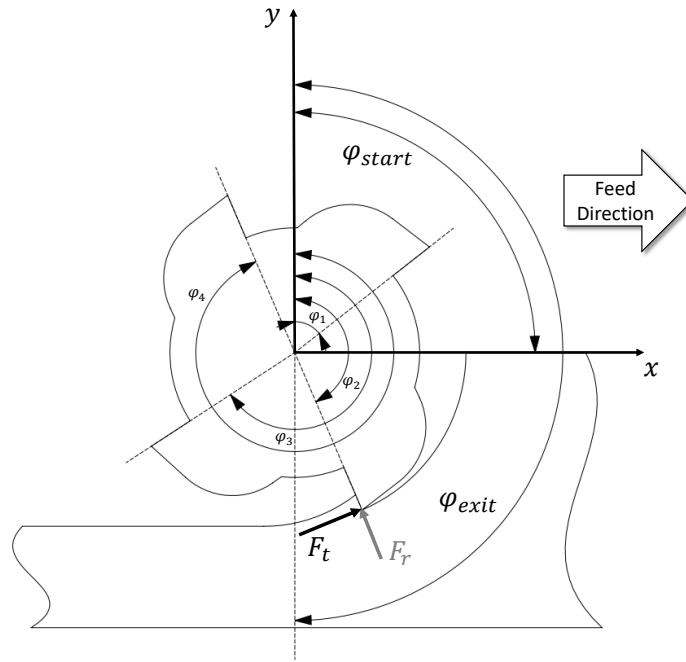


Figure 3.5. The schematic view of the milling with crest-cut end mill

3.2.1. Chip Thickness Calculation

As shown in Figure 3.5, $\Delta\varphi_{i,j}$ is different for each edge at a certain axial position and thus $h_{i,j}(\phi)$ (chip thickness) can be defined as follows:

$$h_{i,j}(\phi) = \frac{\Delta\varphi_{i,j}}{2\pi} Nf \sin(\varphi_{i,j}(\phi)) \quad (3.10)$$

where N is the number of teeth, and f is the nominal feed per tooth.

3.2.2. Total Forces in x, y, and z Directions

In order to calculate total forces, differential forces that come from each element on each edge should be summed up. Therefore, differential forces need to be transformed from tool coordinates (radial, tangential and axial) to machine coordinates (x , y , and z).

Differential forces in x , y , and z directions can be calculated by using the differential forces in tool coordinates given by equation (3.13):

$$\begin{aligned}
dF_x(i, j, \varphi) &= -dF_r(i, j, \phi) \sin(\varphi_{i,j}(\phi)) - dF_t(i, j, \phi) \cos(\varphi_{i,j}(\phi)) \\
dF_y(i, j, \varphi) &= -dF_r(i, j, \phi) \cos(\varphi_{i,j}(\phi)) + dF_t(i, j, \phi) \sin(\varphi_{i,j}(\phi)) \\
dF_z(i, j, \varphi) &= dF_a(i, j, \phi)
\end{aligned} \tag{3.11}$$

The total forces in x, y, z directions for each rotation increment can be obtained by summation of the differential forces come from each element and edge at specified increment:

$$\begin{aligned}
F_x(\varphi) &= \sum_{i=0}^a \sum_{j=1}^N dF_x(i, j, \varphi) \\
F_y(\varphi) &= \sum_{i=0}^a \sum_{j=1}^N dF_y(i, j, \varphi) \\
F_z(\varphi) &= \sum_{i=0}^a \sum_{j=1}^N dF_z(i, j, \varphi)
\end{aligned} \tag{3.12}$$

3.2.3. Experimental Verification of Force Model

Several tests have been conducted to verify the proposed force model. Cutting forces with crest-cut end mills were measured during the tests performed on MAZAK 3-axis CNC machine using a 3 component Kistler dynamometer. The work-piece material was selected as Aluminum 7075-T6. The orthogonal cutting data of this material is obtained by the method introduced in (Ozlu, Budak, and Molinari 2009) and it is shown in **Error! Reference source not found.** The experimental conditions and tool properties manufactured by KARCAN™ are shown in Table 3.2. Note that, since the wave shape of each tooth on the test cutters is similar, for the simplicity of expressions the wavelength and wave amplitude will be referred as A and λ , respectively, in the following sections. Moreover, the straight parts of the edges are zero ($l_j=0$) on the test tools.

Table 3.1. Material database for Al7075-T6 Alloy

$$T_s = 297.1 + 1.1\alpha$$

$$\beta = 18.8 + 6.7h + 0.0076V_c + 0.26\alpha$$

$$\phi_c = 24.2 + 36.7h + 0.005V_c + 0.3\alpha$$

$$K_{te} = 23.4 \frac{N}{mm}, K_{re} = 35.2 \frac{N}{mm}$$

The comparison between experimental and simulation results is illustrated in Figure 3.6. As can be seen from the figure, there is a good agreement between the milling force predictions and the measurements.

The comparison between experimental and simulation results is illustrated in Figure 3.6. As can be seen from the figure, there is a good agreement between the milling force predictions and the measurements.

Unlike conventional milling tools, due to the presence of wavy edges, the periodic behavior of the cutting forces is distorted. This is due to the fact that, on each axial element of each tooth, the phase lag between the waves of teeth causes different chip thicknesses and the wavy shapes of edges will have different start and exit angles and different tool-workpiece engagement. Therefore, the cutting forces of teeth j and $j + 1$ at the same angular position (position of edges at ϕ and $\phi + \left(\frac{2\pi}{N}\right)$ respectively) is different.

Table 3.2. Tool and process parameters in cutting force experiments

Test No.	End Mill Parameters				Process Parameters			
	Tool Dia. (mm)	No. of Teeth	Helix Angle (Deg)	Wave Shape (mm)	Spindle Speed (RPM)	Depth of Cut (mm)	Width of Cut (mm)	Feed (mm/rev.tooth)
1	16	4	30	A= 1.2 $\lambda= 16$	4500	20	4	0.05
2				A= 0.8 $\lambda= 16$	4500	10	8	0.1
3	12			A= 0.8 $\lambda= 15$	4500	15	3	0.025
4				A= 0.5 $\lambda= 10$	4500	10	6	0.05

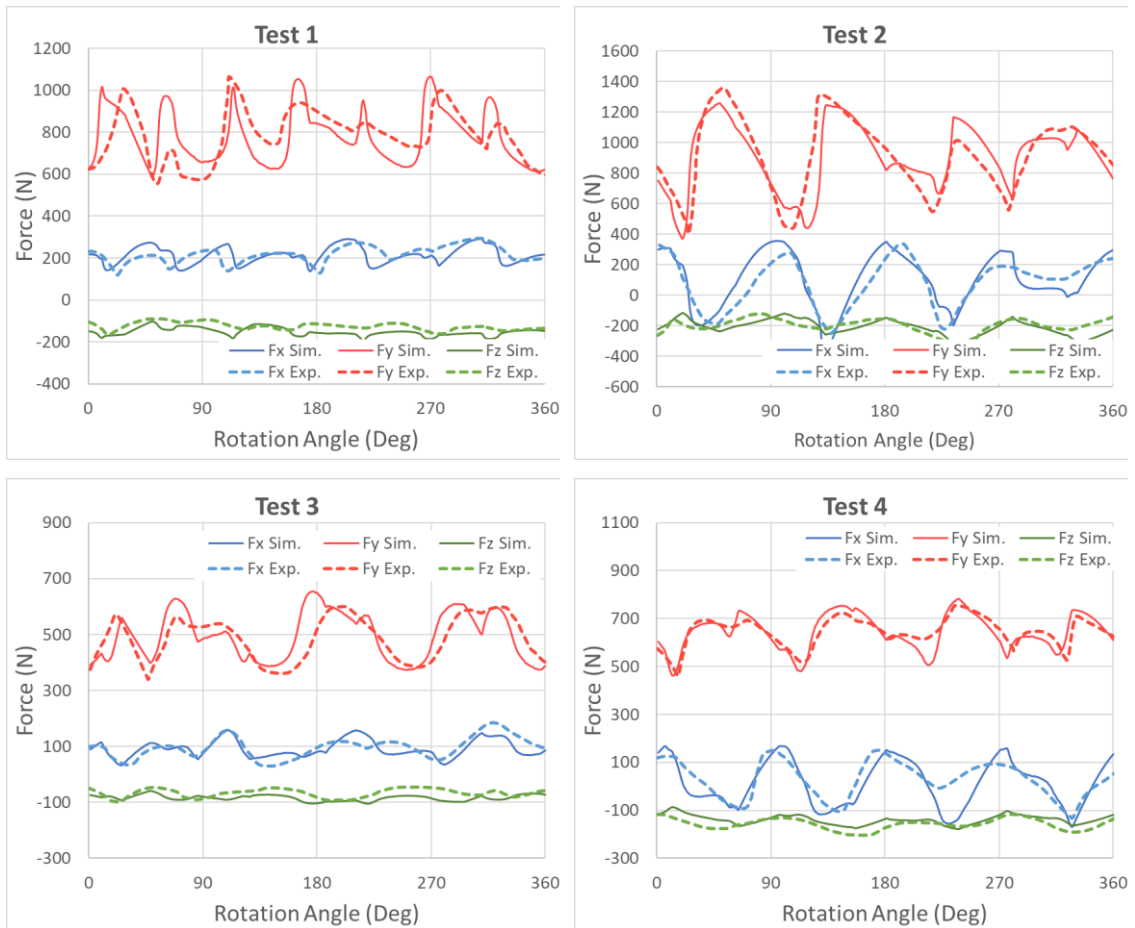


Figure 3.6. Measured and simulated milling forces for different conditions given in Table 3.2

In order to have a detailed comparison, the RMS and peak value of predicted and experimental results are compared the difference between them are listed in Table 3.3. It is seen that the average discrepancy between the peak and RMS values are 11.16% and 6.95%, respectively.

Table 3.3. Statical comparison of the prediction and experimental results.

	RMS diff.%	Peak diff.%
F_x Test 1	1.9	11.8
F_y Test 1	1.1	6.4
F_z Test 1	14.7	13.9
F_x Test 2	12.3	14.4
F_y Test 2	1.1	7.9
F_z Test 2	4.8	2.5
F_x Test 3	5.4	17.3
F_y Test 3	1.4	8.7
F_z Test 3	11.7	5.6
F_x Test 4	14.9	17.7
F_y Test 4	<1	3.5
F_z Test 4	13.2	24.2
Average	6.9	11.1

3.3. Chatter Stability of Crest-cut End Mills

In this section, the dynamics and stability of crest-cut end mills are investigated. As discussed in previous chapters, chatter vibration has a negative impact on the efficiency and quality of the milling process. Crest-cut tools can be used effectively to increase stability in the desired condition if tool parameters are selected properly considering the cutting condition.

The milling process's stability is determined by the variable chip thickness, which is a function of present and previous vibration imprints left on the cutting surface. Due to the geometry of crest-cut end mills, pitch angles between teeth are not equal, and they are variable in each axial element (Figure 3.9). As a result, delay values between teeth at each axial height are different. Therefore, unlike normal end mills, multiple delays must be taken into account during the dynamic modeling of the milling with crest-cut tools. Crest-cut end mills affect the dynamics of the process by applying perturbation in the regeneration mechanism, and they can be utilized to eliminate chatter vibration.

Chatter stability of end mills with multiple delays can be solved using the Semi-

Discretization method (Tamás Insperger and Stépán 2011). The first Order Semi-Discretization method is used in this study to analyze the stability of the process. Furthermore, the stability model is verified with milling experiments.

3.3.1. Semi Discretization Method for Delayed Differential Equations

If the delayed differential equations (DDEs) have time-periodic coefficients, investigation of the eigenvalues of the infinite-dimensional monodromy operator is required in the stability analysis. In this case, in general, stability conditions cannot be given as closed-form functions of system parameters, but numerical approximations can be used to obtain stability properties. Semi-Discretization method (SDM) is an efficient numerical method that provides a finite size matrix approximation of an infinite-dimensional monodromy matrix.

One of the basic ideas of SDM is dividing the principal period of the system is into discrete time intervals. In SDM, delay terms in each discretization step are calculated approximately with constant values or higher order polynomials considering the order of the method.

In the first step of the SDM, the principal period of the system (T) should be divided to m (resolution) discrete-time intervals:

$$\Delta t = \frac{T}{m} \quad (3.13)$$

Using the above equation, the length of each discrete time interval can be calculated.

Considering a multiple delay time-periodic equation in the form found in the following equation:

$$\dot{\mathbf{x}}(t) = \mathbf{A}(t)\mathbf{x}(t) + \sum_{r=1}^{N_D} \mathbf{B}_r(t)\mathbf{v}(t - \tau_r(t)) \quad (3.14)$$

$$\mathbf{v}(t) = \mathbf{D}\mathbf{x}(t)$$

In this equation, $\mathbf{A}(t)$ ve $\mathbf{B}_r(t)$ are time-dependent periodic coefficient matrices and N_D is the number of different delays in the system. For ease of use in the subsequent equations, for the representation of time-dependent terms in the formulation, the

following adjustments will be made.

$$\begin{aligned} X_i &\equiv X(t_i) \\ t_i &\equiv i\Delta t \end{aligned} \tag{3.15}$$

The main point of SDM is approximating time-dependent coefficients with constant values for each time interval. Also, delayed terms are approximated by linear combinations of discrete delayed values.

$$\begin{aligned} A_i &= \frac{1}{\Delta t} \int_{t_i}^{t_{i+1}} A(t) dt \\ B_{r,i} &= \frac{1}{\Delta t} \int_{t_i}^{t_{i+1}} B_r(t) dt \\ \tau_{r,i} &= \frac{1}{\Delta t} \int_{t_i}^{t_{i+1}} \tau_r(t) dt \end{aligned} \quad i = 1, 2, \dots, p \quad . \quad r = 1, 2, \dots, N_D \tag{3.16}$$

Note that the non-delayed terms in the equations are left without any change.

$$\begin{aligned} \dot{\mathbf{x}}(t) &= \mathbf{A}_i \mathbf{x}(t) + \sum_{r=1}^{N_D} \mathbf{B}_{r,i} \mathbf{\Gamma}_{r,i}^{(q)}(t - \tau_{r,i}). \quad t \in [t_i, t_{i+1}) \\ \mathbf{\Gamma}_{r,i}^{(q)}(t - \tau_{r,i}) &= \sum_{k=0}^q \left[\prod_{l=0, l \neq k}^q \frac{t - \tau_{r,i} - (i + l - dr_{r,i})h}{(k - l)h} \right] \mathbf{v}_{i+k-r_{r,i}} \end{aligned} \tag{3.17}$$

In these equations, the delay term is Lagrange polynomial interpolation with the degree of q .

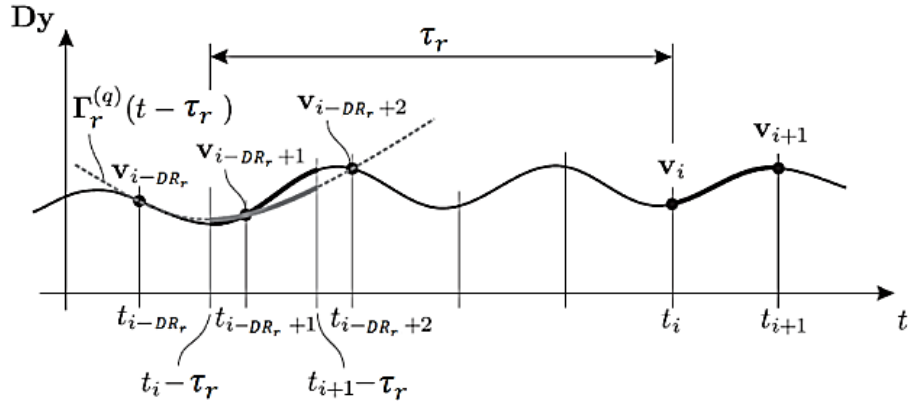


Figure 3.7. Approximation of the delayed term by polynomial of degree q (Tamás Insperger and Stépán 2011)

The delay resolution is obtained by following equation:

$$dr_{r,i} = \text{int} \left(\frac{\tau_{r,i}}{\Delta t} + \frac{q}{2} \right) \quad r = 1, 2, \dots, N_D \quad (3.18)$$

In this equation, the int function returns the integer part of the number. Thus, there are two approximation parameters: the period resolution m , which is the number of steps separating the fundamental period, and the order of the approximation of the delay term q . The application of this method can be seen in Figure 3.7.

Now, the approximated model given in (3.17) has an analytical solution over each time intervals.

$$\begin{aligned}
 x_{i+1} &= P_i x_i + \sum_{r=1}^{ND} \sum_{k=0}^q R_{r,i,k} v_{i+k-dr_{r,i}} \\
 P_i &= e^{A_i \Delta t} \\
 R_{r,i,k} &= \int_{t_i}^{t_{i+1}} e^{A_i(t_{i+1}-s)} \left[\prod_{l=0}^q \frac{s - \tau_r - (i-l-dr_{r,i})\Delta t}{(k-l)\Delta t} \right] B_{r,i} ds \\
 &= \int_0^{\Delta t} e^{A_i(\Delta t-s)} \left[\prod_{l=0}^q \frac{s - \tau_r - (l-dr_{r,i})\Delta t}{(k-l)\Delta t} \right] B_{r,i} ds
 \end{aligned} \quad (3.19)$$

Discrete map can be obtained as follow:

$$\begin{aligned}
\mathbf{z}_{i+1} &= \mathbf{G}_i \mathbf{z}_i \\
\mathbf{z}_i &= (\mathbf{y}_i \quad \mathbf{v}_{i-1} \quad \mathbf{v}_{i-2} \quad \dots \quad \mathbf{v}_{i-dr_{max}})^T \\
\mathbf{G}_i &= \begin{bmatrix} \mathbf{P}_i & \mathbf{0} & \dots & \mathbf{0} & \mathbf{0} \\ \mathbf{D} & \mathbf{0} & \dots & \mathbf{0} & \mathbf{0} \\ \mathbf{0} & \mathbf{I} & \dots & \mathbf{0} & \mathbf{0} \\ \vdots & \vdots & \ddots & \vdots & \vdots \\ \mathbf{0} & \mathbf{0} & \dots & \mathbf{I} & \mathbf{0} \end{bmatrix} + \sum_{r=1}^{N_D} \begin{bmatrix} \mathbf{0} & \mathbf{0} & \dots & \mathbf{0} & \mathbf{R}_{r,i,q} & \dots & \mathbf{R}_{r,i,0} & \mathbf{0} & \dots & \mathbf{0} \\ \mathbf{0} & \mathbf{0} & \dots & \mathbf{0} & \mathbf{0} & \dots & \mathbf{0} & \mathbf{0} & \dots & \mathbf{0} \\ \mathbf{0} & \mathbf{0} & \dots & \mathbf{0} & \mathbf{0} & \dots & \mathbf{0} & \mathbf{0} & \dots & \mathbf{0} \\ \vdots & \vdots & \ddots & \vdots & \vdots & \ddots & \vdots & \vdots & \ddots & \vdots \\ \mathbf{0} & \mathbf{0} & \dots & \mathbf{0} & \mathbf{0} & \dots & \mathbf{0} & \mathbf{0} & \dots & \mathbf{0} \end{bmatrix} \quad (3.20) \\
dr_{max} &= \max(dr_{r,i})
\end{aligned}$$

Here \mathbf{G}_i is the transition matrix connecting the states $i + 1$ and i in the time interval.

Since we have discrete time intervals, the application in (3.19) is repeated m times to obtain the monodromy matrix (Φ). This matrix connects the initial state (\mathbf{z}_0) to a state one principal period later (\mathbf{z}_p).

$$\begin{aligned}
\mathbf{z}_p &= \Phi \mathbf{z}_0 \\
\Phi &= \mathbf{G}_{p-1} \mathbf{G}_{p-2} \dots \mathbf{G}_0 \quad (3.21)
\end{aligned}$$

Φ is a finite-dimensional approximation of the actual system's infinite-dimensional operator. According to the Floquet theory, the eigenvalues of this matrix are used to analyze the system's stability. The system is unstable if the greatest eigenvalue of the monodromy matrix has an absolute value more than 1, at the stability limit if it is equal to 1, and stable if it is less than 1.

First Order SDM:

The structure of the transition matrix and the formulation of the first-order SDM will be presented in this section. At the end of this section, some important comments about applying the method to multiple delay milling processes will be explained.

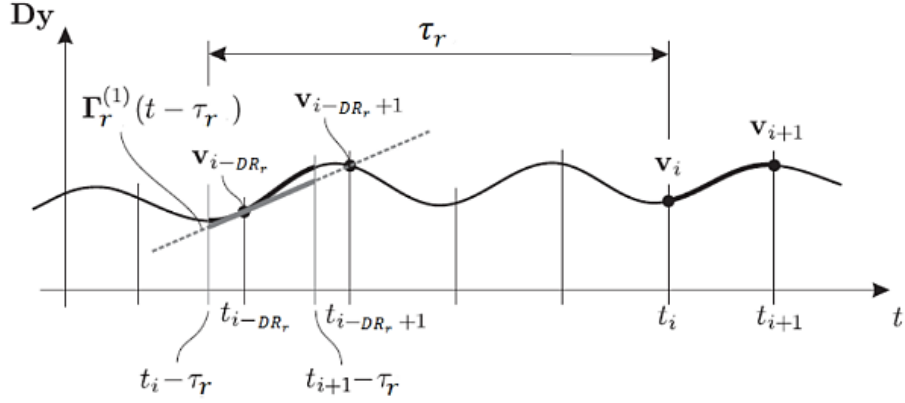


Figure 3.8. Approximation of the lag term with the 1st order Lagrange polynomial
(Tamás Insperger and Stépán 2011)

Considering equations (3.17) and (3.18) for the first-order case ($q = 1$):

$$\Gamma_{r,i}^{(1)}(t - \tau_{r,i}) = \beta_{r,i,0}(t)v(t_{i-dr_{r,i}}) + \beta_{r,i,1}(t)v(t_{i-dr_{r,i}})$$

$$\beta_{r,i,0}(t) = \frac{\tau_{r,i} + (i + 1 - dr_{r,i})\Delta t - t}{\Delta t}$$

(3.22)

$$\beta_{r,i,1}(t) = \frac{t - \tau_{r,i} - (i - dr_{r,i})\Delta t}{\Delta t}$$

$$dr_{r,i} = \text{int} \left(\frac{\tau_{r,i}}{\Delta t} + \frac{1}{2} \right)$$

For this situation,

$$\dot{\mathbf{x}}(t) = \mathbf{A}_i \mathbf{x}(t) + \sum_{r=1}^{N_D} \mathbf{B}_{r,i} [\beta_{r,i,0}(t)v(t_{i-DR_{r,i}}) + \beta_{r,i,1}(t)v(t_{i-dr_{r,i}})]$$

(3.23)

$$\forall t \in [t_i, t_{i+1})$$

$$\mathbf{v}(t_i) = \mathbf{D} \mathbf{x}(t_i)$$

Over an interval of time, the solution is calculated from the next equations:

$$\begin{aligned}
\mathbf{x}_{i+1} &= \mathbf{P}_i \mathbf{x}_i + \sum_{r=1}^{N_D} (\mathbf{R}_{r,i,0} \mathbf{v}_{i-dr_{r,i}} + \mathbf{R}_{r,i,1} \mathbf{v}_{i+1-dr_{r,i}}) \\
\mathbf{P}_i &= e^{A_i \Delta t} \\
\mathbf{R}_{r,i,0} &= \int_0^h \frac{\tau_{r,i} + (1 - dr_{r,i}) \Delta t - s}{\Delta t} e^{A_i(\Delta t - s)} ds \mathbf{B}_{r,i} \\
\mathbf{R}_{r,i,1} &= \int_0^h \frac{s - \tau_{r,i} + dr_{r,i} \Delta t}{\Delta t} e^{A_i(\Delta t - s)} ds \mathbf{B}_{r,i}
\end{aligned} \tag{3.24}$$

If A_i^{-1} exists, integrals are calculated by the next equations.

$$\begin{aligned}
\mathbf{R}_{r,i,0} &= \left[A_i^{-1} + \frac{1}{\Delta t} (A_i^{-2} - (\tau_{r,i} + (1 - dr_{r,i}) \Delta t) A_i^{-1}) (I - e^{A_i \Delta t}) \right] \mathbf{B}_{r,i} \\
\mathbf{R}_{r,i,1} &= \left[-A_i^{-1} + \frac{1}{\Delta t} (-A_i^{-2} + (\tau_{r,i} - dr_{r,i} \Delta t) A_i^{-1}) (I - e^{A_i \Delta t}) \right] \mathbf{B}_{r,i}
\end{aligned} \tag{3.25}$$

For this situation transition matrix, \mathbf{G}_i , can be calculated as follow:

$$\mathbf{G}_i = \begin{bmatrix} \mathbf{P}_i & \mathbf{0} & \cdots & \mathbf{0} & \mathbf{0} \\ \mathbf{D} & \mathbf{0} & \cdots & \mathbf{0} & \mathbf{0} \\ \mathbf{0} & \mathbf{I} & \cdots & \mathbf{0} & \mathbf{0} \\ \vdots & \vdots & \ddots & \vdots & \vdots \\ \mathbf{0} & \mathbf{0} & \cdots & \mathbf{I} & \mathbf{0} \end{bmatrix} + \sum_{r=1}^{N_D} \begin{bmatrix} \mathbf{0} & \mathbf{0} & \cdots & \mathbf{0} & \mathbf{R}_{r,i,1} & \mathbf{R}_{r,i,0} & \mathbf{0} & \cdots & \mathbf{0} \\ \mathbf{0} & \mathbf{0} & \cdots & \mathbf{0} & \mathbf{0} & \mathbf{0} & \mathbf{0} & \cdots & \mathbf{0} \\ \mathbf{0} & \mathbf{0} & \cdots & \mathbf{0} & \mathbf{0} & \mathbf{0} & \mathbf{0} & \cdots & \mathbf{0} \\ \vdots & \vdots & \ddots & \vdots & \vdots & \vdots & \vdots & \ddots & \vdots \\ \mathbf{0} & \mathbf{0} & \cdots & \mathbf{0} & \mathbf{0} & \mathbf{0} & \mathbf{0} & \cdots & \mathbf{0} \end{bmatrix} \tag{3.26}$$

The monodromy matrix can be obtained using \mathbf{G}_i and the size of this matrix will be $(2dr_{max} + 4) \times (2dr_{max} + 4)$.

The accuracy of the method is strongly dependent on the resolution (m), and higher values of m result in a larger size of the monodromy matrix. The size of the transition and monodromy matrices has a very significant effect on the computational cost of the method. Because, to approximate the infinite-dimensional monodromy matrix to a finite

matrix, the transition matrix is calculated and multiplied m times. Also, calculating eigenvalues for the larger size of the monodromy matrix is more difficult. Therefore, the m value affects the calculation time, and this issue should be taken into account.

3.3.2. Chatter Stability

The milling system's dynamics will be modeled in this part, taking into account dynamic chip thickness, dynamically changing milling forces, and the milling system's structural properties. The milling model is represented in this study using two orthogonal degrees of freedom systems in the x and y process directions (Figure 3.9).

$$\begin{aligned} m_x \ddot{x}(t) + c_x \dot{x}(t) + k_x x(t) &= F_x(t) \\ m_y \ddot{y}(t) + c_y \dot{y}(t) + k_y y(t) &= F_y(t) \end{aligned} \quad (3.27)$$

In these equations, m_x , m_y , c_x , c_y , k_x ve k_y determine the modal mass, modal damping, and modal stiffness values in the x and y directions, respectively. $\ddot{x}(t)$, $\ddot{y}(t)$, $\dot{x}(t)$, $\dot{y}(t)$, $x(t)$ and $y(t)$ are vibration acceleration, velocity, and displacement in the x and y directions, respectively. $F_x(t)$ and $F_y(t)$ are the milling forces in the x and y directions. Equation (3.28) can be rewritten as follows:

$$\begin{aligned} \ddot{x}(t) + 2\xi_x \omega_{nx} \dot{x}(t) + \omega_{nx}^2 x(t) &= \frac{F_x(t)}{m_x} \\ \ddot{y}(t) + 2\xi_y \omega_{ny} \dot{y}(t) + \omega_{ny}^2 y(t) &= \frac{F_y(t)}{m_y} \end{aligned} \quad (3.28)$$

Here ω_{nx} , ω_{ny} , ξ_x and ξ_y represent the damping ratio and natural frequency of the system's most dominant vibration mode in the x and y directions.

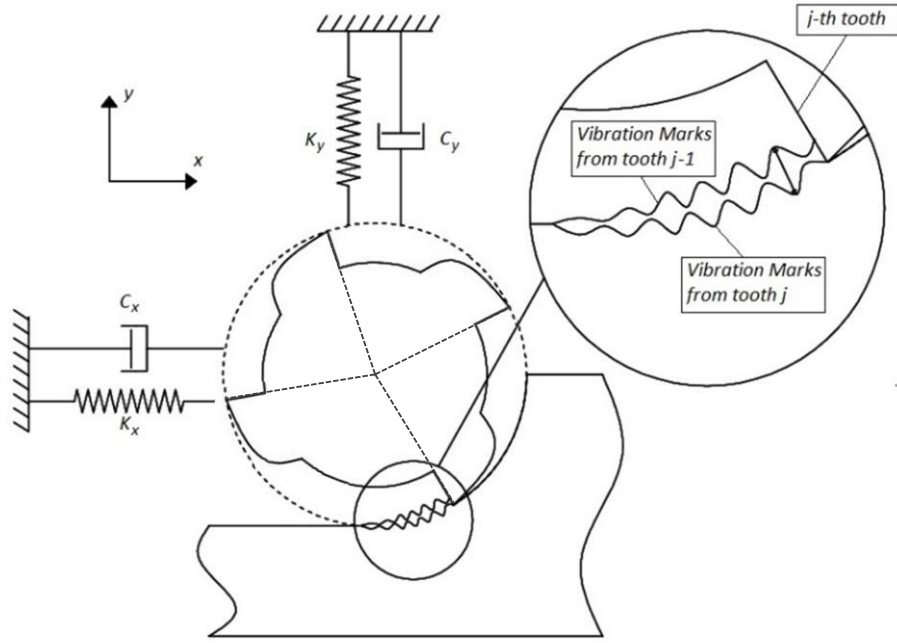


Figure 3.9. Two degrees of freedom milling dynamic system

The chip thickness varies periodically under the effect of previous vibration marks left on the surface and the present vibrations of the cutting teeth. As a result, the milling system must be considered as a delayed dynamic system. The following equations consider the influence of these vibrations on chip thickness:

$$h_{i,j}(\phi) = \left[\Delta x \sin(\varphi_{i,j}(\phi)) + \Delta y \cos(\varphi_{i,j}(\phi)) \right]$$

$$\Delta x = x(t) - x(t - \tau_{i,j}) \quad (3.29)$$

$$\Delta y = y(t) - y(t - \tau_{i,j})$$

where the time-dependent vibration amplitude differences in the x and y directions are denoted by Δx and Δy , respectively. At each axial height, $\tau_{i,j}$ shows the delay time between teeth j and $j + 1$. For each angular position of cutting teeth, the effect of vibrations on dynamic chip thickness is taken into account by considering their components in the chip thickness direction.

Considering equation (3.29), dynamic milling forces can be obtained by following

equations:

$$\begin{aligned}
dF_x(i, j, \varphi) &= -K_{rc}[\Delta x \sin(\varphi_j) + \Delta y \cos(\varphi_j)] \sin(\varphi_{ij}(\varphi)) \\
&\quad - K_{tc}[\Delta x \sin(\varphi_j) + \Delta y \cos(\varphi_j)] \cos(\varphi_{ij}(\varphi)) \\
dF_y(i, j, \varphi) &= -K_{rc}[\Delta x \sin(\varphi_j) + \Delta y \cos(\varphi_j)] \cos(\varphi_{ij}(\varphi)) \\
&\quad + K_{tc}[\Delta x \sin(\varphi_j) + \Delta y \cos(\varphi_j)] \sin(\varphi_{ij}(\varphi))
\end{aligned} \tag{3.30}$$

Since the geometry of crest-cut tools brings multiple time delays to the system, this issue should be taken into account in the model, and the obtained equations will be solved by the Semi-Discretization method. Also, in the formulation, crest-cut tools with variable pitch and/or helix tools are considered. And the effect of non-constant nominal pitch and helix angles will be investigated.

Since the delay varies along the tool axis for each tooth due to the geometry of the crest-cut end mills, their values must be calculated for each tooth and axial position. At certain axial position i , the delay for the tooth number j , $\tau_{i,j}$, can be determined using the local pitch angle $\Delta\varphi_{i,j}$ (Equation (3.8)) and the spindle speed Ω as follows:

$$\tau_{i,j} = \frac{60\Delta\varphi_{i,j}}{2\pi\Omega} \tag{3.31}$$

After determining the delay for each tooth and element, the number of discrete points that cover each time delay ($\tau_{i,j}$) is obtained as follow (Tamás Insperger and Stépán 2002):

$$\begin{aligned}
D_{i,j} &= \text{int} \left(\frac{\tau_{i,j}}{h} + \frac{1}{2} \right) \\
\mathbf{r} &= \text{unique}(D_{i,j}) \quad \forall i = 1:z \text{ and } \forall j = 1:N \\
N_D &= \text{size}(\mathbf{r})
\end{aligned} \tag{3.32}$$

The coefficients of dynamic displacement differences in the x and y coordinates are generated by rearranging the dynamic milling forces (equation (3.11)) as follows:

$$\begin{aligned}
dF_x(i, j, t) &= \Delta x (a_{xx}(i, j, t)) + \Delta y (a_{xy}(i, j, t)) \\
dF_y(i, j, t) &= \Delta x (a_{yx}(i, j, t)) + \Delta y (a_{yy}(i, j, t))
\end{aligned} \tag{3.33}$$

To take into account the geometry of the crest-cut tools in these equations, directional coefficients are calculated for all cutting teeth at each z level.

$$\begin{aligned}
a_{xx}(i, j, t, D_{i,j}) &= g(\varphi_{i,j}(t)) \left(\sin(\varphi_{i,j}(t)) (-\sin(\varphi_{i,j}(t))K_{rc} - \cos(\varphi_{i,j}(t))K_{tc}) \right) dz \\
a_{xy}(i, j, t, D_{i,j}) &= g(\varphi_{i,j}(t)) \left(\cos(\varphi_{i,j}(t)) (-\sin(\varphi_{i,j}(t))K_{rc} - \cos(\varphi_{i,j}(t))K_{tc}) \right) dz \\
a_{yx}(i, j, t, D_{i,j}) &= g(\varphi_{i,j}(t)) \left(\sin(\varphi_{i,j}(t)) (-\cos(\varphi_{i,j}(t))K_{rc} - \sin(\varphi_{i,j}(t))K_{tc}) \right) dz \\
a_{yy}(i, j, t, D_{i,j}) &= g(\varphi_{i,j}(t)) \left(\cos(\varphi_{i,j}(t)) (-\cos(\varphi_{i,j}(t))K_{rc} - \sin(\varphi_{i,j}(t))K_{tc}) \right) dz
\end{aligned} \tag{3.34}$$

Here, $a_{xx}(i, j, t, D_{i,j})$ represents the directional coefficient of the axial element i on each tooth (j) at time t in XX direction. These coefficients are grouped according to the delay value of the corresponding element and tooth D_{ij} . $\varphi_{i,j}(t)$ is the angular position of each element on each tooth at time t and it can be obtained by the following equation:

$$\varphi_{ijt} = \frac{60t}{\Omega} 2\pi + \varphi_{ij} \tag{3.35}$$

Considering obtained relations, equation (3.28) can be rewritten as follows:

$$\begin{aligned}
&\left\{ \ddot{x}(t) + 2\zeta_x \omega_{nx} \dot{x}(t) + \omega_{nx}^2 x(t) \right\} \\
&\left\{ \ddot{y}(t) + 2\zeta_y \omega_{ny} \dot{y}(t) + \omega_{ny}^2 y(t) \right\} \\
&= \begin{bmatrix} \frac{\omega_{nx}^2}{k_x} & 0 \\ 0 & \frac{\omega_{ny}^2}{k_y} \end{bmatrix} \sum_{r=1}^{r=N_D} \left[[DC_r(t)] \begin{bmatrix} x(t) - x(t - \tau_r) \\ y(t) - y(t - \tau_r) \end{bmatrix} \right]
\end{aligned} \tag{3.36}$$

$DC_r(t)$ matrix includes direction coefficient and the elements of $DC_r(t)$ are given below:

$$DC_{r,t} = \sum_{i=1}^z \sum_{j=1}^N \begin{bmatrix} a_{xx}(i,j,t,r) & a_{xy}(i,j,t,r) \\ a_{yx}(i,j,t,r) & a_{yy}(i,j,t,r) \end{bmatrix} \quad (3.37)$$

In the next step, the system (equation (3.36)) is transformed into the form of (Tamás Insperger and Stépán 2002):

$$\begin{aligned} \dot{\mathbf{X}}(t) &= \mathbf{L}(t)\mathbf{X}(t) + \sum_{r=1}^{r=N_D} \mathbf{R}_r(t)\mathbf{X}(t - \tau_r) \\ \mathbf{X}(t) &= \begin{Bmatrix} x(t) \\ y(t) \\ \dot{x}(t) \\ \dot{y}(t) \end{Bmatrix} \end{aligned} \quad (3.38)$$

In this equation $\mathbf{L}(t)$ and $\mathbf{R}_r(t)$ are time dependent periodic coefficient matrices:

$$\begin{aligned} \mathbf{L}(t) &= \begin{bmatrix} \mathbf{0} & \mathbf{I} \\ \mathbf{M}^{-1}\mathbf{D}\mathbf{C}_t - \mathbf{D} & \mathbf{C} \end{bmatrix} \\ \mathbf{R}_r(t) &= \begin{bmatrix} \mathbf{0} & \mathbf{I} \\ \mathbf{M}^{-1}\mathbf{D}\mathbf{C}_{r,t} & \mathbf{0} \end{bmatrix} \\ \mathbf{M}^{-1} &= \begin{bmatrix} \frac{\omega_{nx}^2}{k_x} & 0 \\ 0 & \frac{\omega_{ny}^2}{k_y} \end{bmatrix} \\ \mathbf{D} &= \begin{bmatrix} \omega_{nx}^2 & 0 \\ 0 & \omega_{ny}^2 \end{bmatrix} \\ \mathbf{D}\mathbf{C}_t &= \sum_{r=1}^{r=N_D} \mathbf{D}\mathbf{C}_{r,t} \\ \mathbf{C} &= \begin{bmatrix} -2\zeta_x\omega_{nx} & 0 \\ 0 & -2\zeta_y\omega_{ny} \end{bmatrix} \end{aligned} \quad (3.39)$$

$\mathbf{L}(t)$ matrix has the contributions of all directional coefficients in time t and it is independent of delay labels. On the other hand, only direction coefficients labeled r affect

the $\mathbf{R}_r(t)$ matrix.

Stability analysis of Equation (3.38) is done by the first-order Semi-Discretization method. In this method, as discussed in previous sections, the stability of the system is analyzed with an approximate monodromy matrix according to Floquet Theory. The solution at each time step depends on the state of the system in the previous time step (Tamás Insperger and Stépán 2002).

$$\mathbf{z}_{u+1} = \mathbf{B}_u \mathbf{z}_u$$

$$\mathbf{z}_u = \begin{pmatrix} \mathbf{X}_u \\ \mathbf{X}_{u-1} \\ \vdots \\ \vdots \\ \mathbf{X}_{u-m+1} \\ \mathbf{X}_{u-m} \end{pmatrix} \quad (3.40)$$

where,

$$\mathbf{B}_u = \begin{bmatrix} \mathbf{e}^{L_u \Delta t} & \mathbf{0} & \cdots & \mathbf{0} & \mathbf{0} \\ \mathbf{I} & \mathbf{0} & \cdots & \mathbf{0} & \mathbf{0} \\ \mathbf{0} & \mathbf{I} & \cdots & \mathbf{0} & \mathbf{0} \\ \vdots & \vdots & \ddots & \vdots & \vdots \\ \mathbf{0} & \mathbf{0} & \cdots & \mathbf{I} & \mathbf{0} \end{bmatrix} + \sum_{r=1}^{N_D} \begin{bmatrix} 0 & 0 & \cdots & 0 & \mathbf{R}_{r,u,1} & \mathbf{R}_{r,u,0} & 0 & \cdots & 0 \\ 0 & 0 & \cdots & 0 & 0 & 0 & 0 & \cdots & 0 \\ 0 & 0 & \cdots & 0 & 0 & 0 & 0 & \cdots & 0 \\ \vdots & \vdots & \ddots & \vdots & \vdots & \vdots & \vdots & \ddots & \vdots \\ 0 & 0 & \cdots & 0 & 0 & 0 & 0 & \cdots & 0 \end{bmatrix}$$

$$\mathbf{R}_{r,u,0} = \left(\mathbf{L}_u^{-1} + \frac{1}{h} (\mathbf{L}_u^{-2} - (\tau_{r,u} - (r_r - 1)\Delta t)\mathbf{L}_u^{-1}) (\mathbf{I} - \mathbf{e}^{L_u \Delta t}) \right) \mathbf{R}_{r,u}$$

$$\mathbf{R}_{r,u,1} = \left(-\mathbf{L}_u^{-1} + \frac{1}{h} (-\mathbf{L}_u^{-2} + (\tau_{r,u} - r_r \Delta t)\mathbf{L}_u^{-1}) (\mathbf{I} - \mathbf{e}^{L_u \Delta t}) \right) \mathbf{R}_{r,u}$$

$$\Delta t = \frac{T}{m}$$

$$T = \frac{60}{\Omega}$$

State matrices $\mathbf{L}(t)$ and $\mathbf{R}_r(t)$ depend on time-varying matrices \mathbf{DC}_t and $\mathbf{DC}_{r,t}$ that can be evaluated in each time interval (u). The time-varying milling process can be simulated

by solving a set of discrete recursive equations in each time interval. Since the process is periodic in T , it is sufficient to solve the equations in m (number of time steps) time interval.

The system's stability can be assessed by considering m intervals in the tool rotation period T , as shown below.:

$$\mathbf{z}_{i+m} = \mathbf{\Phi} \mathbf{z}_i \quad (3.42)$$

In line with the Floquet theory, if at least one eigenvalue of the transition matrix ($\mathbf{\Phi}$) has a module greater than one, there will be chatter in the system. The system will be critically stable if the greatest module is one and stable if all of the modules are less than one (Tamás Insperger and Stépán 2004).

3.3.3. Experimental Verification of Stability Model

In this part, chatter tests will experimentally verify the stability model presented to the crest cutting tools. DMU 75 5-axis machining center is used to milling of a Al7075-T6 prismatic block. A microphone is set as close to the cuttings area and the recorded sound data are analyzed using LabVIEW software to capture the sound spectrum of chatter tests. Prior to the tests, a hammer test is used to acquire the modal characteristics of the tool-holder-spindle assembly at the tool tip, and stability analysis is performed using these parameters. (Figure 3.10). CUT PRO® software was used for the hammer test.



Figure 3.10. Hammer test before the stability experiments with crest-cut tools

The modal parameters obtained for the system are shown in Table 2.

Table 3.4. Modal parameters of the system used in the chatter test of the crest-cut tool

ω_{nx} (Hz)	k_x (N/m)	ζ_x %	ω_{ny} (Hz)	k_y (N/m)	ζ_y %
711	2.65e7	3.08	509	2.41e7	4.37

The geometrical parameters of the crest-cut end mill used in the chatter tests are disclosed in Table 3.

Table 3.5. Crest-cut end mill parameters in the chatter test

R	N	γ	λ	A	l
8 mm	4	30°	16 mm	1.2 mm	0

The schematic and unfolded view of the used end mill is shown in Figure 3.11.

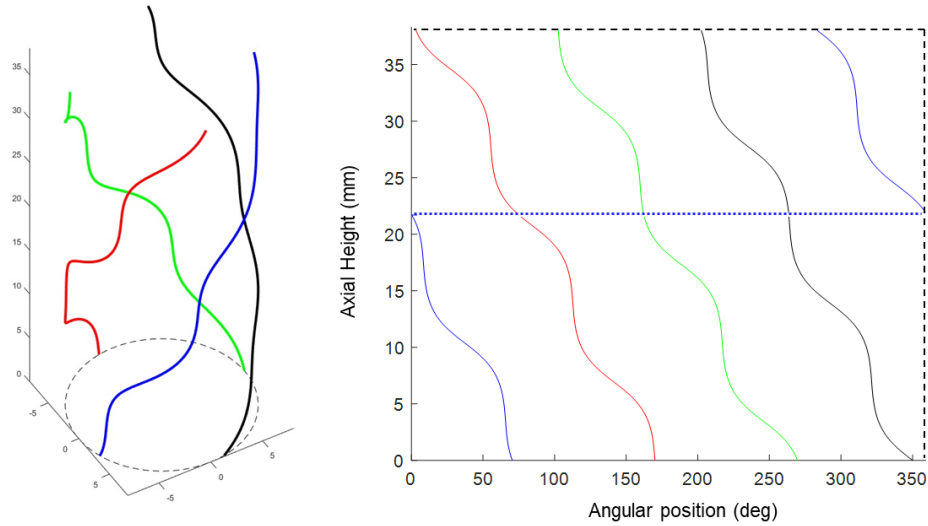


Figure 3.11. Schematic and unfolded view of the tool used in chatter tests

Half immersion milling with $0.025 \text{ mm}/(\text{rev-tooth})$ feed was applied in the chatter tests. The predicted stability diagram, together with the chatter test results, are shown in Figure 3.12. The stability diagram for a similar standard end mill is also given in the same figure, illustrating a substantial stability limit increase with the crest-cut tool. Furthermore, as it can be seen from the figure, instead of classical stability lobes for standard milling tools, crest-cut end mills provide much larger stability regions due to different delays introduced to the system as they disrupt regeneration mechanisms. Considering this advantage, crest-cut tools provide wider and higher stable regions in certain speed ranges improving productivity significantly. In higher spindle speeds, on the other hand, since the wavelength of vibrations is increased, the stabilizing effect of the crest-cut tools is reduced. These effects will be discussed in section 5 in detail.

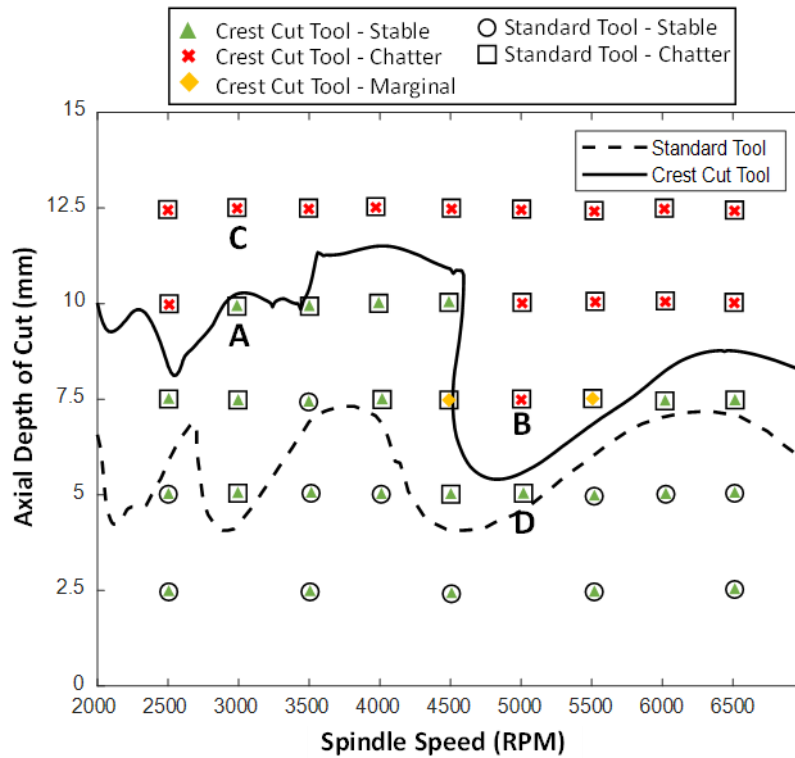


Figure 3.12. Stability lobes and chatter test results for crest-cut end mill

In Figure 3.13, the sound spectrums and the machined surface pictures for stable and unstable cases (cases A, B, C, and D in see Figure 3.12) are presented. For the unstable cases (B and C), the chatter marks appear at 5000 RPM and 3000RPM at 7.5 mm and 12.5mm axial cutting depth, respectively, as shown in Figure 3.13. The sound spectrum is captured by the microphone during the cutting experiment. For case B, the corresponding tooth passing frequency is $\omega_T = 333 \text{ Hz}$, while the chatter frequency ω_c with higher amplitude is shown around the natural frequency of the system.

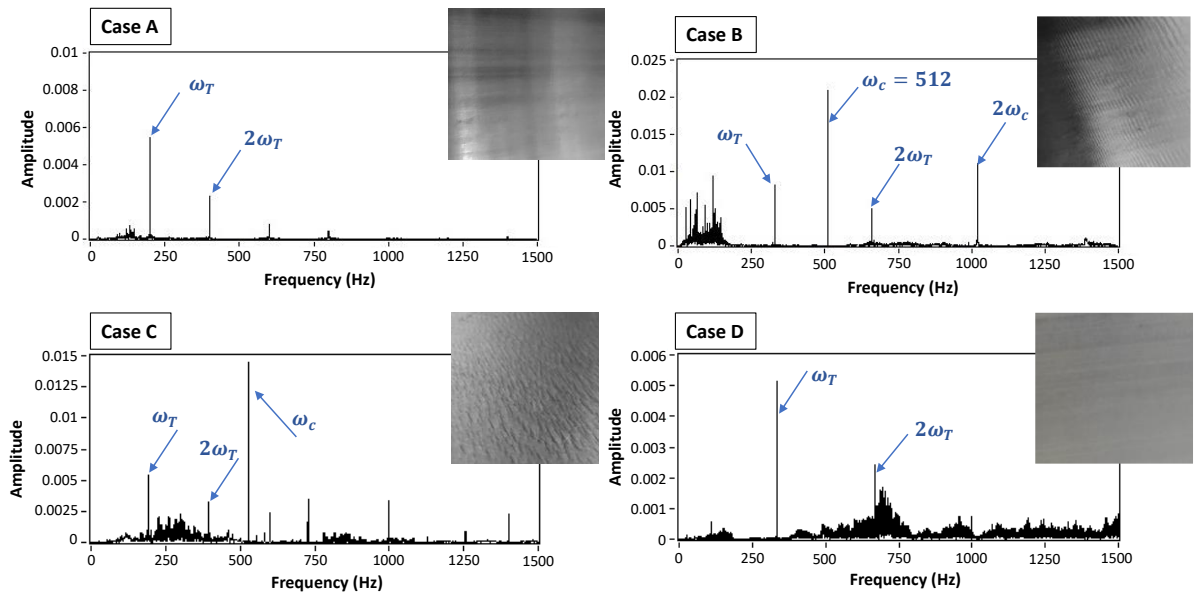


Figure 3.13. Sound Spectrum and cut surface of the different cases

Similarly, the photographs of the cut surface and the sound spectrums are also illustrated for the stable conditions (case A and D) in Figure 3.13. It is seen that for these cases the chatter marks are eliminated, and a clean surface is produced. The sound spectrums show only the tooth passing frequency and its harmonics with no indication of chatter.

Based on the above experimental validation, it can be concluded that the proposed model can be used effectively to predict chatter stability limits accurately for crest-cut end mills. The model is also used to investigate the stability of crest-cut tools with different wavelengths and wave amplitudes, and the results are presented in the next section.

3.4. Stability Analysis Based on Crest-cut Tools Geometry

As shown in the previous section (see Figure 3.12), crest-cut end mills demonstrate much better performance in terms of absolute and maximum stability limits compared to standard end mills. Since the wavy geometry of the cutting edge is the main reason for the increased stability, the effects of the wavelength and wave amplitude should be investigated in detail. For this purpose, another crest-cut end mill with different geometrical parameters is used to show these effects on stability lobe diagrams. In this case study, the diameter and length of the tool, as well as the tool-holder assembly conditions, are taken as the ones in Section 3.3.3 to achieve similar modal parameters

given in Table 3.2. The comparison between simulation and test results is shown in Figure 3.14.

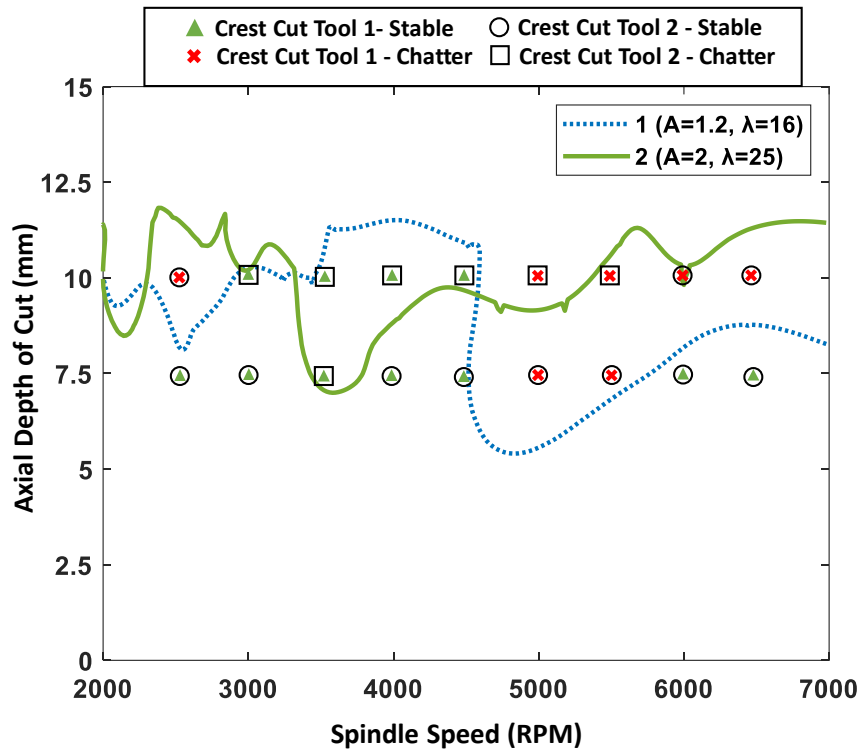


Figure 3.14. Comparison of two different crest-cut end mill

In this study, the stability lobe diagram for the second tool with geometrical parameters ($A=2$, $\lambda=25$) is validated by experiments and compared with the results obtained in Section 3.3.3. As shown in Figure 3.14, different crest-cut end mills behave differently on each point of the stability lobe diagram. Therefore, for a specific cutting condition, the selection of proper crest-cut tool wave shapes is crucial.

3.4.1. Effects of Edge Wave Shape on Chatter Stability

In this section, the effects of edge wave shape on stability lobe diagrams are investigated and the results are discussed. The simulations are performed using the tool dynamic properties and cutting conditions given in section 3.3.3. In the first step, the effects of the wavelength on the stability lobe diagrams are investigated with the illustrated results in Figure 3.15. In these simulations, the edge wave amplitude (A) was kept constant as 1mm. In order to complement these results with the effects of the edge wave amplitude on the stability limits, stability lobe diagrams with different wave amplitudes (with the constant

edge wavelength of 20mm) are shown in Figure 3.16.

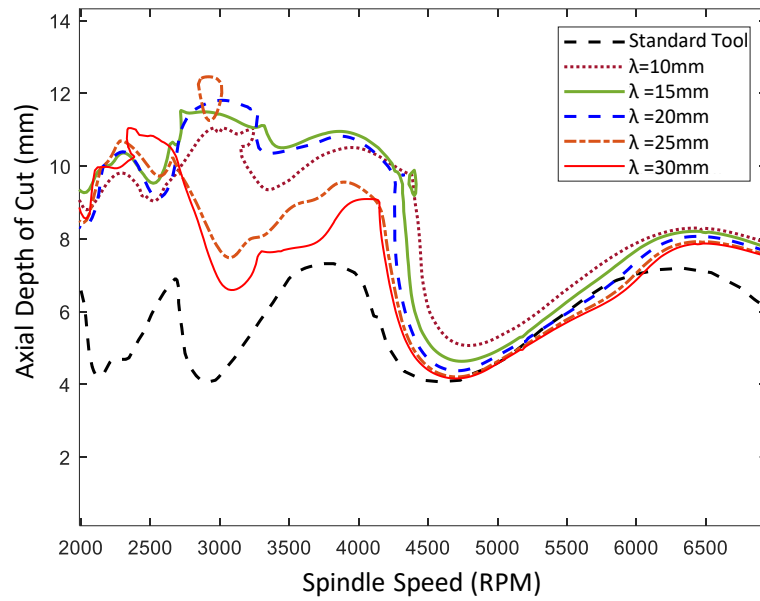


Figure 3.15. Stability lobe diagrams for different edge wavelengths

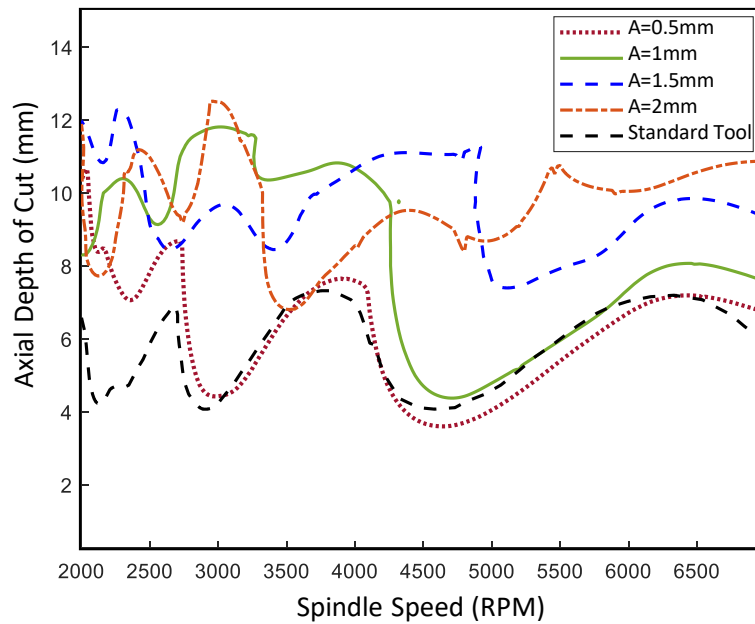


Figure 3.16. Stability lobe diagrams for different edge wave amplitudes

In Figure 3.15, the stability lobe diagrams of crest-cut end mills having different wavelengths are compared with the stability diagram of the standard end. It can be seen from the figure that although the stability limits for smaller wavelengths, i.e., $\lambda =$

10, 15, 20 mm, are close to each other they are significantly different for longer wavelengths of $\lambda = 25, 30$ mm. Based on these simulations, it can be deduced that higher stable cutting depths can be achieved with smaller wavelengths, however, they cannot be increased further after a certain minimum wavelength. Stability lobe diagrams remain similar for wl values between minimum and a specific value since the generated local pitch variations between two consequent teeth are repeated regardless of the number of engaged waves at the maximum stable depth of cut. Accordingly, if the wavelength becomes greater than the specific value, some of the pitch variations and as a result, some of the delays are eliminated and the stability limits decreases. Hence, for very large λ values the pitch variations become negligible as the number of the introduced delays to the system decreases and the crest-cut tool tends to behave like standard end mills.

The simulation results in Figure 3.16 indicate that the variation of wave amplitudes does not only change the stability limits but also shifts the lobes toward higher spindle speeds significantly. It is observed that, although the stability limit is increased, the lobe shift provides a higher stable depth of cuts even in the spindle speed values where the limits for the standard tool are at their minimum. As a result, by choosing the proper wave geometry of crest-cut end mills, it is possible to reach a higher depth of cuts at desired spindle speeds. Simulation results also show that by increasing the spindle speed, the wave amplitude of the crest-cut edges should also be increased to obtain higher stability limits. It is known that the chatter wavelengths increase with the spindle speed (E. Budak 2003b). Therefore, low values of wave amplitude on the edge may not be sufficient to eliminate the phase shift between two consecutive chatter marks at higher spindle speeds. For instance, as shown in **Error! Reference source not found.**, the tools with a wave amplitude of 0.5 mm and 1 mm lose their effectiveness after 2750 rpm and 4250 rpm, respectively. On the other hand, tools with 1.5mm and 2 mm of edge wave amplitudes are effective up to much higher spindle speeds due to their ability to eliminate the phase shift between chatter marks at these speeds. Therefore, like variable pitch end mills, in order to eliminate chatter in a specific spindle range, the amplitude should be large enough considering the ratio of chatter and tooth passing frequencies ($r_\omega = \frac{\omega_c}{\omega_T}$). For smaller ratios, larger wave amplitudes should be selected to increase stability.

The results obtained in this section prove that the selection of the geometrical parameters of crest-cut tools is vital in order to achieve high chatter-free MRR. Further, it is deduced

that the wave amplitude and wavelength must be selected according to the target cutting conditions.

3.4.2. Selection of Optimal Geometry for Crest-cut Tools

Similar to variable-pitch end mills, crest-cut tools present important opportunities to achieve high stability limits by tuning their geometry for a specific spindle speed. In order to determine the optimum crest-cut wave shape for a target spindle speed, simulations can be used, as explained in this section. To demonstrate the procedure, three different spindle speeds (3000, 4000, and 5000 RPM) are selected for which the maximum stability limits with different edge-wave shapes are calculated (Figures 3.19a, 3.20a, 3.21a). The optimal design is selected as the one which provides the highest stability limit. To investigate the performance of the optimal crest-cut tools, their stability diagrams are compared with a standard milling tool and a variable-pitch end mill having optimum pitch variation tuned according to the method proposed by (E. Budak 2003a) as presented in Figures 14b, 15b, and 16b. In all simulations, the same dynamics properties given in Table 3.2 are used. Results show that optimal crest-cut end mills provide higher stability limits at the target spindle speed in comparison to optimum variable-pitch end mills. Another important feature of the optimized crest-cut tools is their high stability zones compared to the tuned variable-pitch end mills, as shown in Figures 3.19b, 3.20b, 3.21b. According to the (a) parts of these figures, it is seen that for 3000 RPM, and 5000 RPM spindle speeds, the optimum wave amplitudes are 1mm and 1.5mm, respectively. This confirms the reasoning discussed in the previous section that the optimum wave amplitude is increased with increased spindle speed.

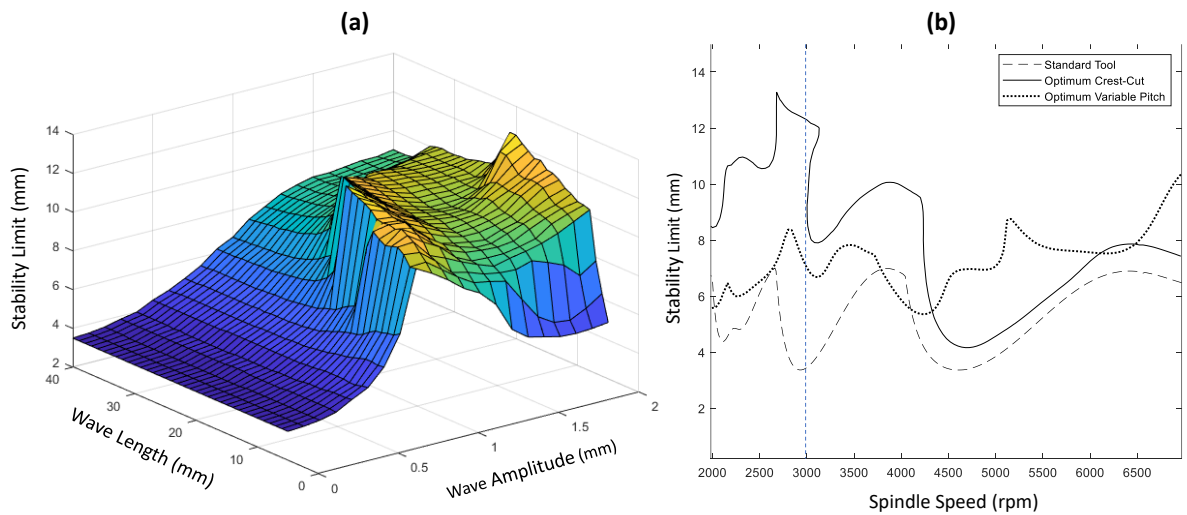


Figure 3.17. Stability limit of crest-cut end mill with different shapes b) comparison of optimum crest-cut end mill ($wa=1\text{mm}$, $wl=22\text{mm}$) and variable pitch tool in 3000 rpm

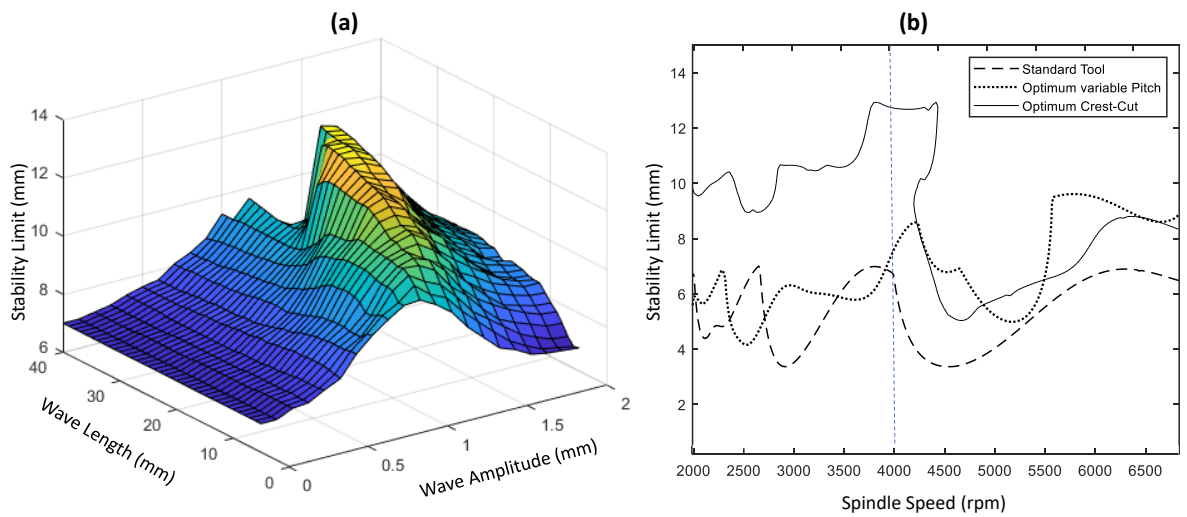


Figure 3.18. a) Stability limit of crest-cut end mill with different shapes b) comparison of optimum crest-cut end mill ($wa=1.3\text{mm}$, $wl=31\text{mm}$) and variable pitch tool in 4000 rpm

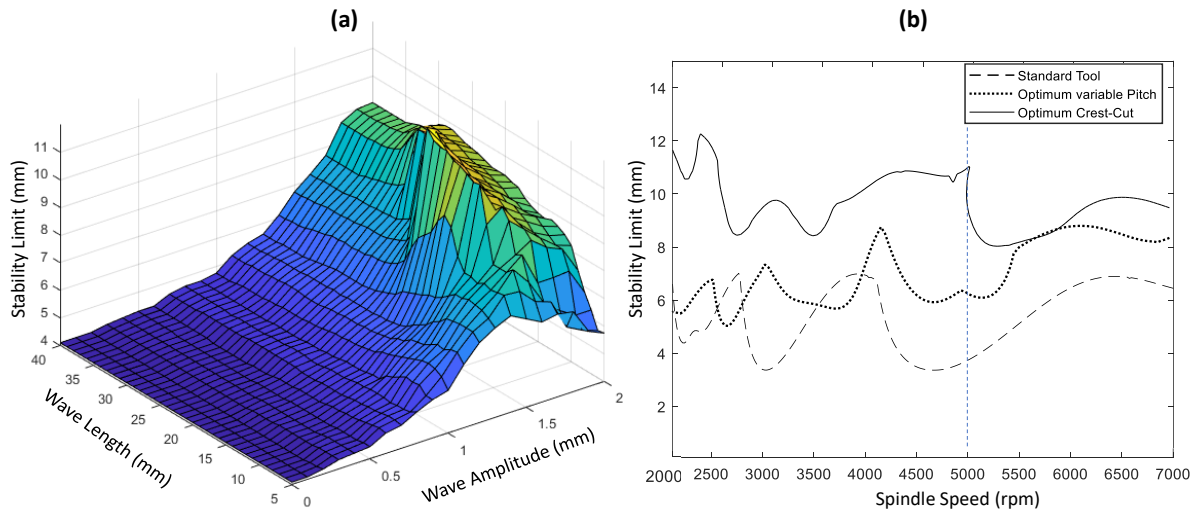


Figure 3.19. a) Stability limit of crest-cut end mill with different shapes b) comparison of optimum crest-cut end mill ($wa=1.5\text{mm}$, $wl=20\text{mm}$) and variable pitch tool in 5000 rpm

According to the obtained results, optimum crest-cut end mills can increase the stability limits and performance of the process at the desired spindle speed. Despite their relatively higher production time compared to standard end mills, crest-cut milling tools can reduce machining times substantially by increasing stable MRR. Moreover, it is deduced that crest-cut tools provide a much wider stable zone in the vicinity of desired spindle speed whereas narrow stable ranges are possible with variable pitch tools. This advantage makes crest-cut tools more robust against variations in chatter frequency and spindle speed. Different modes of tool, part and spindle assemblies may exist or emerge during the process based on the cutting location; however they cannot be suppressed by variable pitch tools as they are designed for a target chatter frequency. Furthermore, dynamics of the workpiece may also change due mass removal, especially in thin-walled structures (E Budak and Kops 2000; Erhan Budak et al. 2012). The chatter frequency changes resulting from such issues can be tolerated more effectively by crest-cut tools because of their wide stable ranges. Additionally, manufacturers prefer to use cutting tools in different operations under different cutting conditions. Optimized variable pitch tools designed for a specific spindle speed may perform even worse than standard end mills at different spindle speeds (Iglesias et al. 2019) whereas crest-cut tools can be used in a wider range of speeds. This advantage of crest-cut tools provides an opportunity for their use under different process conditions.

3.5. Conclusions

The present study investigates the mechanics and dynamics of milling with crest-cut end mills. The effectiveness of the crest-cut tools in improving the stability of milling processes is analyzed. Results show that these tools can provide significant improvements in terms of process stability. The specific contributions and conclusions of the study are listed as follows.

- Milling forces are predicted and confirmed with experimental results. Considering cutter-workpiece engagement and local cutting force coefficients, accurate cutting force predictions are obtained. Unlike standard milling tools, crest-cut end mills produce non-periodic cutting forces.
- The milling process stability with crest-cut tools is analyzed using the semi-discretization method, and the obtained results are verified experimentally for the first time in the literature. It is demonstrated that higher process stability can be obtained by crest-cut tools compared to standard and variable pitch milling tools.
- The stability diagrams obtained for crest-cut tools show several different characteristics. The most important one is the substantially enlarged stable regions compared to classical relatively narrow stability lobes offered by standard milling tools.
- As another novel part of the study, the effects of the crest-cut wave shape on the stability limits are investigated. Results show that the wave amplitude has a strong effect on cutting dynamics behavior and each wave amplitude is effective at a specific spindle speed range. Having the ability to disrupt the regeneration mechanism, higher values of wave amplitude result in higher stability limits at the conditions where the r_ω is low. However, the manufacturing of high wave amplitudes on edges is hindered by dimensional limitations.
- As the edge wavelength in crest-cut tools increases, the number of delays introduced to the system decreases. Therefore, the effectiveness of crest-cut tools reduces and the stability limit approaches to those of a standard endmill. On the

other hand, higher wavelengths provide a wider range of the producible wave amplitudes in manufacturing of these tools. In order to overcome this dilemma, the proposed model can be used to select the proper wavelength.

- The results show that the amplitude of the waves on the edges is a more important parameter. The wavelength selection can be made after choosing optimal wave amplitude considering the dimensional limitations in manufacturing the crest-cut tools.
- It is observed that, at a specific spindle speed, the optimal crest-cut tool demonstrates a higher stability limit compared to the standard end mill. Furthermore, the peak and absolute stability limits for the optimal crest-cut tools are higher than those of the tuned variable-pitch tools at the vicinity of the speed selected for tuning.

In summary, this study reveals the way that the shape of the wavy edges in crest-cut tools affects the stability of the process. Using effective crest-cut end mills designed and selected by the proposed guideline can significantly improve the process stability in the desired cutting conditions. One of the major limitations which can be solved in future studies is generation of a method to design an optimum edge shape quantitatively. The new outcomes of this study are expected to open new possibilities for the research community and industry to develop high-performance crest-cut end mills that can improve productivity further.

4. SERRATED END MILLS

Serrated end mills offer reduced milling forces, increased chatter stability and superior chip breaking ability once they are designed and employed properly. Although serrated end mills are often used in industry, the literature on these tools is quite limited compared to standard milling tools. In this chapter, a method to analyze mechanics and dynamics of milling with different types of serrated end mills will be presented. Tools with variable helix or/and pitch with different serration geometries and different types of end mills are also considered in the investigation. In the first step, the geometric model of the cutters will be defined mathematically and different parameters of the tools are extracted from the model. Then model of the mechanics of milling with these tools to predict cutting forces are presented and verified experimentally. In the proposed method a novel and accurate way to calculate the chip thickness is presented. For the first time in the literature, effects of serration wave geometry and cutting conditions on effectiveness of serrated tools are investigated resulting in optimized serration shapes for given milling conditions. As an important factor, effects of the phase shift direction on the serration waves are also investigated. In the last step, chatter stability analysis will be investigated. Because of the multiple delays which existing in the system, semi discretization method will be used to obtain stability lobe diagrams. The chatter stability model will be verified experimentally and then it will be used for comparing performance of the designed optimum serrated end mills with standard end mills.

4.1. Geometry of Serrated End Mills

In this section, a general geometric model for commonly used serrated end mills is presented. The proposed model for the mechanics and dynamics of these tools is based on the geometrical model introduced here.

The models considered in this study include cylindrical and tapered end mills, ball end

mills and round end mills with circular, sinusoidal and trapezoidal serration wave forms. These forms are chosen since most of the serration types used in industry can be represented by these wave forms. Moreover, tools with variable helix or/and pitch are also covered. In the geometry model, the tool is discretized along its axis as shown in Figure 1 and the cutting geometry is calculated for each axial element.

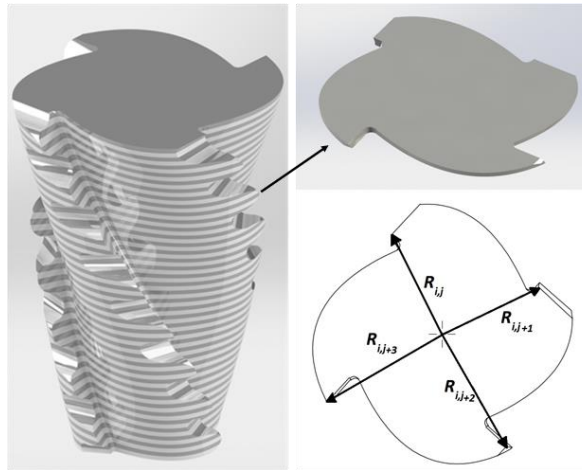


Figure 4.1. Axial elements of the end mill

4.1.1. Discretized End Mill Envelope Geometry

In this study, as shown in the Figure 4.2, the tool envelope is defined by four parameters. These parameters can define different shapes of serrated end mills (cylindrical and tapered end mills with flat, ball and round noses) which are used in industry.

To define general tool geometry, the tool radius as well as the angular position of each cutting edge in each element should be determined. The angular position of the first edge at the tip of the tool is taken as the reference, i.e. is assumed to be zero, and the angular position of the edge j at the tip of the tool are defined with respect to the first edge as follows:

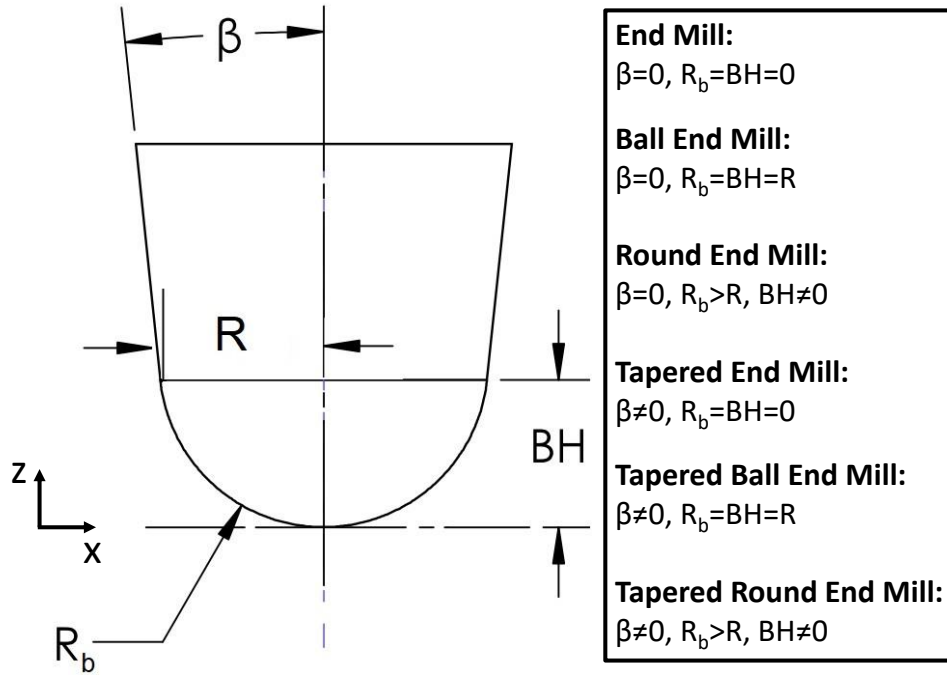


Figure 4.2. Tool envelop parameters for different types of end mills

$$p_t(j) = \sum_{s=1}^{s=j-1} p_s \quad (4.1)$$

where p_s is the pitch angle of the tooth s .

4.1.2. Case1: Cylindrical End Mills

For these tools, the radius is constant along the tool axis. Then, the angular position of element i on the tooth j (φ_{ij}) can be calculated as follows:

$$\varphi_{ij} = p_t(j) - \frac{\tan(\gamma_j)}{R} (z_i - z_t) + \varphi_{tj} \quad (4.2)$$

where φ_{tj} is the starting angular position of each edge in cylindrical part of the tool and is equal to $p_t(j)$ (if the tool tip is flat). z_t is the height of the first element in cylindrical section of the tool. It is equal to zero if the tool tip is flat and equal to BH when it has round tip. γ_j is the helix angle of the j^{th} tooth, R is the radius of the tool and z_i is the height

of element i .

4.1.3. Case 2: Tapered End Mills

For these tools, the radius varies along the tool axis due to the taper angle and can be represented as follows:

$$R_i = (z_i - z_t) \tan(\beta) + R \quad (4.3)$$

where R is the minimum radius of the tool's tapered part and β is the taper angle. z_t is axial position of the first element on the tapered part of the end mill and equal to BH and it is zero when tool does not have ball or round nose.

To define the angular position of each cutting edge in an axial element, the tapered end mills are categorized in two group as constant lead with varying helix and constant helix with varying lead.

For constant helix tools, the angular position of edge j on element i is defined as follows:

$$\varphi_{ij} = a_j \ln(1 + b(z_i - z_t)) + \varphi_{tj} \quad (4.4)$$

where,

$$a_j = \frac{\tan(\gamma_j)}{\sin(\beta)} \quad (4.5)$$

$$b = \frac{\tan(\beta)}{R_{min}} \quad (4.6)$$

For tapered end mills with constant lead, on the other hand, the angular position of each edge on the element i can be defined as follows:

$$\varphi_{ij} = c_j(z_i - z_t) + \varphi_{tj} \quad (4.7)$$

where,

$$c_j = \frac{\tan(\eta_j)}{R_{min}} \quad (4.8)$$

$$\eta_j = \tan^{-1}\left(\frac{2\pi R_{min}}{L_j \cos(\beta)}\right) \quad (4.9)$$

L_j is the lead of the j^{th} tooth.

4.1.4. Case 3: Ball and Round End Mills

If the tool nose is not flat, the angular position and the radius of the tool at each height of the ball end part can be calculated by the following equations:

$$R_i = \sqrt{R_b^2 - (R_b - z_i)^2} \quad (4.10)$$

$$\varphi_{ij} = \frac{z_i}{R_i} \tan(\gamma_j) + P_t(j) \quad (4.11)$$

where R_b is tool ball nose radius.

4.1.5. Local Radius

The teeth of the serrated end mills have wavy flank surfaces and waves on consecutive teeth have phase difference. In addition, due to the serrations, tool radius of each edge varies along the tool axis harmonically (Figure 4.1). Therefore, the contacts between tool edges and workpiece are not continuous along the depth of cut, and each tooth is engaged with the material in certain axial heights as shown in Figure 4.3. Consequently, the contact length between the workpiece and the cutter is less than the nominal axial depth of cut. This can be considered as the main reason for reduced cutting forces in milling with serrated tools.

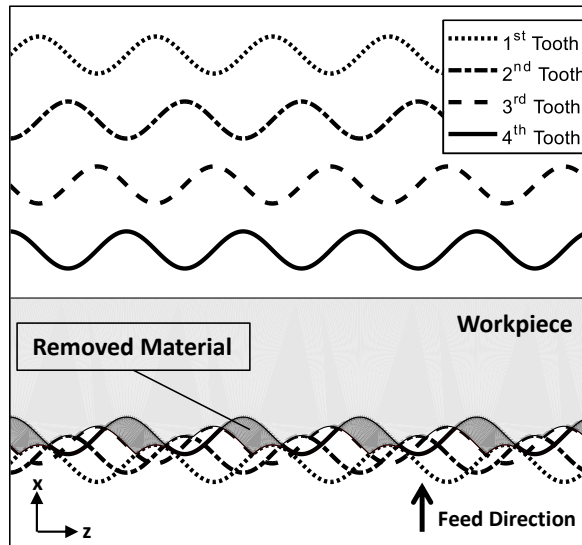


Figure 4.3. Engagement of cutting teeth and workpiece, and the marks left on the cut surface

Local radii depend on the serration wave forms such as circular, sinusoidal and trapezoidal. These shapes with different parameters can cover most of the serration forms which are currently used in the industry.

4.1.6. Sinusoidal Serration

This serration type includes sine waves with amplitude A and wave length of WL :

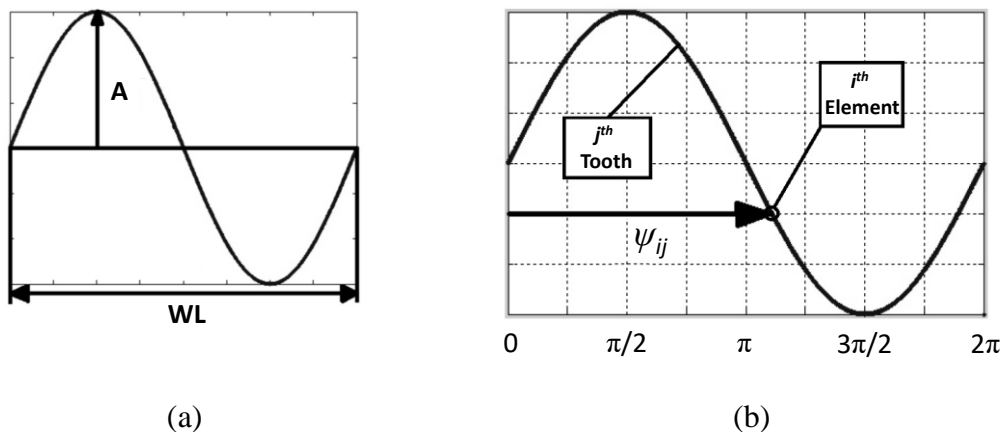


Figure 4.4. a) Parameters of sinusoidal serration b) Serration angle definition

Considering the effect of the wave shape on the local radius, for sinusoidal serrated tools the local radius of tooth j on the element i can be obtained as follows:

$$R_{ij} = R_i - A(1 - \sin(\psi_{ij})) \quad (4.12)$$

$$\psi_{ij} = 2\pi \left(\frac{l_{ij}}{WL} \right) - ps_j \quad (4.13)$$

where ψ_{ij} shows the angular position of the element i on the j^{th} tooth on serration. ps_j represents the phase shift which is the starting angle of the j^{th} tooth wave at tip of the tool. Moreover, l_{ij} shows the j^{th} cutting edge length from the serration starting point until element i which depends on the shape of the tool. For cylindrical end mills it can be determined as follows:

$$l_{ij} = \frac{z_i}{\cos(\gamma_j)} \quad (4.14)$$

For tapered end mills, the cutting edge length is calculated by using arc length formulation (Ortín 2010) for the tapered end mills with constant helix as follows:

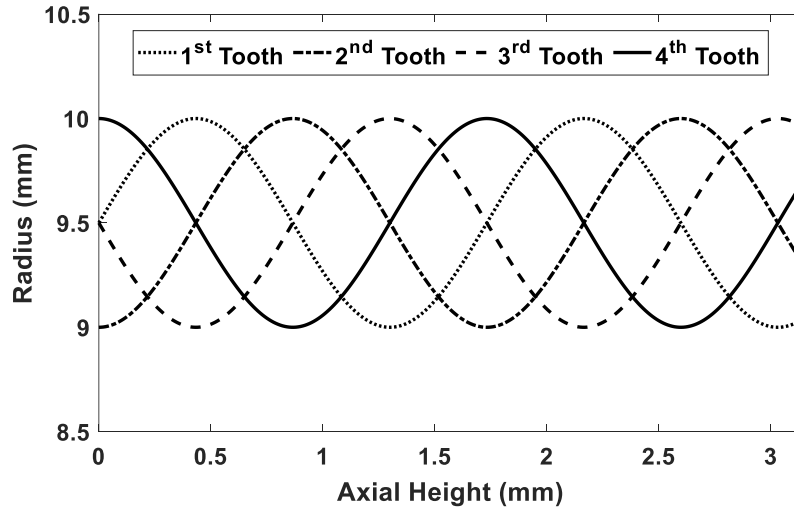


Figure 4.5. Local radius variation along axis for end mill with sinusoidal serration

$$l_{ij} = \sqrt{\tan(\beta)^2 + \left(\frac{\tan(\gamma_i)}{\cos(\beta)} \right)^2 (z_i - z_t)} \quad (4.15)$$

By using the same approach as used for the tapered end mills with the constant lead, the cutting edge length can be obtained as follows:

$$l_{ij} = \frac{1}{2 \tan \beta} \left[v \sqrt{\frac{1}{\cos^2 \beta} + \frac{\tan \eta_j^2 v^2}{R_{min}^2}} + \frac{R_{min}}{\cos^2 \beta \tan \eta_j} \ln \left(\frac{v \tan \eta_j + \sqrt{\frac{R_{min}^2}{\cos^2 \beta} + \tan \eta_j^2 v^2}}{R_{min}} \right) \right] - l_{0ij} \quad (4.16)$$

where,

$$v = R_{min} + \tan \beta (z_i - z_t) \quad (4.17)$$

$$l_{0ij} = \frac{R_{min}}{2 \tan \beta} \left[\sqrt{\frac{1}{\cos^2 \beta} + \tan \eta_j^2} + \frac{1}{\cos^2 \beta \tan \eta_j} \ln \left(\tan \eta_j + \sqrt{\frac{1}{\cos^2 \beta} + \tan \eta_j^2} \right) \right] \quad (4.18)$$

The schematic views of the different tool types with sinusoidal serrations are illustrated in Figure 4.6.

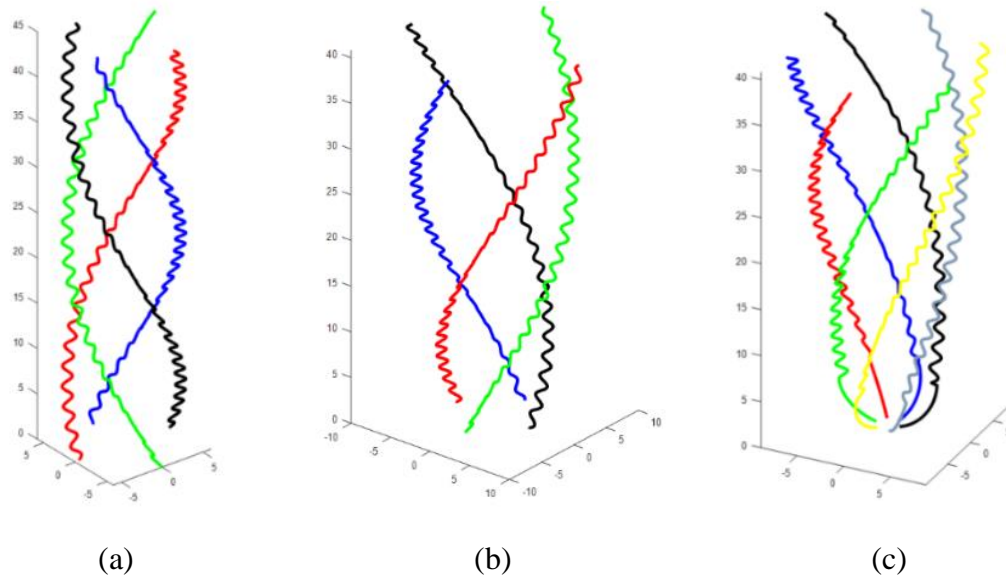


Figure 4.6. Schematic view of serrated (a) Flat end mill (b) Tapered end mill (c) Tapered ball end mill with sinusoidal serration

4.1.7. Circular Serration

Circular serration is defined by two circular sections as shown in Figure 4.7.

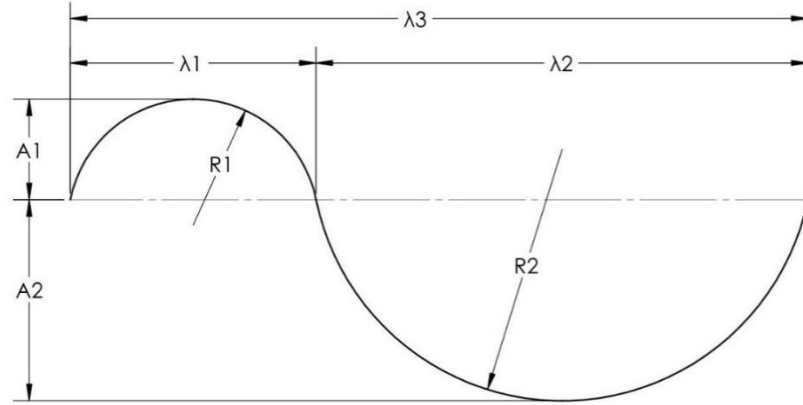


Figure 4.7. Parameters of circular serration waves

Local radius for the i^{th} element on the j^{th} tooth with circular serration type can be obtained by the following steps. One full serration wave length can be calculated by the following equation:

$$\begin{aligned}\lambda_1 &= 2\sqrt{A_1(2R_1 - A_1)} \\ \lambda_2 &= 2\sqrt{A_2(2R_2 - A_2)} \\ \lambda &= \lambda_1 + \lambda_2\end{aligned}\tag{4.19}$$

the parameters in this equation are illustrated in Figure 4.7.

The position, of the cutting edge in the i^{th} element on the j^{th} tooth along the serration wave can be obtained by following equation:

$$\begin{aligned}\psi_{ij} &= l_{ij} - \left(\frac{pS_j}{2\pi}\lambda\right) \\ x &= \text{Rem}\left(\frac{\psi_{ij}}{\lambda}\right)\end{aligned}\tag{4.20}$$

where l_{ij} is cutting edge length till i^{th} element which defined by equations (4.14), (4.15) or

(4.16) regarding end mill type. By considering the position of the element on the wave the local radius can be obtained by the formulations:

$$\text{if } \begin{cases} x < \lambda_1/2 \\ x \geq \lambda_1/2 \\ x < \lambda_1 + \lambda_2/2 \\ x \geq \lambda_1 + \lambda_2/2 \end{cases} \rightarrow \begin{cases} X = x \\ X = \lambda_1 - x \\ X = x - \lambda_1 \\ X = \lambda - x \end{cases}$$

if $x \leq \lambda_1$ (4.21)

$$R_{ij} = R_i + (\sqrt{R_1^2 - (\lambda_1/2 - X)^2} - R) \cos(\lambda_j)$$

if $x > \lambda_1$

$$R_{ij} = R_i - (\sqrt{R_2^2 - (\lambda_2/2 - X)^2} + A_1 - A_2 + R_2) \cos(\lambda_j)$$

Schematic view of the end mill and the change of its radius along the tool axis is shown in Figure 4.8.

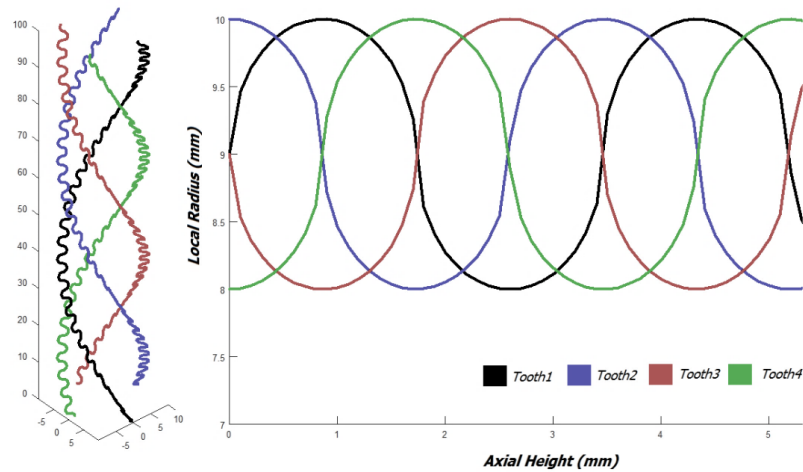


Figure 4.8. Schematic view of the end mill with circular serration

4.1.8. Trapezoidal Serration Form

Serrated end mills with trapezoidal wave form are also used in industry. The wave geometry is shown in Figure 4.9.

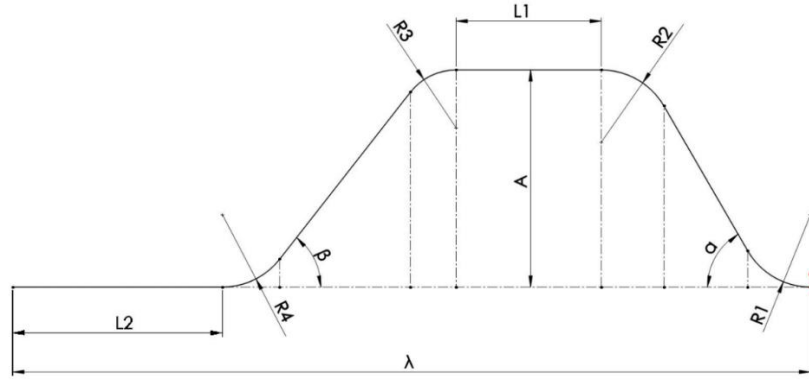


Figure 4.9. Parameters of trapezoidal serration waves

The local radius for the i^{th} element on the j^{th} tooth with trapezoidal serration type can be calculated by the following equations. Parameters for this equation are defined on the Figure 4.9.

$$\begin{aligned}
 \lambda_1 &= R_1 \cos \alpha, \quad \lambda_2 = (A - (R_1 + R_2) (1 - \sin \alpha)) \tan \alpha \\
 \lambda_3 &= R_2 \cos \alpha, \quad \lambda_4 = L_1, \quad \lambda_5 = R_3 \cos \beta \\
 \lambda_6 &= (A - (R_3 + R_4) (1 - \sin \beta)) \tan \beta \\
 \lambda_7 &= R_4 \cos(\beta) \\
 \lambda_8 &= L_2 \\
 \lambda &= \sum_{i=1}^8 \lambda_i
 \end{aligned} \tag{4.22}$$

The position of the i^{th} element on the j^{th} tooth on the serration wave can be determined by equation (4.23).

$$\begin{aligned}
 \psi_{ij} &= l_{ij} - \left(\frac{ps_j}{2\pi}\lambda\right) \\
 x &= \text{Rem}\left(\frac{\psi_{ij}}{\lambda}\right)
 \end{aligned} \tag{4.23}$$

By taking into account the position of the element on the serration wave the local radius of the i^{th} element on the j^{th} tooth can be calculated by following equations:

$$\begin{aligned}
\text{if } x \leq \lambda_1 &\rightarrow \begin{cases} X = x \\ R_{ij} = R_i - A + R_1 - \sqrt{R_1^2 - X^2} \end{cases} \\
\text{if } x \leq \sum_{i=1}^2 \lambda_i &\rightarrow \begin{cases} X = x - \lambda_1 \\ R_{ij} = R_i - A + X \cot \alpha + R_1(1 - \sin \alpha) \end{cases} \\
\text{if } x \leq \sum_{i=1}^3 \lambda_i &\rightarrow \begin{cases} X = x - \sum_{i=1}^2 \lambda_i \\ R_{ij} = R_i - R_2 + \sqrt{R_2^2 - (X - R_2 \cos \alpha)^2} \end{cases} \\
\text{if } x \leq \sum_{i=1}^4 \lambda_i &\rightarrow R_{ij} = R_i \\
\text{if } x \leq \sum_{i=1}^5 \lambda_i &\rightarrow \begin{cases} X = x - \sum_{i=1}^4 \lambda_i \\ R_{ij} = R_i - R_3 + \sqrt{R_3^2 - X^2} \end{cases} \\
\text{if } x \leq \sum_{i=1}^6 \lambda_i &\rightarrow \begin{cases} X = x - \sum_{i=1}^5 \lambda_i \\ R_{ij} = R_i - A + ((R_3 + R_4)(1 - \sin \beta) \dots \\ \dots \tan \beta - x) \cot \beta + R_4(1 - \sin \beta) \end{cases} \\
\text{if } x \leq \sum_{i=1}^7 \lambda_i &\rightarrow \begin{cases} X = x - \sum_{i=1}^6 \lambda_i \\ R_{ij} = R_i - A + R_4 \dots \\ \dots - \sqrt{R_4^2 - (X - R_4 \cos \beta)^2} \end{cases} \\
\text{if } x \leq \sum_{i=1}^8 \lambda_i &\rightarrow R_{ij} = R_i - A
\end{aligned} \tag{4.24}$$

4.1.9. Edge Point Position Vectors

The position vector \vec{P}_{ij} defines the location of point i , on the j^{th} edge at level z_i , in Cartesian coordinates (Figure 4.10). This vector can be calculated by converting polar coordinates to Cartesian ones:

$$\vec{P}_{ij} = (R_{ij} \cos \varphi_{ij})\vec{i} + (R_{ij} \sin \varphi_{ij})\vec{j} + z_i\vec{k} \quad (4.25)$$

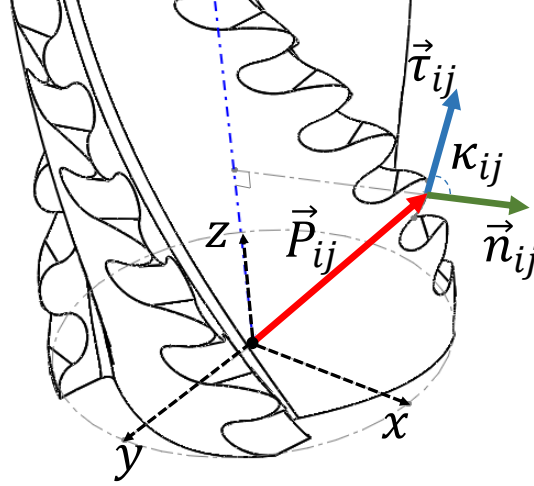


Figure 4.10. Axial immersion angle and position vector of element i on the j^{th} edge

4.1.10. Axial immersion angle

Since differential force directions are dependent on axial immersion angle, κ_{ij} , determining this angle is a significant part of force calculations. The immersion angle is the angle between the tool edge tangent vector and the unit vector \vec{n}_{ij} which is directed toward edge along tool radius in x - y plane as shown in Figure 4.10.

Due to the high number of elements in the axial direction, a vector connecting two ends of each element ($\vec{\tau}_{ij}$) on the cutting edge is a good approximation for the tangent vector in that element. Axial immersion angle can be obtained by dot product of these vectors as follows:

$$\begin{aligned} \vec{\tau}_{ij} &= \vec{P}_{i+1j} - \vec{P}_{ij} \\ \vec{n}_{ij} &= (\cos \varphi_{ij})\vec{i} + (\sin \varphi_{ij})\vec{j} \\ \kappa_{ij} &= \cos^{-1} \left(\frac{\vec{\tau}_{ij} \cdot \vec{n}_{ij}}{|\vec{\tau}_{ij}| |\vec{n}_{ij}|} \right) \end{aligned} \quad (4.26)$$

Variation of the axial immersion angle for the one tooth of serrated end mill with sinusoidal serration ($WL = 2\text{mm}$, $A = 0.25\text{mm}$) is demonstrated in Figure 4.11.

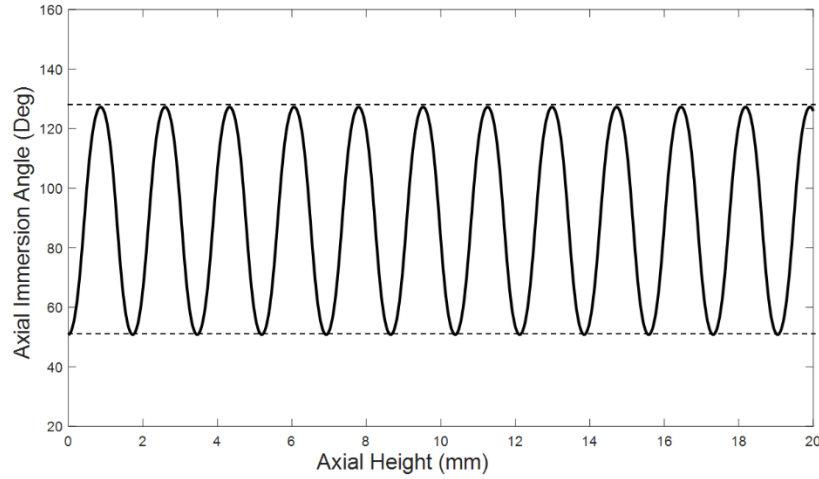


Figure 4.11. Variation of axial immersion angle (κ) along tool axis

4.1.11. Local rake and oblique angles

Serration geometry of the tool results in variable rake, α_{ij} , and oblique, γ_{ij} , angles along the cutting edges (Figure 4.12). Even if helix angle is zero, the existence of rake angle results in local non-zero oblique angles in some elements. Also because of presence of the helix angle, rake angle changes along cutting edge and the local values vary between negative and positive values in each portion of serration wave. The variation of these angles affects the chip removal mechanisms and should be considered in analyzing mechanics of milling. It is a known fact that increased rake angle affects the shearing mechanism positively. This tendency can be taken advantage of when selecting or designing serrated end mills. However, in order to take advantage of this, cutting edge strength must also be considered, as cutting edge strength diminishes as the rake angle increases. Moreover, variation of these angles affects cutting force coefficients which have significant role in calculation of cutting forces. Therefore, for each tooth in each axial element, the local cutting angles should be calculated.

The local rake, α_{ij} , and oblique, γ_{ij} , angles for each tooth on each element can be obtained

using the 3D geometrical relationships as follows:

$$\alpha_{ij} = 2(\sin^{-1}(\cos(c_{ij} - \beta) \sin(\alpha_j/2)) + \sin^{-1}(\sin(c_{ij} - \beta) \sin(\gamma_j/2))) \quad (4.27)$$

$$\gamma_{ij} = 2(\sin^{-1}(\sin(c_{ij} - \beta) \sin(\alpha_j/2)) - \sin^{-1}(\cos(c_{ij} - \beta) \sin(\gamma_j/2))) \quad (4.28)$$

where α_j and γ_j are the global rake and helix angles of the j^{th} tooth. β is taper angle and c_{ij} is used to make equation simpler and it can be calculated by equation (4.29):

$$c_{ij} = \tan^{-1}\left(\frac{R_{i+1j} - R_{i+1j}}{dz}\right) \quad (4.29)$$

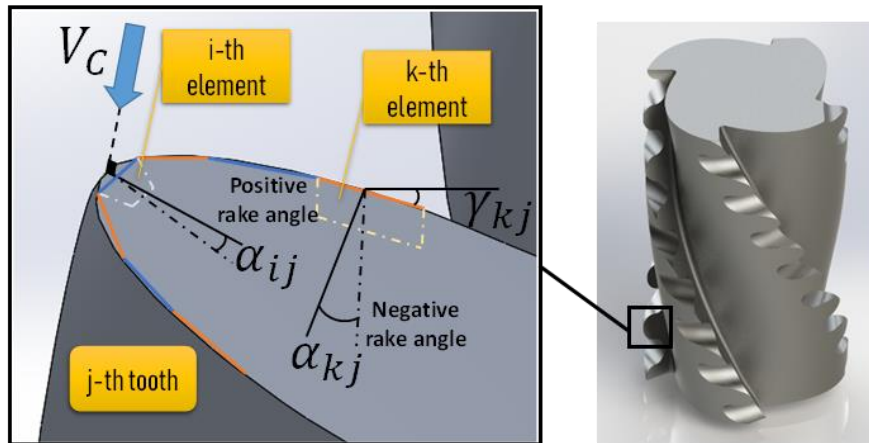


Figure 4.12. Local rake and oblique angles on the serration wave for each element

The variation of the rake angle along the cutting edge of a sample end mill which has circular serration is illustrated as an example in the Figure 4.13. Helix and rake angle of the tool are 30 and 5 degree respectively. As shown in Figure 4.13, local rake varies between 30 and -30 degree.

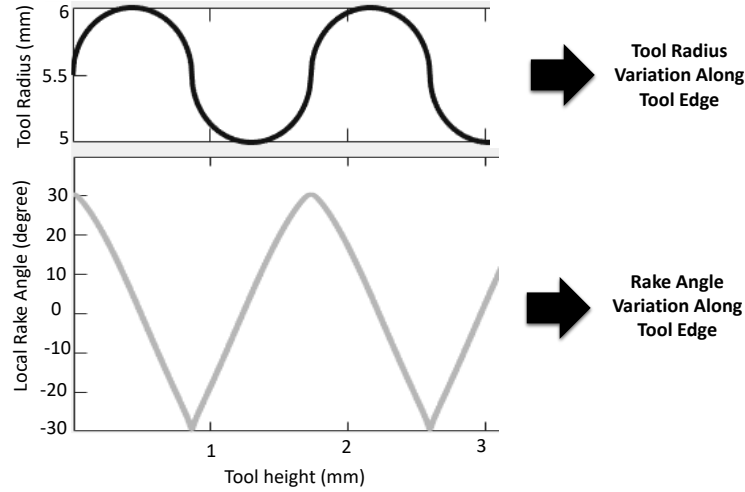


Figure 4.13. Local rake angle variation along end mill cutting edge

4.2. Force Model of Serrated End Mills

Linear edge force model (E. Budak, Altıntaş, and Armarego 1996) is used in this study to formulate milling forces. First step in the calculation procedure is obtaining differential forces in axial, radial and tangential directions (Figure 4.14), for each tooth on each axial element at any angular position of a cutting tool:

$$\begin{aligned}
 dF_a(i, j) &= g(\varphi_{ij}) [K_{ae}(i, j) + K_{ac}h_{ij}(\varphi_{ij})] db \\
 dF_r(i, j) &= g(\varphi_{ij}) [K_{re}(i, j) + K_{rc}h_{ij}(\varphi_{ij})] db \\
 dF_t(i, j) &= g(\varphi_{ij}) [K_{te}(i, j) + K_{tc}h_{ij}(\varphi_{ij})] db
 \end{aligned} \tag{4.30}$$

where $g(\varphi_{ij})$ is a step function which is zero when the tooth is not in cut, i.e. if φ_{ij} is not between φ_{start} and φ_{exit} , and is equal to one when the tooth is in cut, i.e. φ_{ij} is between φ_{start} and φ_{exit} . K_{ac} , K_{rc} and K_{tc} are the cutting force coefficients in axial, radial and tangential directions, respectively, whereas K_{ae} , K_{re} and K_{te} are the edge cutting force coefficients in 3 orthogonal directions. These coefficients can be determined using orthogonal cutting data base and oblique cutting transformation (E. Budak, Altıntaş, and Armarego 1996). Geometrical parameters of the tool such as oblique and rake angles

influence cutting coefficients. Because of local rake and oblique angles variation along cutting edges, these coefficients have to be calculated for each edge on every axial and angular positions separately. The elemental axial depth, db , is defined by following equation:

$$db = \frac{dz}{\sin(\kappa_{ij})} \quad (4.31)$$

$h_{ij}(\varphi_{ij})$ is the uncut chip thickness for the i^{th} element of the j^{th} tooth and it is calculated at each rotational step.

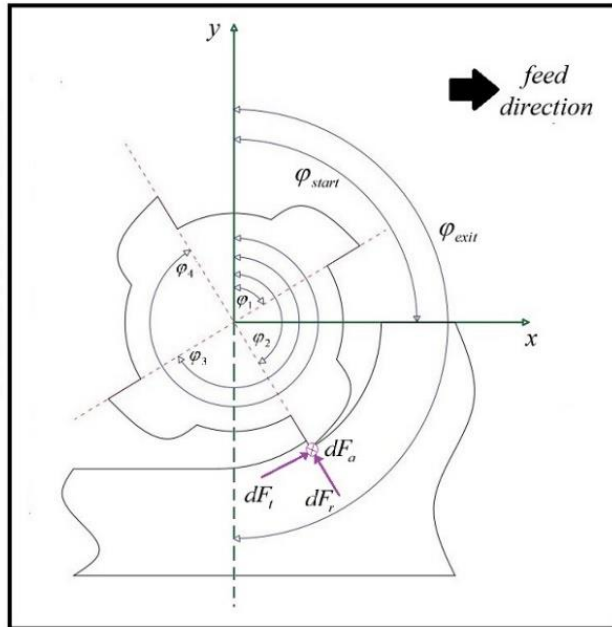


Figure 4.14. Differential cutting forces in axial, radial and tangential direction

4.2.1. Uncut Chip Thickness Calculation

Uncut chip thickness should be calculated in a direction which is perpendicular to the cutting edge. In previous studies this issue was not considered and some assumptions were used to simplify the problem (Tehranizadeh and Budak 2017; S. D. Merdol and

Altintas 2004; Dombovari, Altintas, and Stepan 2010; Hosseini, Moetakef-Imani, and Kishawy 2011; Koca and Budak 2013). Therefore, a new method has been developed to calculate the chip thickness accurately. In this method the interface of the tool and workpiece is found and these areas are considered as chip areas. These chip areas are divided considering elemental disks which are defined in previous sections. While constructing these differential chip areas, 2 main issue is considered: 1) Differential chip areas should not intersect each other. 2) In each element, the chip area is constructed in a direction where the chip thickness becomes perpendicular to the edge. To meet these requirements the following steps should be taken (Figure 4.15):

1. To find the chip thickness for each edge on each element the shape of the workpiece surface which remained after cutting by the previous teeth should be calculated for tooth j at each axial height i in each angular position (line marked with number 1 in Figure 4.15). The formulas used for this step are:

$$W(i, j, \varphi_{ij}) = \max \left\{ \begin{array}{l} 0 \\ \min \{ R_{im} - k f_t \sin(\varphi_{ij}) \} \end{array} \right\} \quad (4.32)$$

$$m = \begin{cases} k - j & \text{if } k - j > 0 \\ k - j + N_t & \text{if } k - j \leq 0 \end{cases}$$

$$k = 1, 2, \dots, N_t$$

2. Based on the serration shape of the in-cut tooth and the surface of the workpiece (step 1) the chip areas are constructed for each edge at each angular position (areas between tool and workpiece in Figure 4.15). The thickness of this area in each axial element (H) can be determined from the following:

$$H(i, j, \varphi_{ij}) = R_{ij} - W(i, j, \varphi_{ij}) \quad (4.33)$$

3. In order to prevent the intersection of differential chip areas for different elements, the total chip area is divided into different regions based on the changes in slope and curvature of the serration wave (dash line which marked with number 3 in Figure 4.15). In the circular serration all of the perpendicular lines to the edges pass through the origin and they are not intersecting each other. Therefore, there is no need to divide the chip area in a circular serration type.

4. In each region, intersection of the line perpendicular to the cutting edge with the limits of that region and previously machined surface (areas which marked as number 4 in Figure 4.15) is calculated. The intersection of two lines L_1 and L_2 (O) can be calculated by using following equation:

$$O_x = \frac{(x_1y_2 - y_1x_2)(x_3 - x_4) - (x_1 - x_2)(x_3y_4 - y_3x_4)}{(x_1 - x_2)(y_3 - y_4) - (y_1 - y_2)(x_3 - x_4)} \quad (4.34)$$

$$O_y = \frac{(x_1y_2 - y_1x_2)(y_3 - y_4) - (y_1 - y_2)(x_3y_4 - y_3x_4)}{(x_1 - x_2)(y_3 - y_4) - (y_1 - y_2)(x_3 - x_4)}$$

where O_x and O_y are the coordinates of point O . In equation (4.34) each of lines L_1 $((x_1, y_1), (x_2, y_2))$ and L_2 $((x_3, y_3), (x_4, y_4))$ is defined by two points. After calculating intersection of perpendicular lines to edge j at each height i with limits of that region (U_{ij}) and previously machined surface (S_{ij}), chip thickness for any element is defined by the following equation

$$h(i, j, \varphi_{ij}) = \min \left\{ \begin{array}{l} \frac{|P_{ij} - U_{ij}| + |P_{i+1j} - U_{ij}|}{2} \\ \frac{|P_{ij} - S_{ij}| + |P_{i+1j} - S_{ij}|}{2} \end{array} \right\} \quad (4.35)$$

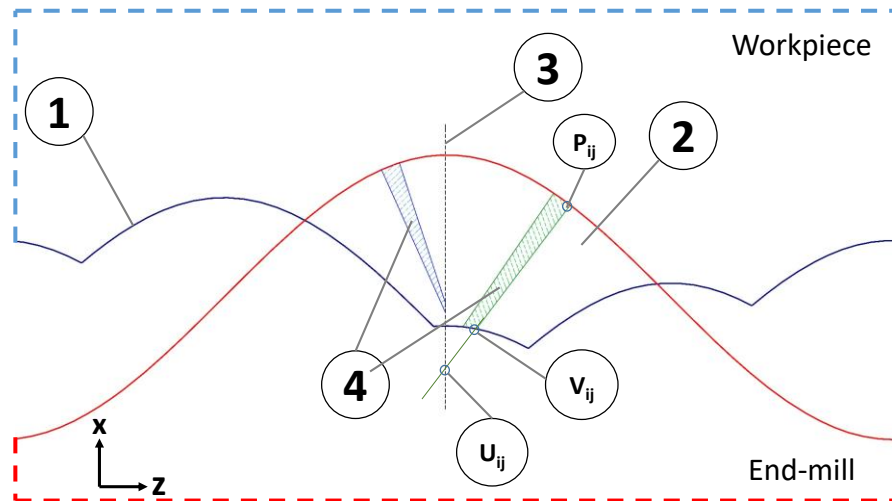


Figure 4.15. Steps of chip thickness calculations

Some examples for different types of serrations and chip thickness calculations are shown in Figure 4.16.

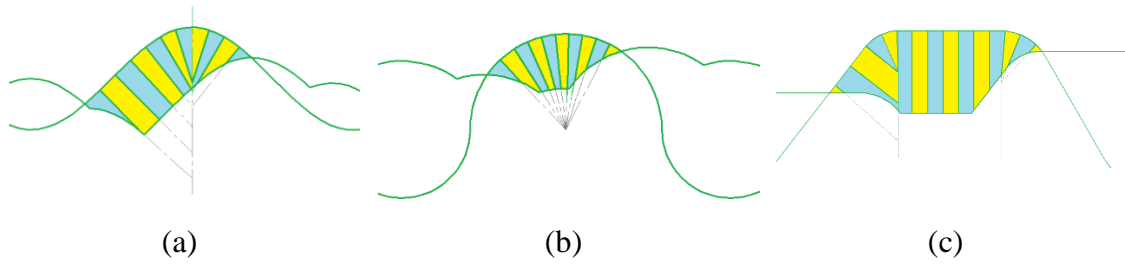


Figure 4.16. Chip thickness calculations for different types of serrations.

a) Sinusoidal b) Circular c) Trapezoidal

4.2.2. Total Forces in x, y and z Directions

The differential forces in x , y and z directions as a function of differential forces in tool coordinates, can be derived as follows:

$$\begin{aligned}
 dF_x &= -dF_r \sin(\varphi_{ij}) \sin(\kappa_{ij}) \\
 &\quad -dF_t \cos(\varphi_{ij}) - dF_a \cos(\kappa_{ij}) \sin(\varphi_{ij}) \\
 dF_y &= -dF_r \cos(\varphi_{ij}) \sin(\kappa_{ij}) \\
 &\quad +dF_t \sin(\varphi_{ij}) - dF_a \cos(\kappa_{ij}) \cos(\varphi_{ij}) \\
 dF_z &= dF_r \cos(\kappa_{ij}) - dF_a \sin(\kappa_{ij})
 \end{aligned} \tag{4.36}$$

To determine the total forces in x , y and z directions in each angular step the sum of differential forces from all elements and teeth should be calculated.

$$\begin{aligned}
 F_x(\varphi) &= \sum_{z=0}^a \sum_{j=1}^{N_t} dF_x(z, j) \\
 F_y(\varphi) &= \sum_{z=0}^a \sum_{j=1}^{N_t} dF_y(z, j) \\
 F_z(\varphi) &= \sum_{z=0}^a \sum_{j=1}^{N_t} dF_z(z, j)
 \end{aligned} \tag{4.37}$$

4.2.3. Experimental Verification

To verify the proposed model some experiments were carried out to obtain the cutting forces in the milling process with serrated end mills. These tests were conducted on the MAZAK 3-axis CNC machine with Kistler Piezo-Dynamometer. The work-piece material was selected as Aluminum 7075 (Figure 4.17).



Figure 4.17. Setup of experiments

The experimental conditions and tool properties manufactured by KARCAN™ are shown in Table 4.1. Figure 4.18 demonstrates the comparison of experimental and simulation results where a good agreement is observed between them.

Table 4.1. Tool and process parameters in experiments.

Test No.	Tool Parameters					Process Parameters			
	Tool Type	Tool Dia.	Cutting Angles	Serration Type	Serration Parameters (mm)	Spindle Speed	Depth of Cut	Width of Cut	Feed
1	End Mill	12mm	$\alpha=5^\circ$ $\lambda=30^\circ$	Trapezoidal	L1=0.3, L2=0.2 A=0.5, $\alpha=\beta=45^\circ$ R1=R2=R3=R4=0.2	1200 rev/min	15mm	3mm	0.1 mm/tooth
2	End Mill	12mm	$\alpha=5^\circ$ $\lambda=30^\circ$	Sinusoidal	A=0.5 WL=2	1200 rev/min	5mm	3mm	0.15 mm/tooth
3	End Mill	12mm	$\alpha=5^\circ$ $\lambda=30^\circ$	Circular	R1=R2=0.5 A1=A2=0.3	1200 rev/min	15mm	3mm	0.1 mm/tooth
4	Tapered Ball End Mill	Min 12mm $\beta=3^\circ$	$\alpha=6^\circ$ lead=100 mm	Sinusoidal	A=0.25 WL=2	1200 rev/min	40mm	1mm	0.05 mm/tooth

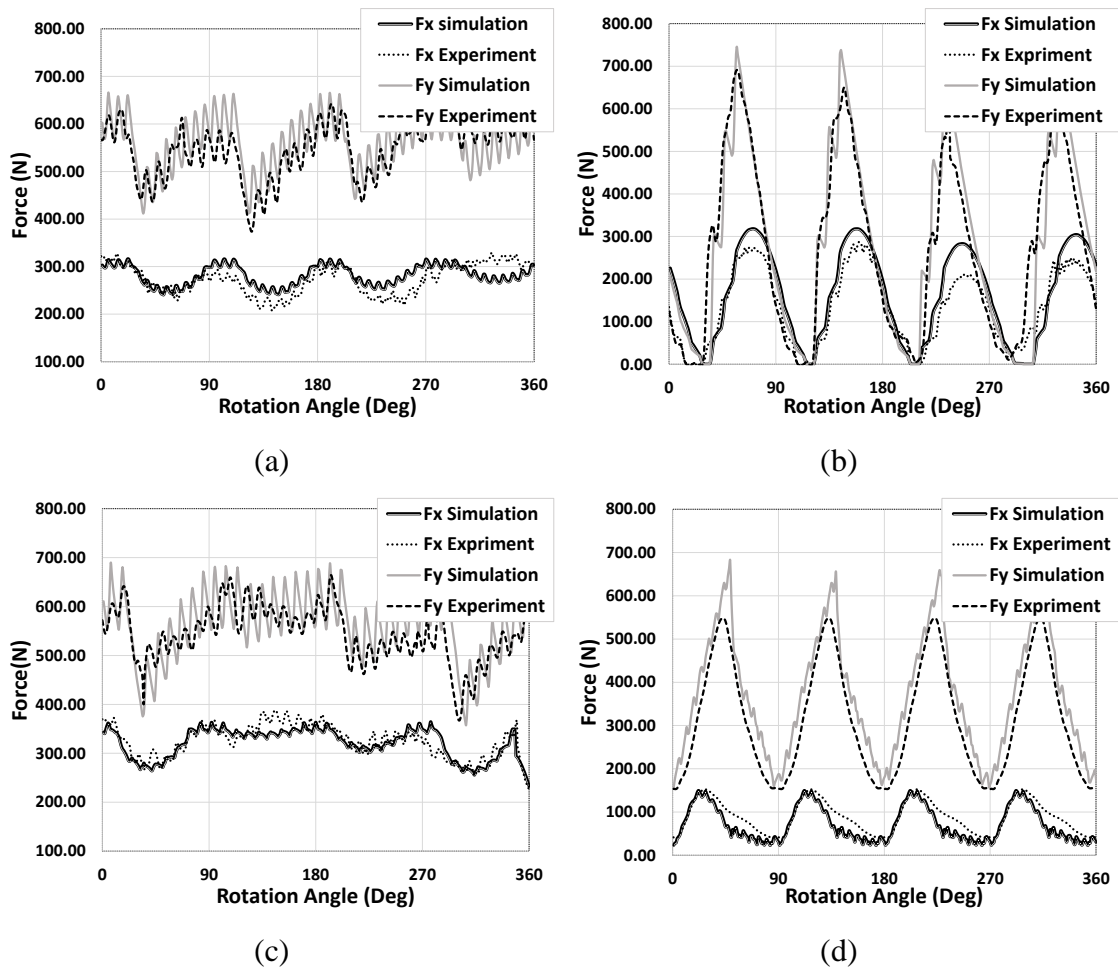


Figure 4.18. Comparison of measured and simulated cutting forces in experimental and simulation results for different conditions given in Table 1: a) 1, b) 2, c) 3 and d) 4

4.3. Serration Parameters Effects on The Cutting Forces and Optimization

The simulation results show that serration parameters have significant role on the milling forces. As a simple instance the effect of sinusoidal serration wave parameters on the maximum F_{xy} was investigated. In these sample simulations axial depth of cut, radial depth of cut and feed rates are chosen as 10mm, 5mm and 0.1mm/(rev.tooth) respectively. The end mill with sinusoidal serration has 10mm diameter and rotates in 1500rpm. The effect of the wave length in two different wave amplitude on the milling forces is shown in the Figure 4.19. This shows that F_{xy} (resultant force of F_x and F_y) changes between

1800N to 800N by using different serration parameters. This figure illustrates the importance of the proper design of serration parameters. In addition, it shows that parameters have no predictable effect on the maximum resultant force.

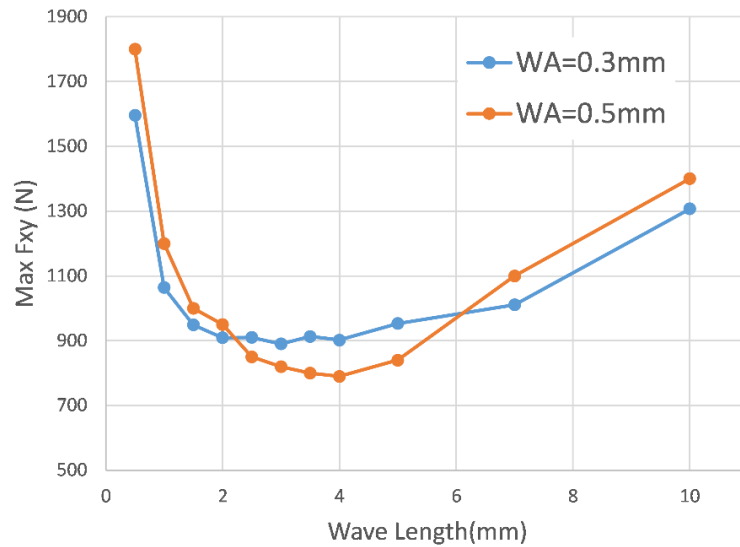


Figure 4.19. Maximum F_{xy} for different sinusoidal serration shapes

4.3.1. Effects of Local Rake and Oblique Angles

Along serrated cutting edges, rake and oblique angles vary. It is well known that increasing the rake angle has a good effect on the shearing process. As a result, it is better to use the portion of the cutting edges with the greatest positive rake angles. This situation can be controlled by choosing the phase shift direction between the serration waves of the consecutive teeth. If the serration wave phase difference between two consecutive teeth is positive, the tool has teeth with forward phase shift and it has reverse phase shift if this difference is negative. These two types of phase shift can be distinguished by looking at the directions of the flute and the serration spirals. If they have the same direction (Figure 4.20-a), e.g. both right hand, then the sections with lower rake angles remove the material resulting in higher cutting force coefficients. On the other hand, if their directions are opposite, the sections with higher positive rake angles (Figure 4.20-b) remove the material resulting in lower cutting force coefficients. This comparison shows the

importance of the serration wave generation on milling tools during their production.

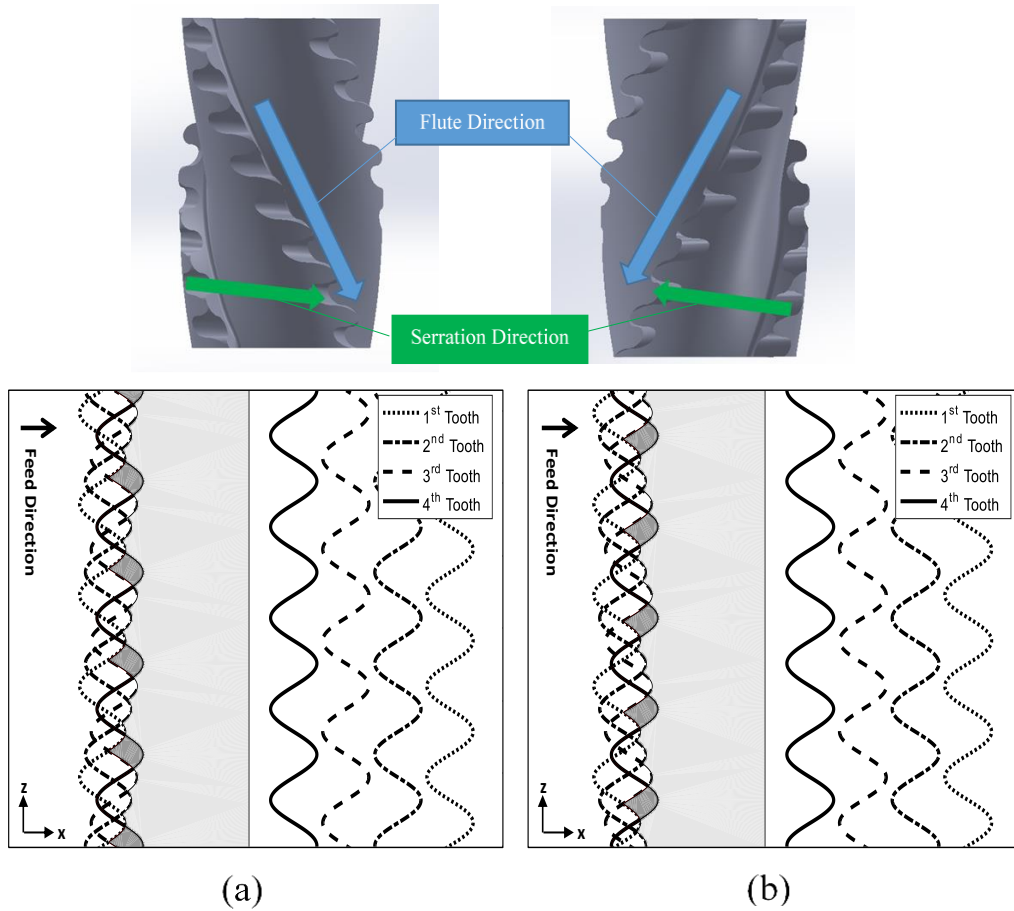


Figure 4.20. Serrated end mill with a) forward phase shift b) reverse phase shift and its engagement with workpiece

4.3.2. Experimental Verification of the Effect of Phase Shift Direction

The effect of phase shift direction on mechanics of milling with serrated tools was explained in the previous section. Milling tests were performed with custom made serrated end mills to verify this effect. Two different end mills were used in the tests. The parameters shown in Table 4.2 are common for both tools.

Table 4.2. Tool parameters for tests of phase shift effect

Tool No.	Tool Parameters					
	Tool Type	Tool Dia.	Cutting Angles	Serration Type	Serration Parameters (mm)	Phase shift Direction
1	End Mill	12mm	$\alpha=5^\circ$ $\lambda=30^\circ$	Circular	R1=R2=0.5 A1=A2=0.3	Forward
2						Reverse

Tool 1 has right hand tool helix and right-hand serration spiral resulting in portions with small or even negative rake angle that engaged with the material being cut. On the other hand, Tool 2 has right hand tool helix but left-hand serration spiral resulting in portions with higher rake angles engaged with the material being cut.

To demonstrate the effect of phase shift direction on milling processes with serrated cutting tools, milling tests were carried out where the resulting milling forces were measured. Milling tests were carried out on a Mazak 3-Axis machine tool using a Kistler table type dynamometer on which Al7075 block was mounted.

Axial depth of cut of 15mm and radial depth of cut of 3mm were used in all experiments while the feed per tooth was varied between 0.05–0.1 mm/rev.tooth and spindle speed was kept the same as 1800 RPM where the milling mode was down-milling.

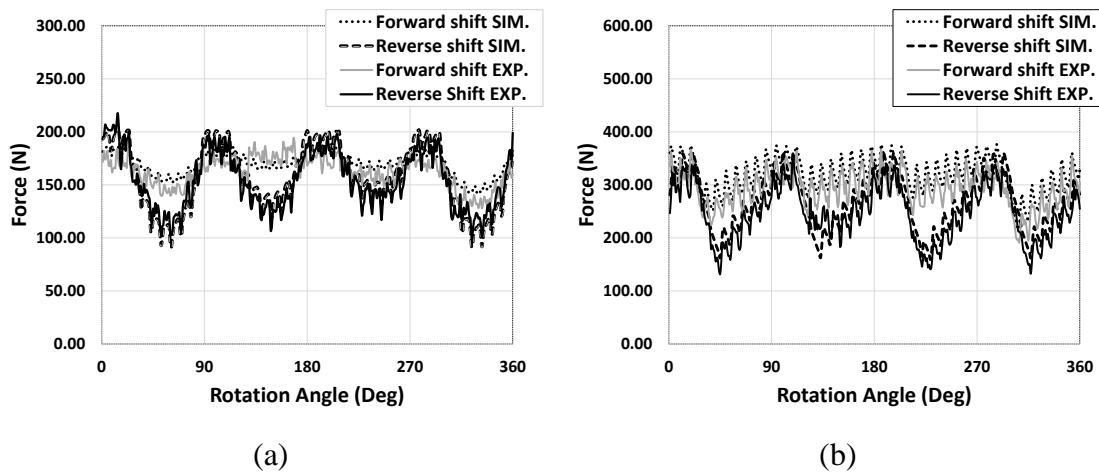


Figure 4.21. Comparison of milling forces for Tool 1 and Tool 2 (Table 4.2) with $f_t=0.05\text{mm/tooth}$ in a) x and b) y direction

Significant difference can be observed between Tool 1 and Tool 2 in terms of F_y and F_z forces even with low feeds while maintaining almost the same average F_x shown in Figure

4.21 and the same trend is seen in Figure 4.22. However, with the increasing feed per tooth, the difference between the forward and reverse phase shift is increased as well. Higher reduction of the cutting forces by using Tool 2 is the result of more engagement between the serrated edge and the work material. When the contact area between the tool and the material increases, the parts of the edge which have higher positive rake angles engage in the process more reducing cutting forces.

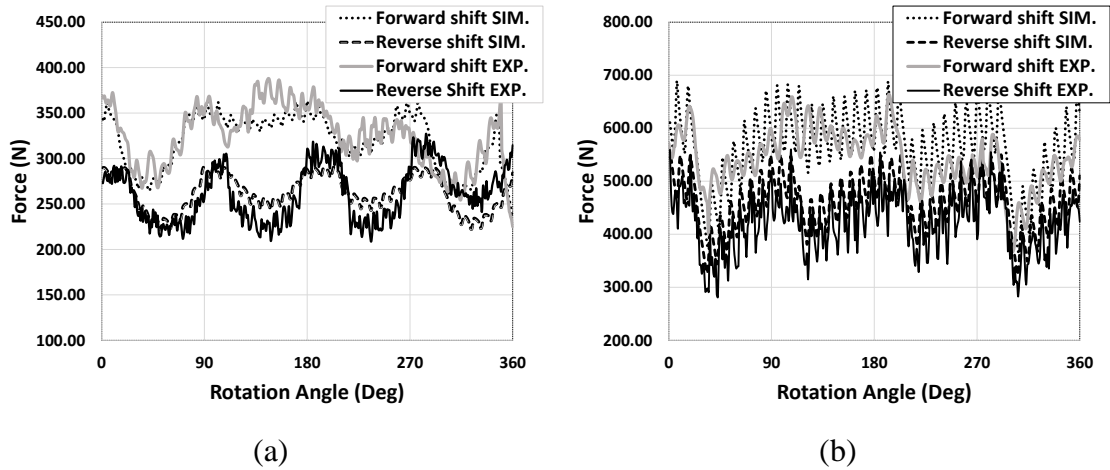


Figure 4.22. Comparison of milling forces for Tool 1 and Tool 2 (Table 4.2) with $f_t=0.1\text{mm/tooth}$ in a) x and b) y direction

4.3.3. Optimization of Serration Wave Parameters

As mentioned in the previous section, the shape of the tool edge serration has significant role on the cutting forces and it can be reduced by choosing proper geometrical parameters. There are two ways to find the optimum design for the tool serration wave in different conditions. The optimum serration can be found by simulating all possible conditions and find the best design by comparison of solutions. It is obvious this method is time consuming and it is not efficient. Another procedure is using optimization algorithms (like evolutionary algorithms) which search the solution space in a much smart way and as result they find optimum solutions faster than first method. In this study, genetic algorithm (GA) is used to optimize serration wave shape parameters to decrease milling forces. GA is a method which increases the quality of the solutions by evolution of the population by using natural genetic operators like crossover and mutation. By

considering these natural rules, chromosomes with higher quality produce more offspring than the less fit ones. As a result, new generations are more compatible with the objective function (Ahn 2006).

For defining the problem, cutting tool and milling process parameters such as radius of cutter, feed rate, radial depth of cut, axial depth of cut etc. are introduced to the algorithm. Moreover, the range of variation for each serration parameter like amplitude and wave length is specified. Following these steps, algorithm runs GA for three serration types separately and chooses the best solution among optimum results of each serration.

4.3.4. Genetic Algorithm

The flowchart of the algorithm used in this study is presented in Figure 4.23. The first step in solving any problem with GA is representation of solutions in the form of chromosomes. In this study chromosomes are defined as strings and lengths of these strings depend on features of wave shapes.

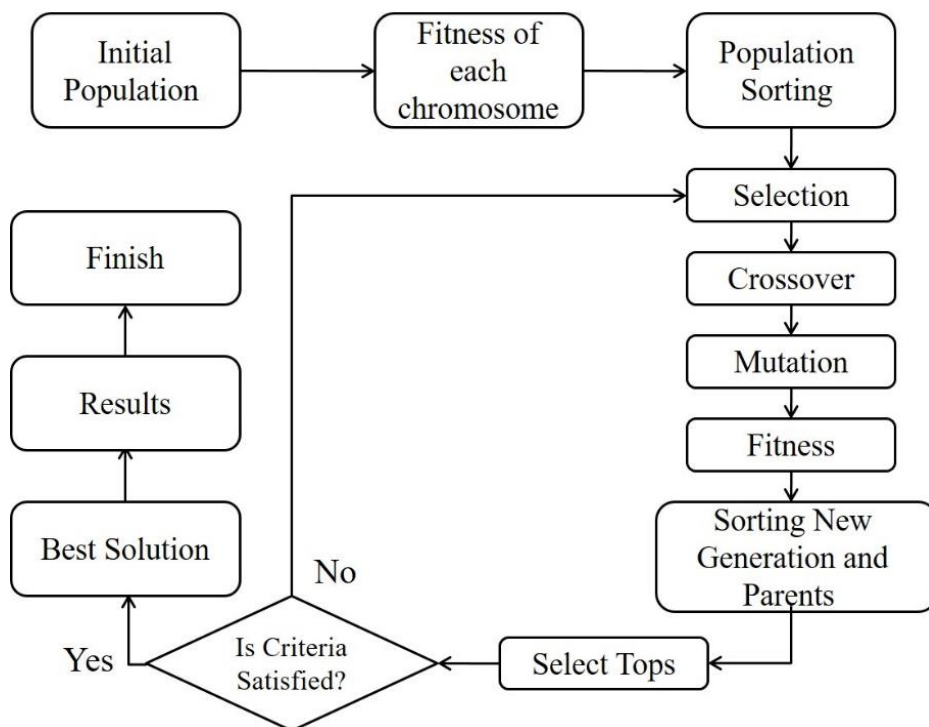


Figure 4.23. Genetic algorithm flowchart

In the next step, the algorithm should generate the initial population. The initial

population can be produced by two ways: random procedure and systematic procedure. Obtained initial population with particular method decreases process time of algorithm but it may cause the algorithm to be trapped at local optimums. Therefore, in this study the initial chromosomes are selected randomly among the feasible ones using the range of parameters. Then, the population should be sorted according to the fitness value of each chromosome. The objective function, $F(u)$, can be defined as any weighted combination of the average or maximum forces in different directions (F_x, F_y, F_z, F_{xy}) and weights can be set according to desire of the problem. Fitness of chromosome u will be calculated by scaling the objective function follows:

$$f(u) = \exp\left[\frac{-\delta \times F(u)}{WC}\right] \quad (4.38)$$

In equation above, δ is a scale factor, $F(u)$ is the value of the objective function for the u^{th} chromosome and WC is the result of worst chromosome in the population. After sorting the population according to the fitness values, chromosomes are selected for crossover and mutation operations by the roulette wheel rule. By using the roulette wheel rule better chromosomes have more chance to participate in crossover and mutation functions.

Crossover function exchanges information between the chromosomes. In the proposed algorithm, single point crossover is used. Cut point is determined randomly on chromosomes of parents and genes before this point are exchanged between parents.

The mutation function selects some genes on the chromosome and changes their values to other feasible ones. This operator helps algorithm to search different areas of solution space and prevents being stuck in local optimums.

Finally, the new offspring which were produced by the mutation and crossover functions (80% of new generations are obtained by the crossover and the remaining 20% are generated by the mutation function) as well as the previous generation are sorted according to the fitness values of chromosomes. Then, the fittest chromosomes are chosen as the new generation. This algorithm is continued iteratively till the results converge to a specific solution.

4.3.5. Results of Optimization

To show the effectiveness of the presented algorithm, it was implemented in MATLAB R2018a®. Some samples have been selected to evaluate the efficiency of the end mills which were designed by the proposed GA algorithm. In these cases, optimum tools were designed for different situations and force simulation results of these tools were compared with normal end mills and standard serrated end mills (which were available in market). The cutting tools in these instances had 4 flutes and the diameter of the tools was 12mm. In addition, Rake and helix angles of the end mills were 5° and 30° respectively. The serration wave of standard serrated end mill was sinusoidal where amplitude is 0.5 mm and wavelength is 2mm. In Table 4.3 different conditions for the simulations and corresponding optimum serrated end mill with sinusoidal serration type are presented.

Table 4.3. Process and corresponding optimum end mill parameters

Sim No.	Optimum Tool Parameters					Process Parameters			
	Tool Type	Tool Dia.	Cutting Angles	Serration Type	Serration Parameters (mm)	Spindle Speed	Depth of Cut (a)	Width of Cut (b)	Feed
1	End Mill	12mm	$\alpha=5^\circ$ $\lambda=30^\circ$	Sinusoidal	A=0.4 WL=7.75	2000 rev/min	45 mm	3mm	0.025 mm/tooth
2				Sinusoidal	A1=0.3 WL=5.5	2000 rev/min	45 mm	3mm	0.2 mm/tooth
3				Circular	A1=A2=0.4 R1=R2=3	2000 rev/min	45 mm	1mm	0.025 mm/tooth
4				Trapezoidal	L1=2, L2=2.5 A=0.35, $\alpha=\beta=45^\circ$ R1=R2=R3=R4=0.2	2000 rev/min	45 mm	1mm	0.2 mm/tooth

As shown in Figure 4.24-a, there is about 45-55% reduction in maximum value of F_{xy} by using optimum serrated tool in comparison with normal end mills. Moreover, optimum designed tools have about 15% better performance in terms of cutting forces against standard serrated end mill. The reasons for this improvement will be explained in the sections that follow. It can be observed in Figure 4.24-b that the drop in milling forces is not as drastic for higher feed rate values as it is for lower feed rate values. Moreover, in some situations, such as in the case of simulation 2, improper selection of serration wave parameters may even result in higher cutting forces in comparison with a normal end mill.

When a standard serrated tool, which has a forward phase shift, is used in high feed rate values, edge forces will not decrease significantly. On the other hand, some portions of the tool with lower or negative values of effective rake angle will be in the cut which increases the cutting force. As a result, while cutting with standard serrated end mills in high feed rates, the average of milling forces is higher than in normal end mills. In simulation 2 as illustrated in Figure 4.24-b, by using optimum serration wave shape cutting forces are reduced. But it is worth mentioning that, even if the phase direction of standard serrated tool changes, while all other serration wave parameters are kept the same, cutting forces will decrease significantly (Figure 4.25-a). As discussed in the previous section, phase shift direction is significant when higher values of feed rate are used. In this condition, the parts of the tool which have higher values of effective rake angle are engaged with the workpiece (Figure 4.25-b).

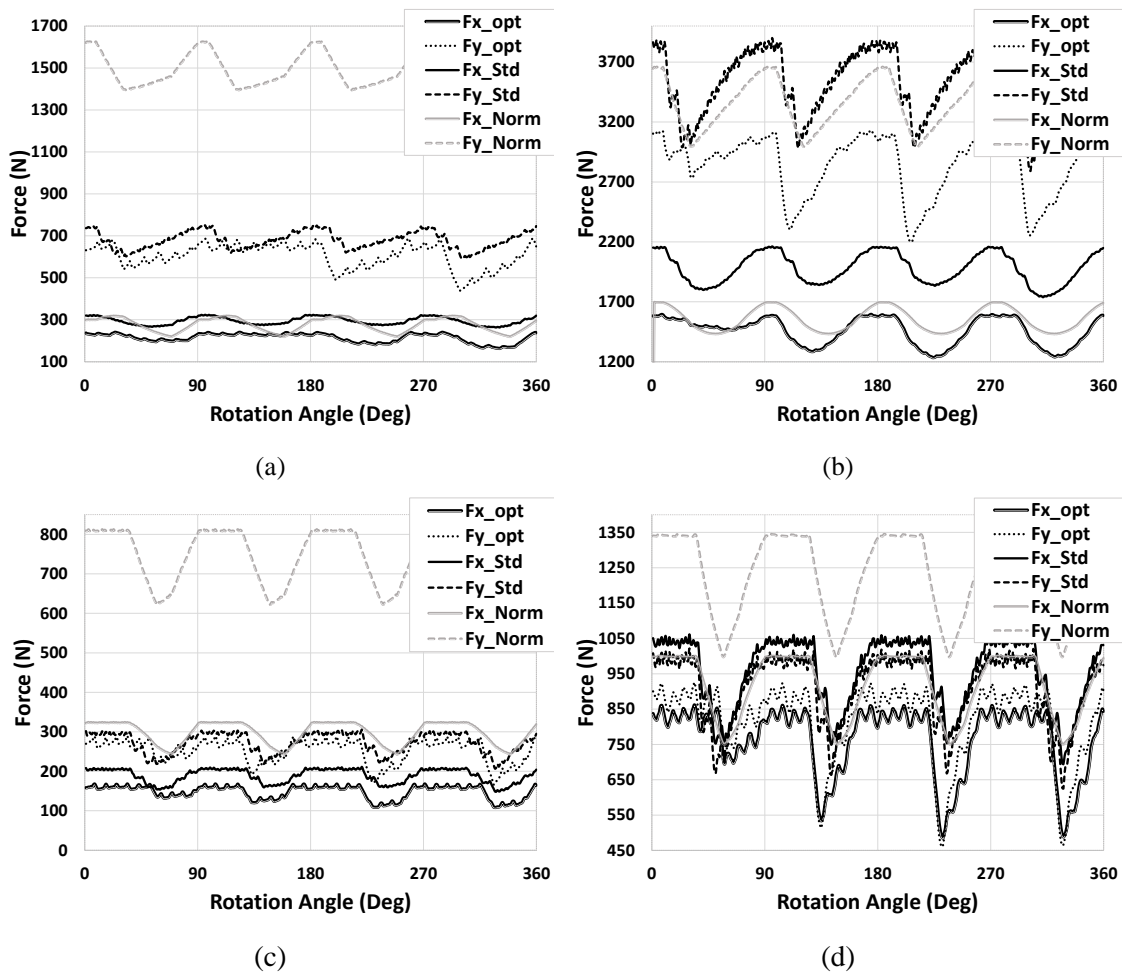


Figure 4.24. Force Simulation Results for optimum, standard serrated and normal end mills for different conditions given in Table 3: a) 1, b) 2, c) 3 and d) 4

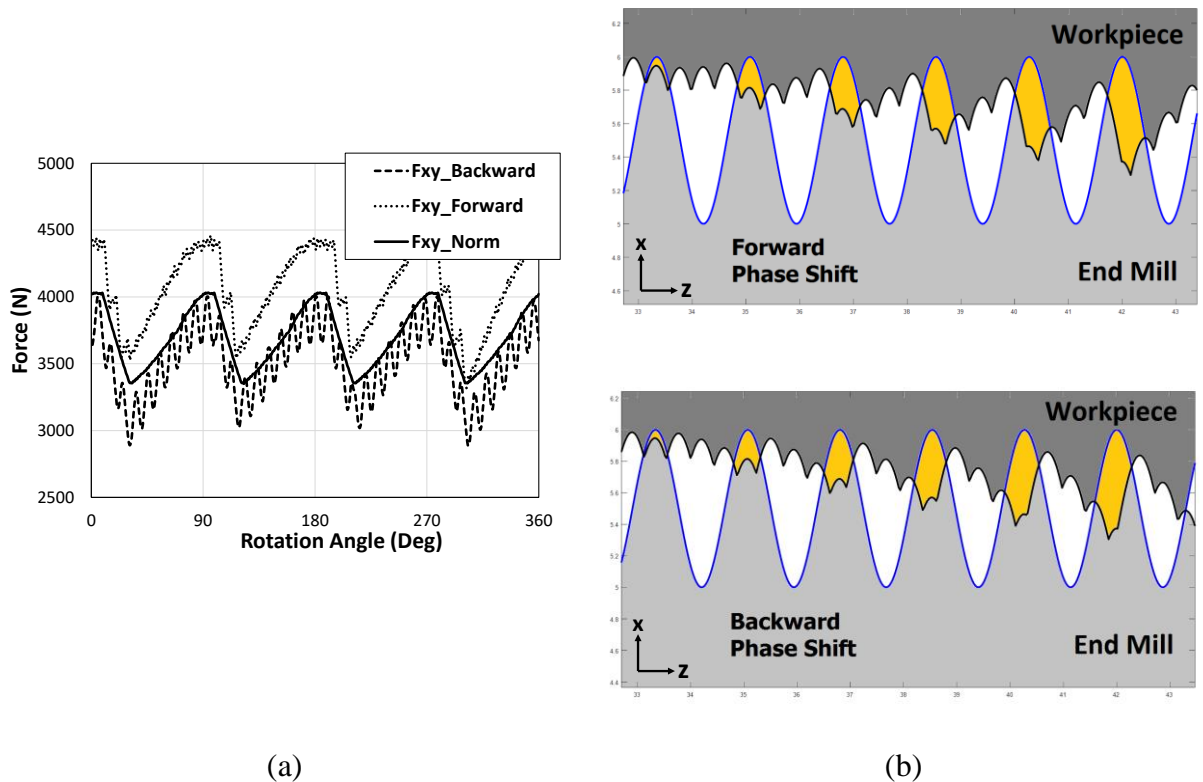


Figure 4.25. Difference between a) cutting forces and b) cutting areas in milling with serrated tools having forward and backward phase shifts.

The width of cut affects the uncut chip thickness for a given milling process, because uncut chip thickness depends on radial immersion angle of the tool. When greater values of width of cut are used, maximum uncut chip thickness will be increased and in this situation effectiveness of serrated tools is decreased. It is the reason behind more of the force reduction when serrated tools are used in comparison with normal end mills in last two simulations.

The optimum tool is the best solution for the specified cutting condition. In addition, it can be considered as a near optimum solution for a range of cutting parameters, which are close to the specified condition.

Another essential point to note is that while comparing the optimization results for different serration types, it is discovered that each serration geometry type converges to almost the same objective function value. For example, the optimum circular and trapezoidal serration wave types in simulation 1 (Table 4.3) result in similar milling forces to the ones with the optimal sinusoidal serration. Geometrical parameters for these tools are given in Table 4.4 whereas the cutting forces are illustrated in Figure 4.26. Thus, similar force reduction, and thus similar performance increase can be achieved with different serration types provided that their

geometric parameters are optimized. Moreover, the results show that, independent from the serration type, two most important parameters in serration geometry, namely the length and the amplitude of the optimum wave shapes are very similar.

Table 4.4. Optimum tools with different serration types for same condition

Optimum Tool Parameters					Process Parameters			
Tool Type	Tool Dia.	Cutting Angles	Serration Type	Serration Parameters (mm)	Spindle Speed	Depth of Cut (a)	Width of Cut (b)	Feed
End Mill	12mm	$\alpha=5^\circ$ $\lambda=30^\circ$	Sinusoidal	A=0.4 WL=7.75	2000 rev/min	45 mm	3mm	0.025 mm/tooth
			Circular	A1=A2=0.4 R1=R2=5.25				
			Trapezoidal	L1=1.2, L2=1.2 A=0.4, $\alpha=\beta=60^\circ$ R1=R2=R3=R4=0.75				

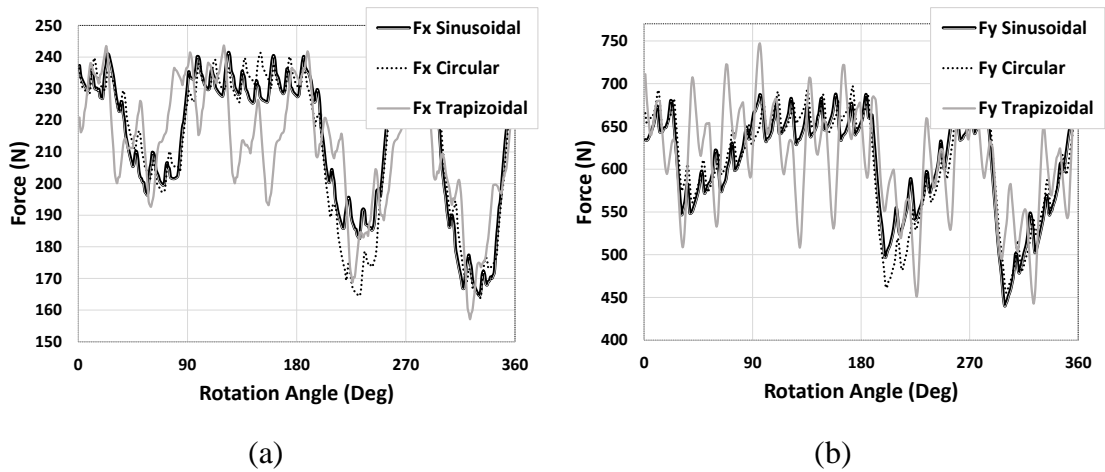


Figure 4.26. Cutting forces with the optimum tools having different serration types given in Table 4.4 a) x and b) y direction

4.3.6. Efficiency of Optimization in Different Conditions

Optimization results show that the efficiency of the optimum serrated end mill changes

and depends on the cutting parameters. Therefore, prediction of efficiency of the optimum becomes an important issue. DOE method is used to investigate the efficiency of optimized serrated end mills in different cutting situations. The difference between cutting forces of optimum serrated and normal end mills, in x-y direction, is considered as the response function. The response is analyzed by considering depth of cut, width of cut and feed rate in 3, 5 and 5 levels, respectively. The main and interaction effects of these factors are illustrated in Figure 4.27 and Figure 4.28 respectively.

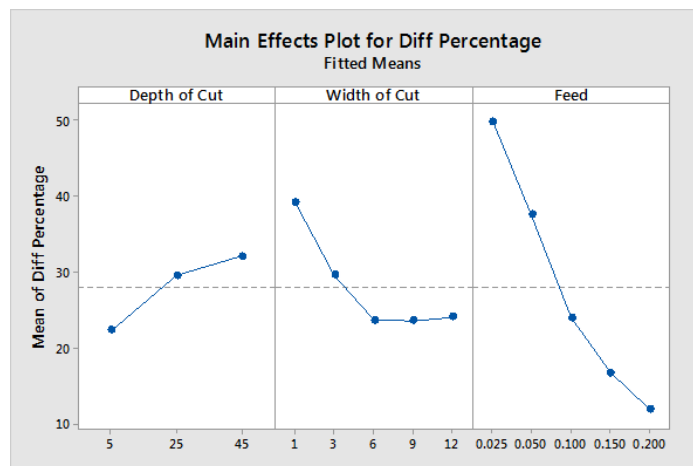


Figure 4.27. Plots of cutting condition parameters main effects on the efficiency of the optimization

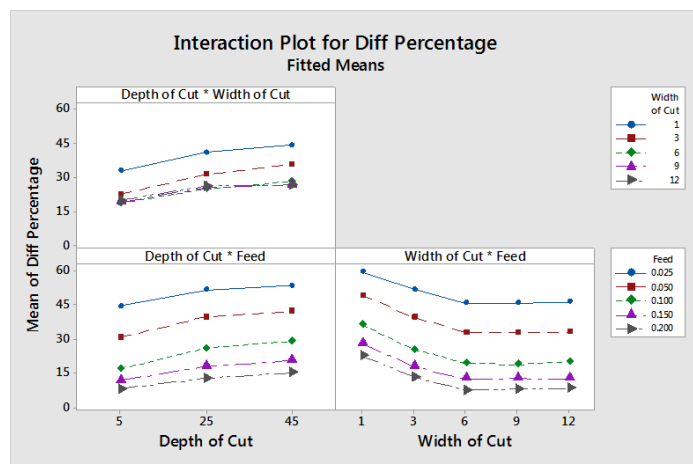


Figure 4.28. Plots of cutting condition parameters interaction effects on the efficiency of the optimization

By decreasing the depth of cut, due to the lower engaged cutting-edge length, the number

of in-cut serration waves is decreased. This will result in varying material removal rate for different edges and unbalanced cutting forces. This issue is much more significant in higher feed values. An example of this situation is illustrated in Figure 4.29. As it is shown in the figure, cutting forces for each tooth vary significantly and maximum of cutting forces for serrated end mill is higher than the value for a normal tool.

The optimization algorithm in low depth of cuts proposed serration waves with lower wave lengths, to avoid unbalanced forces. This means less reduction of cutting forces in lower depths of cut in comparison with higher depths. Therefore, the efficiency of the optimum serrated tools will be more obvious in higher depths of cut (Figure 4.27).

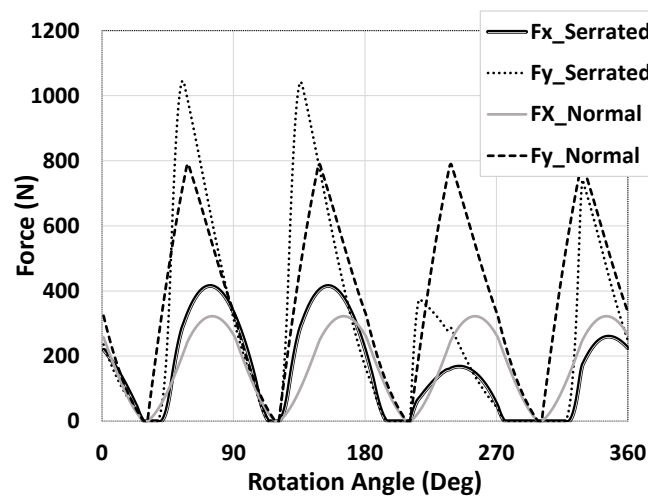


Figure 4.29. Unbalanced Force in cutting low depth of cut with high serration wave length

As discussed in the previous section, the efficiency of the serrated end mills is dependent on the uncut chip thickness and they are much more effective in cutting with low uncut chip thickness values. This is due to the fact that when the thickness of the uncut chip rises, a larger portion of the serrated edge becomes immersed in the material. As a result, total contact length increases, or, to put it another way, total contact length does not decrease as much as it does when feed rates are lower. As a result, in line with our expectation, the main effect plot of feed rate for effectiveness of serrated end mills is decreasing function (Figure 4.27 and Figure 4.28).

The average of uncut chip thickness is maximum in the half immersion cuttings (in our case 6 mm of width of cut). Therefore, as illustrated in Figure 4.27 the main effect of the

width of cut on efficiency of serrated end mill is minimum in 6mm.

4.3.7. Effects of Cutting Parameters on Optimum Serration Shape

In this section based on the optimization results, effects of cutting parameters on optimum serration wave shape is studied. The aim of this section is providing some recommendations for choosing the best tool among available tools for desired cutting processes. Therefore, effects of the depth of cut and feed rate are investigated on optimum values of main parameters of the serration waves. The radial depth of cut is not considered, because it affects maximum chip thickness and its effects are similar to that of feed rate. In order to analyze these effects, DOE method is used. Wavelength and amplitude of optimum serration shape is considered as the response function. The response is analyzed by taking depth of cut and feed rate into account in 3 and 5 levels, respectively. Figure 4.30 shows the main and interaction effects of factors on the serration wave shape.

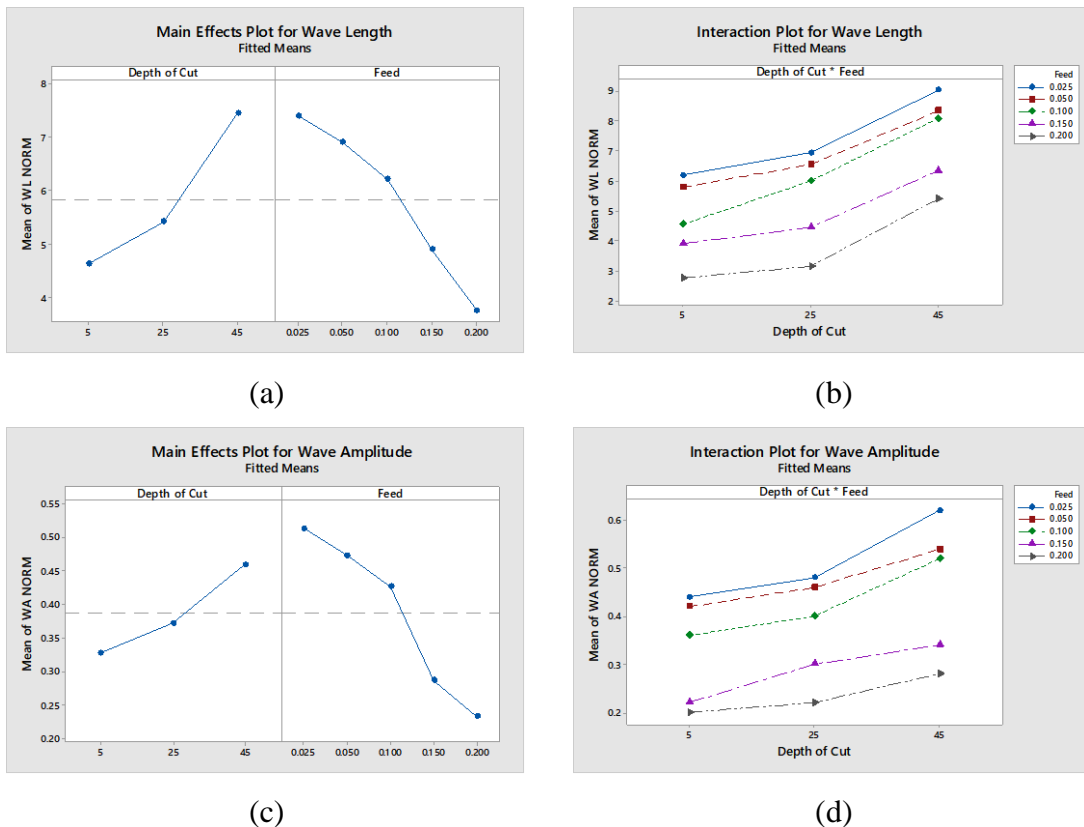


Figure 4.30. Main and interaction effects of cutting parameters on serration wave shape

Results show that, in low depth of cuts as discussed before low wave lengths are preferred

to avoid unbalanced forces. In high depths higher values of the wavelength are used. This is because, by using greater wave lengths, the contact length and thus the edge forces are decreased. Moreover, high values of wave lengths result in higher tool life as stress concentration is reduced on the cutting edges.

For low feed rates, high values of wave lengths are chosen as an optimum solution to decrease the contact length. But for high feed rates, this reduction is not significant (as discussed in previous section). Therefore, lower values of wave lengths are chosen as optimum solution which has more drastic changes in local rake values and this is the dominant phenomenon in force reduction.

Finally, the amplitude of the serration waves should be proportional to wave length. Using high amplitudes with low wavelengths increases the contact length. Moreover, it results in high stress concentration on the tool edge. However, choosing low amplitudes with high wavelengths decrease the effectiveness of the local cutting angles.

4.4. Chatter Stability of Serrated End Mills

In this section, dynamic behaviors of the end mill with optimal serration shape (which is optimized considering cutting forces), standard serrated tools and regular end mill are compared. Milling operation stability is based on dynamically variable chip thickness, which is a consequence of both present and previous vibration marks left on the cut surface. The milling system is considered as two orthogonal degree of freedom to analyze stability as shown in Figure 4.31.

Because of the presence of multiple delay in the system as discussed in previous chapter, First Order Semi Discretization method (Tamás Insperger and Stépán 2011) and time-averaged coefficient matrices (Sims, Mann, and Huyanan 2008) are used in analyzing chatter stability of serrated end mills. Required changes for the method applied to serrated end mills (Koca 2012) and this method is used to investigate the effect of optimization on the stability limits.

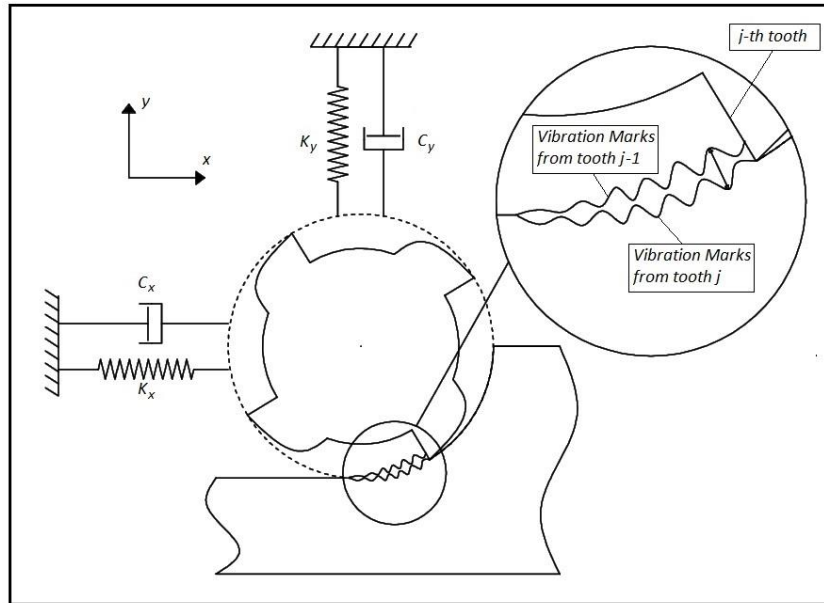


Figure 4.31. Two orthogonal degree of freedom system and dynamic chip thickness

The modal parameters given in Table 4.5 are used to compare the tools in terms of chatter stability.

Table 4.5. Modal parameters of the investigated system

ω_{nx} (rad/ sec)	m_x (kg)	ζ_x	ω_{ny} (rad/ sec)	m_y (kg)	ζ_y
$693*2\pi$	0.8409	%2.503	$689*2\pi$	0.9372	%2.947

The comparison of the tools stability behavior are shown in Figure 4.32. In this simulations Al7075 is chosen as workpiece material and the process is quarter immersion down milling with 0.05 mm/(rev.tooth) of feed rate.

As it can be seen from Figure 4.32, the optimal serrated end mill, because of the effective depth of cut reduction, shows much better stability performance over the standard serrated and normal end mill.

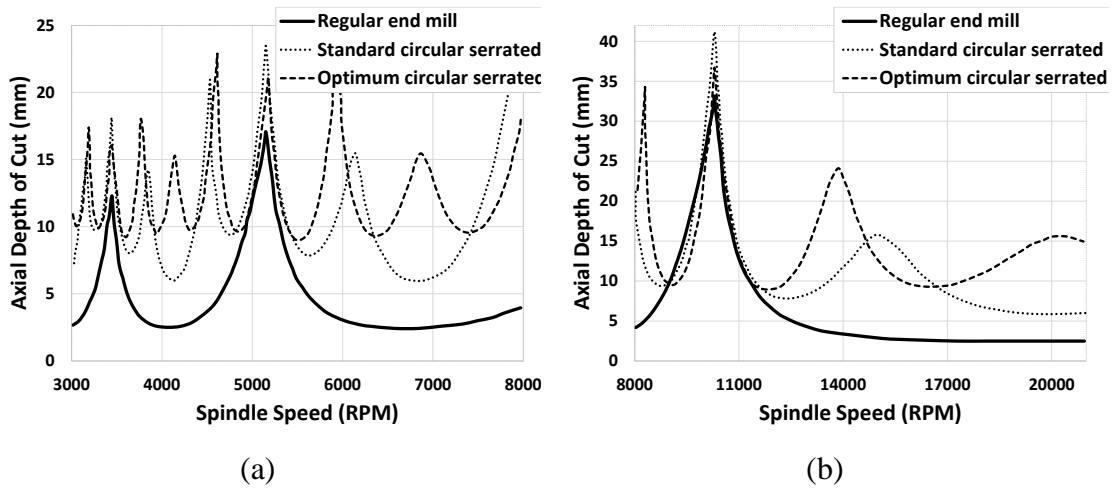


Figure 4.32. Comparisons of stability diagrams ($f_t=0.05\text{mm/tooth}$) a) 3000-8000 RPM
b) 8000-21000 RPM

In Figure 4.33 stability diagrams obtained for higher feed rate (0.15mm/tooth) are shown. Because of the increase in the feed per tooth, the effectiveness of serration waves decreases (Figure 4.27). But optimized serrated end mills still have higher stability limits compared to the standard serrated and normal end mills.

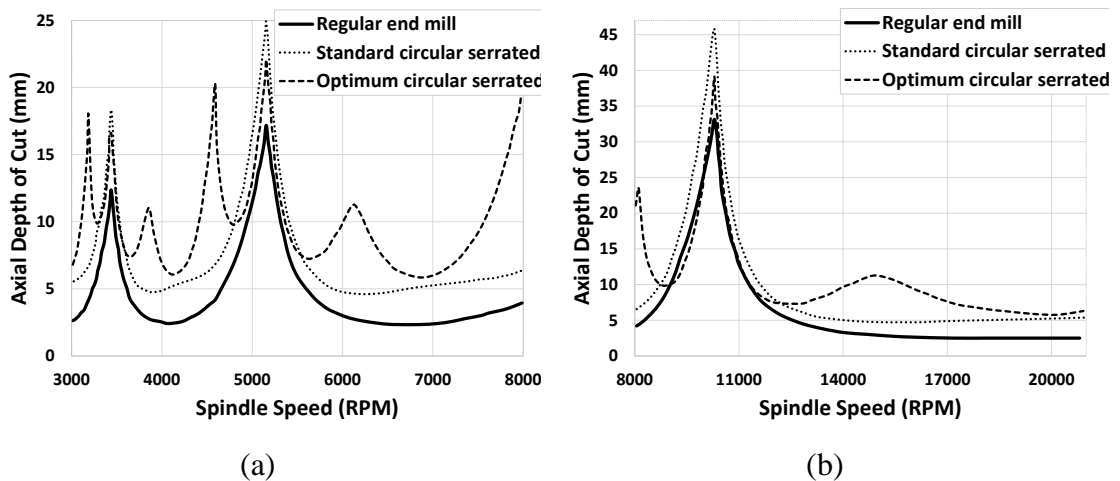


Figure 4.33. Comparisons of stability diagrams ($f_t=0.15\text{mm/tooth}$) a) 3000-8000 RPM
b) 8000-21000 RPM

In Figure 4.34, three different optimized serrated forms are compared for the same given milling scenario with 0.05mm/rev.tooth of feed rate. It is shown that if the serration geometry is optimized, the same amount of stability increase can be achieved regardless of the wave type.

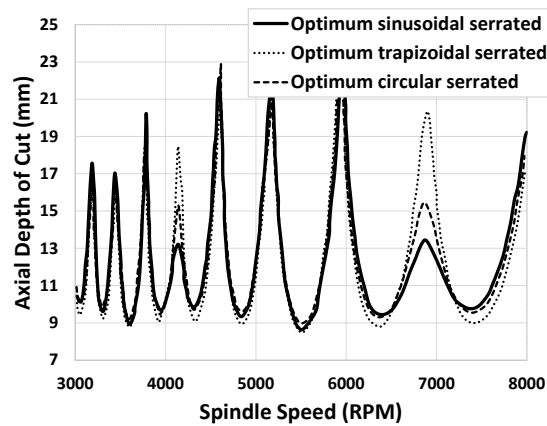


Figure 4.34. Stability comparison of different optimized serration profiles

4.5. Conclusions

Present chapter investigates mechanics and dynamics of milling with serrated end mills. In order to decrease cutting forces, optimum tools are designed by using GA. Results show that these tools have lower cutting forces and higher stability limits in comparison with standard serrated tools. The specific contributions and conclusions are listed in the following.

- For the first time in the literature, different types of end mills (normal, ball nose, round nose and tapered end mills with constant or variable pitch and/or helix angles) with various serration types are modeled.
- Milling forces are modeled and verified experimentally. Chip thickness and cutting force coefficients (considering local cutting angles) are calculated in an accurate way which has resulted in accurate force predictions.
- The effects of serration geometry and phase shift on the local rake and oblique angles, and cutting forces are discussed and demonstrated. It is demonstrated that the serration phase shift has a very strong effect on the cutting mechanics and the forces, and thus has to be selected correctly. Results show the phase shift direction of serrations may change the cutting forces up to 35%.
- Different serration waveforms are optimized to minimize milling forces for various cutting conditions. It is demonstrated that cutting forces can be reduced

significantly using optimum serration geometry against standard ones available in the market. Experimental and simulation results illustrate that optimum tool can reduce cutting forces up to 30% in comparison with standard serrated tools. Furthermore, it is shown that, very similar performance increase, i.e. force reduction, can be achieved with all serration types if their parameters are optimized. This result is important as it allows flexibility in selection of the wave form considering issues such as tool manufacturing, surface quality, wear etc.

- The effect of serration geometry on the dynamics of milling process is explained, and it is shown that in addition to cutting force reduction, the optimized serrated end mills achieve better performance over standard serrated end mills in terms of chatter stability, as well. It is shown that, the stability limit of optimized tool can be as high as 3 times that of standard serrated end mills at certain speeds. It is also illustrated that; the same amount of stability increase can be obtained regardless of the wave type for optimized serrated tools.

In summary, optimization of the serrated tools considering their dynamic behavior can improve their performance significantly. In future works, the outcomes of this study can be used in similar processes such as turn-milling. These tools can also be used to enhance robotic milling where reduction of cutting forces and improvement of stability are important role due to low rigidity of robots. In future studies, similar approaches can be used in investigating mechanics and dynamics of other special milling cutters such as crest-cut tools for their optimization.

5. APPLICATION OF SPECIAL TOOLS IN DIFFERENT PROCESSES

5.1. Special End Mills in Robotic Milling

In robotic milling, unlike normal milling, the dynamic modes from the machine have low frequencies and high amplitudes. Due to the high vibration amplitudes, the fluctuation in cutting forces increases to very high levels during chatter, which damages the part surface, tool surface, spindle, and robot axes. Therefore, the application of special end mills in robotic milling can be a solution to avoid chatter vibration during the process.

As can be seen in the stability diagrams simulations and experimental verifications performed for robotic milling (Cordes, Hintze, and Altintas 2019), the curve showing stable cutting conditions consists of the curve representing the common stable cutting depth obtained by cutting tool and robot modes. For example, as illustrated in Figure 5.1, there are four curves that construct stability lobe diagrams which consist of stability limits obtained for different tool and robot modes, and the global stability lobe diagram is the common stability limits of all modes. Considering the results, the stability diagram is divided into different areas in terms of the active mode.

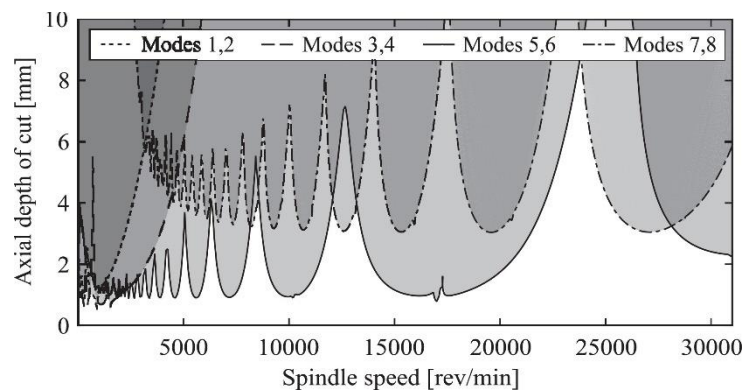


Figure 5.1 Stability diagram for the robotic milling system

Moreover, another study (Gonul, Sapmaz, and Tunc 2019) shows that robot vibration frequencies will not change significantly in a sample milling process by changing the position of arms. Therefore, it can be said that cutting tools designed according to the relevant vibration modes can be used as a valid and reasonable solution for a wide area where the robot will work.

Special end mills such as variable pitch end mills are used in order to suppress chatter vibration during the milling process. Because of the low natural frequencies in robot modes, the wavelength of the undulations left on the surface (Figure 3.9), which are a function of the cutting speed and the vibration frequency, is large. This issue should be considered in the design and application of the special end mills; otherwise, they cannot affect the process positively.

In this chapter, optimum variable pitch tools will be designed to increase chatter stability where robot modes are active and affect stability limits.

5.1.1. Optimization of Variable Pitch Tools for Robotic Milling

In this section, non-constant pitch end mills are designed using the optimization method proposed by Budak (E. Budak 2003a; 2003b). Optimized end mills stability diagrams extracted by semi-discretization method including multiple delays introduced in section 3.3, and the stability limits of the optimized tools will be compared with normal end mills. As discussed in previous chapters, the main difference in the stability analysis of end mills with variable pitch angles is that the delay between the inner and the outer waves is different for each edge (ε_j).

$$\varepsilon_j = \omega_c T_j \quad j = 1, 2, \dots, N \quad (5.1)$$

In the proposed optimization method by Budak (E. Budak 2003a; 2003b), the directional coefficients are obtained by the average value of the pitch angles to simplify formulations.

The characteristic equation for normal end mills (E. Budak and Altıntaş 1998a) can be used for the variable pitch end mills with necessary changes according to the following equation:

$$\Lambda = \frac{1}{4\pi} aK_t \sum_{j=1}^N (1 - e^{i\omega_c T_j}) \quad (5.2)$$

Using Equation (5.2), the stability limit can be determined as:

$$a_{lim} = \frac{-4\pi}{K_t} \frac{\Lambda}{N - \sum_{j=1}^N \cos(\omega_c T_j) + i \sum_{j=1}^N \sin(\omega_c T_j)} \quad (5.3)$$

Stability limit is a real number, and eigenvalue can be complex. Therefore, the denominator of equation (5.3) should be equal to zero:

$$N - \sum_{j=1}^N \cos(\omega_c T_j) = \sum_{j=1}^N \sin(\omega_c T_j) \frac{\Lambda_R}{\Lambda_I} \quad (5.4)$$

Considering equation (5.4), the stability limit can be obtained as:

$$a_{lim} = \frac{-4\pi}{K_t} \frac{\Lambda_I}{\sum_{j=1}^N \sin(\omega_c T_j)} \quad (5.5)$$

This equation shows that in order to maximize the stability limit, the absolute value of the denominator should be minimized, and the main idea behind this method is based on this relation. The denominator can be stated as follow:

$$S = \sum_{j=1}^N \sin(\varepsilon_j) = \sin(\varepsilon_1) + \sin(\varepsilon_2) + \dots + \sin(\varepsilon_j) \quad (5.6)$$

Due to pitch variation, the phase angle is different for each tooth and can be obtained by

the following equation:

$$\varepsilon_j = \varepsilon_1 + \Delta\varepsilon_j \quad (j = 2, \dots, N) \quad (5.7)$$

where $\Delta\varepsilon_j$ is the phase difference between tooth j and first tooth corresponding to the difference in the pitch angles between these teeth.

The number of vibration waves (n) in one cutter revolution can be calculated by the following equation:

$$n = \frac{\omega_c}{\Omega} \quad (5.8)$$

where Ω is the spindle speed (rad/sec). θ is defined as the corresponding immersion angle for one full vibration wave and calculated by:

$$\theta = \frac{2\pi}{n} = \frac{2\pi\Omega}{\omega_c} \quad (5.9)$$

Therefore, the pitch angle variation ΔP corresponding to $\Delta\varepsilon$ can be obtained by:

$$\Delta P_j = \frac{\theta}{2\pi} \Delta\varepsilon_j = \frac{\Omega}{\omega_c} \Delta\varepsilon_j \quad (5.10)$$

According to the mentioned equations, pitch variation can change the value of the S in equation (5.6), and this value can be minimized by selecting the proper value of pitch variation.

Improvement in the stability using variable pitch tools over standard end mills can be investigated by the ratio of the stability limits. The stability limit for the normal end mill is calculated by the following equation:

$$a_{limnorm} = -\frac{4\pi}{K_t} \frac{A_l}{N \sin(\omega_c T)} \quad (5.11)$$

Therefore, the stability ratio between normal and variable pitch end mill calculated by:

$$r = \frac{a_{lim_{vp}}}{a_{lim_{norm}}} = \frac{N \sin(\omega_c T)}{\sum_{j=1}^N \sin(\omega_c T_j)} = \frac{N \sin(\omega_c T)}{S} \quad (5.12)$$

There are many solutions to the minimization of S . For example, for an even number of teeth, assuming $\Delta \varepsilon_j = \pi j$, the value of the S becomes zero. This can easily be applied by using linear or alternating pitch variation in normal milling where natural frequencies are high enough.

For linear pitch alternation ($P_0, P_0 + \Delta P, P_0 + 2\Delta P, \dots$), the value of the r can be calculated for different values of the ε_1 and teeth number, which is illustrated in Figure 5.2-Figure 5.4.

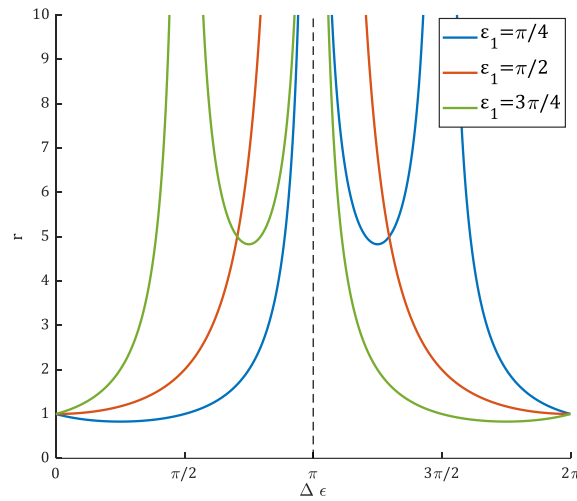


Figure 5.2. r value for 2-flute end mill with linear pitch variation

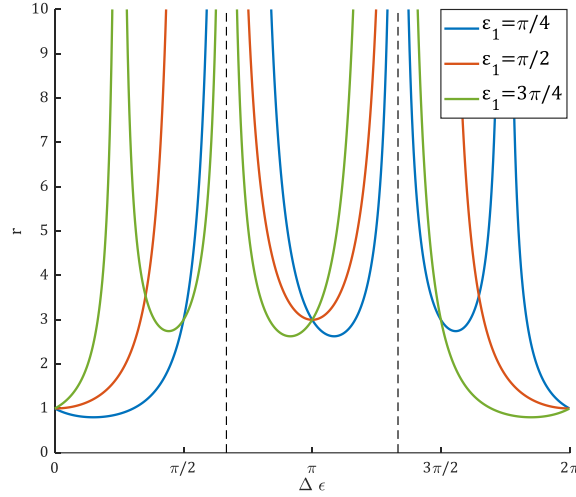


Figure 5.3. r value for 3-flute end mill with linear pitch variation

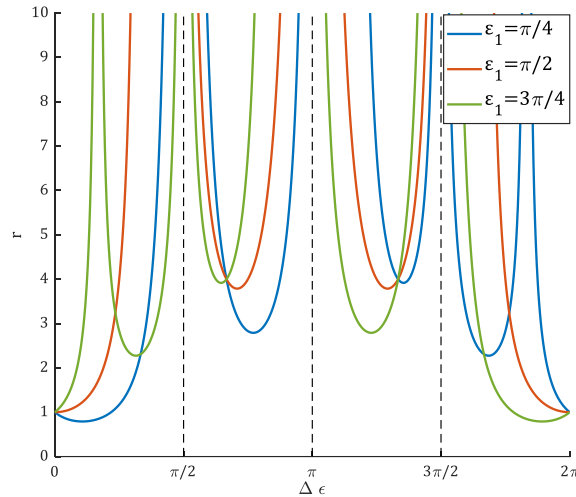


Figure 5.4. r value for 4-flute end mill with linear pitch variation

According to Figure 5.2, for the tools with two teeth, the optimum value for the $\Delta\epsilon$ is equal to π . Also, as it is illustrated in Figure 5.3, there are two optimums $\Delta\epsilon$ value for tools with 3 teeth and they are equal to $\frac{2\pi}{3}, \frac{4\pi}{3}$. These values for the tool with 4 teeth are equal to $\frac{\pi}{2}, \pi, \frac{3\pi}{2}$, as demonstrated in Figure 5.4.

But the main problem in robotic milling is that natural frequencies are low, and because of this issue, the number of vibrations is low, too (equation (5.8)). Therefore, the scaling factor between $\Delta\epsilon$ and ΔP in equation (5.10) is higher than the value of this factor in normal milling. As a result, pitch variations calculated by these solutions generally are

very high and they are not applicable in robotic milling. Therefore, feasible values for $\Delta\varepsilon$ are calculated considering maximum value for ΔP which determined by tool manufacturer considering manufacturing limitations. Moreover, in the determination of the maximum pitch variation the changes in the chip thicknesses for each edge should be considered.

$$\Delta\varepsilon_{max} = \frac{2\pi}{\theta} \Delta P_{max} = \frac{\omega_c}{\Omega} \Delta P_{max} \quad (5.13)$$

According to equation (5.13), $\Delta\varepsilon_{max}$ has direct and inverse relationship with chatter frequency and spindle speed, respectively. Optimization in each situation using this method is possible when $\Delta\varepsilon_{max}$ is higher than at least one of the optimum values of $\Delta\varepsilon$ which obtained for different tools. For example, consider a situation where the natural frequency is 40Hz, and the maximum pitch variation is 30 degrees for a tool with two cutting edges. In this situation, for different desired spindle speeds, we have different scenarios:

- $\Delta\varepsilon_{max} \leq \Delta\varepsilon_{opt}$
 $\Omega \geq \omega_c \frac{\Delta P_{max}}{\Delta\varepsilon_{opt}}$

If spindle speed is equal to 800 rpm, calculated $\Delta\varepsilon_{max}$ ($2\pi/3$) is lower than $\Delta\varepsilon_{opt}$ (π) and the feasible area is not covered optimum point (Figure 5.5). In this situation, it is not possible to suppress chatter vibration in robot mode with a variable pitch tool.

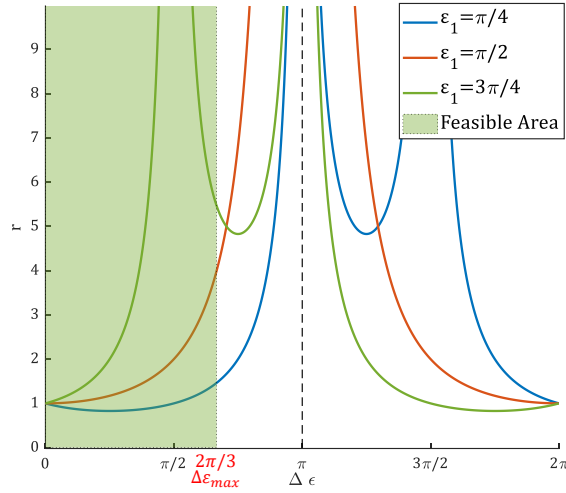


Figure 5.5. Feasible area for choosing pitch variation in 800 rpm for the 2-flute tool with the natural frequency of 40Hz

- $\Delta\varepsilon_{max} \geq \Delta\varepsilon_{opt}$
 $\Omega \geq \omega_c \frac{\Delta P_{max}}{\Delta\varepsilon_{opt}}$

If spindle speed is equal to 400 rpm, calculated $\Delta\varepsilon_{max}$ ($4\pi/3$) is greater than $\Delta\varepsilon_{opt}$ (π) and the feasible area is covered optimum point (Figure 5.6). In this situation, chatter vibration in robot mode can be suppressed with a variable pitch tool. By decreasing spindle speed feasible area for $\Delta\varepsilon$ (green area) is increased, and we will have a wider range to find optimum pitch variation.

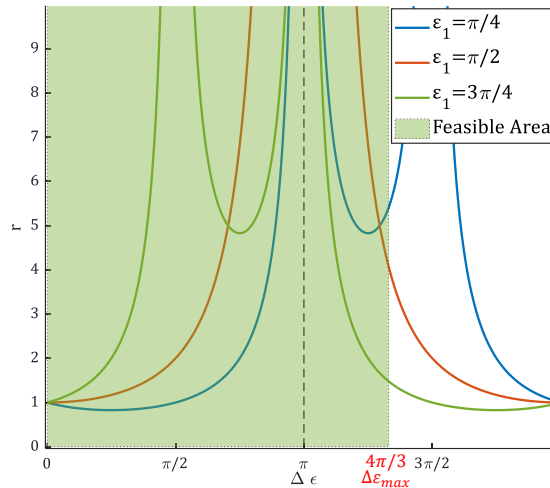


Figure 5.6. Feasible area for choosing pitch variation in 400 rpm for the 2-flute tool with the natural frequency of 40Hz

5.1.2. Case Study

As a case study, the robot with modal parameters presented in Table 5.1 is investigated, and optimum tools for different situations are designed. Moreover, stability limits for designed tools will be analyzed with the method which is presented in previous chapters.

Table 5.1 Model parameters of the robot

	ω_n (rad/sec)	K (N/m)	% ζ
x direction	19.88	3.65e6	0.81
y direction	17.8	2.31e6	1.76

5.1.2.1. Design of Optimum End Mill with 4 Teeth

For the cutting tool with four edges, the minimum value of the $\Delta\varepsilon_{opt}$ is equal to $\frac{\pi}{2}$. In addition, the maximum feasible pitch variation is determined as 30 degrees. By considering these issues and modal parameters of the robot, the range of the spindle speed which can be suppressed by the tool can be obtained by the following equation as 0-350

RPM:

$$\Omega_{max} = \omega_c \frac{\Delta P_{max}}{\Delta \varepsilon_{opt}} \quad (5.14)$$

Optimal pitch variations for each spindle speed are calculated and illustrated in the following figure.

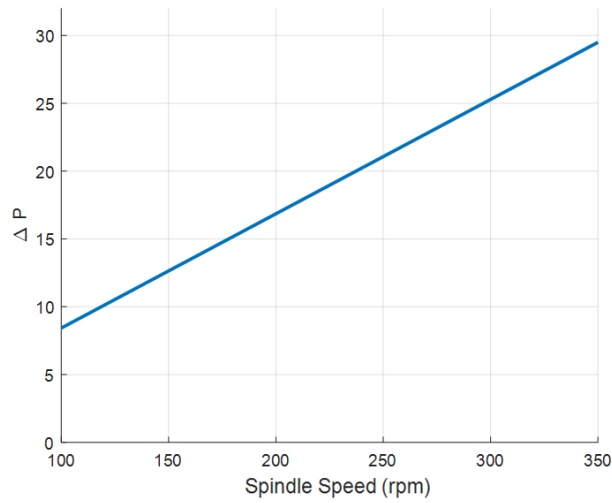


Figure 5.7. Optimum pitch variation for each spindle speed using the 4-flute end mill

In order to verify these results, stability limits are obtained with SDM, which is presented in section 3. The stability lobes for the given condition in Table 5.1 for half immersion milling of AL7075 using four flute normal end mill with 30° helix angle is shown in Figure 5.8.

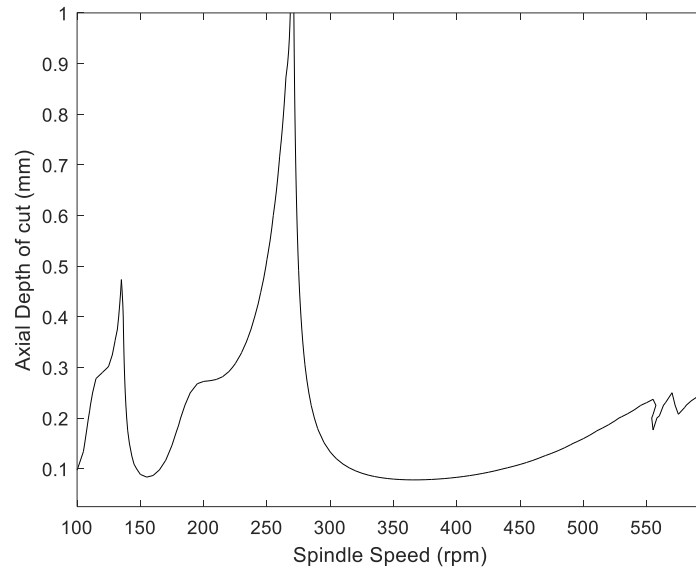


Figure 5.8. Stability lobes for normal end mill with four cutting edge

The stability lobe diagram for the variable pitch tool, which was designed for 150rpm ($\Delta P = 12.5^\circ$), is shown in Figure 5.9. This figure shows that in 150 rpm, the stability limit increases by five times in comparison with the normal end mill.

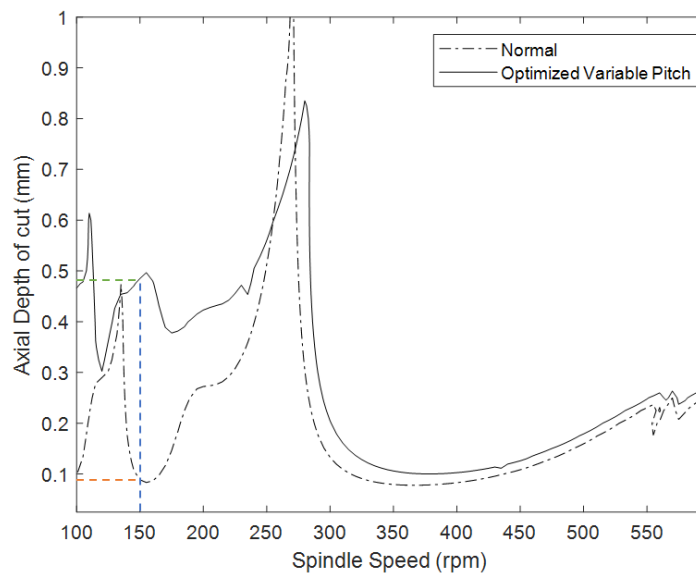


Figure 5.9. Stability lobes for variable pitch 4-flute end mill optimized for 150RPM

The stability lobe diagram for the variable pitch tool, which is optimized for 350rpm

($\Delta P = 30^\circ$), is demonstrated in Figure 5.10. This figure shows that in 350rpm the stability limit increased to a five of its former value with normal end mills. Moreover, the results show that pitch variation not only affects the stability limit on the desired spindle speed and increases the average value of the limits in its neighborhood.

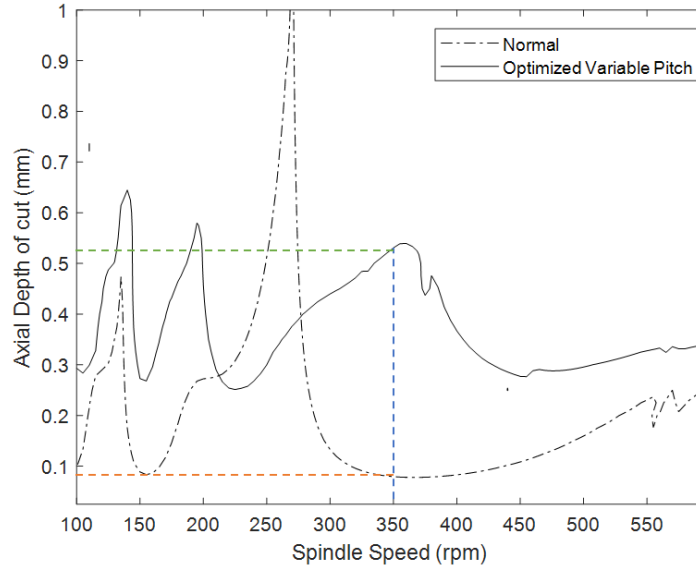


Figure 5.10. Stability lobes for variable pitch 4-flute end mill optimized for 350RPM

5.1.2.2. Design of Optimum End Mill with 3 Teeth

For the 3-flute cutting tool, the minimum value of the $\Delta\varepsilon_{opt}$ is equal to $\frac{2\pi}{3}$. In addition, the maximum feasible pitch variation is considered 40 degrees. The range of the spindle speed which can be suppressed by the tool is calculated by equation (5.14) as 0-350 rpm. Optimal pitch variations for each spindle speed are obtained and shown in Figure 5.11.

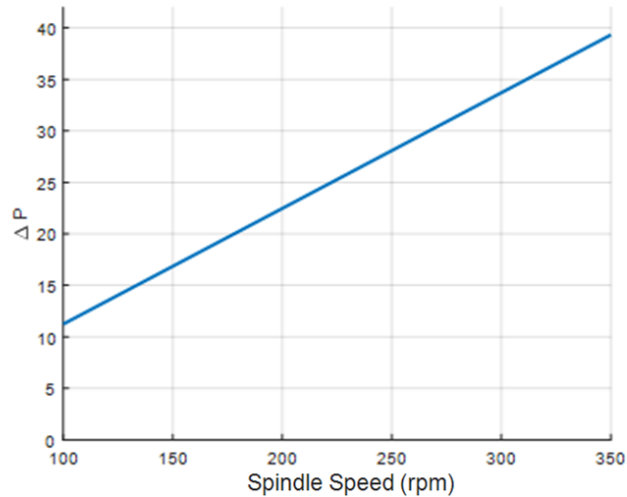


Figure 5.11. Optimum pitch variation for each spindle speed using the 4-flute end mill

The stability lobe diagram for the variable pitch tool with three edges, which was designed for 130rpm ($\Delta P = 14.5^\circ$), is shown in Figure 5.12. This figure shows that using the optimum variable pitch tool at 130rpm increases the stability limit by 600% in comparison with the normal end mill.

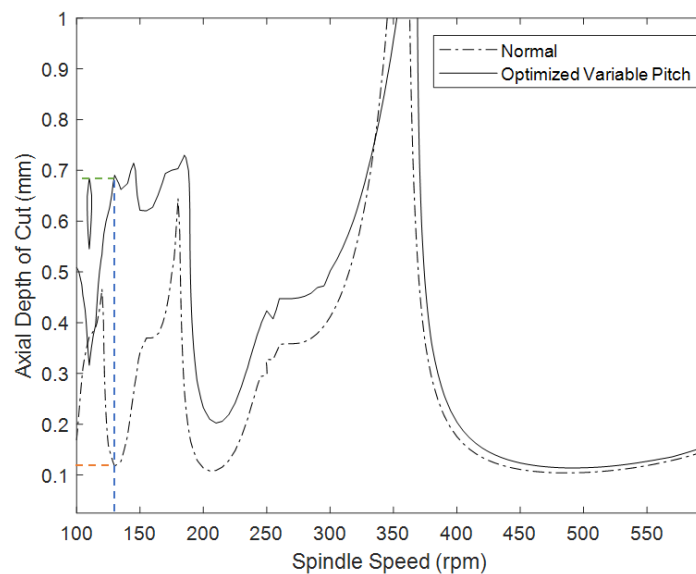


Figure 5.12. Stability lobes for variable pitch 3-flute end mill optimized for 130RPM

The stability lobe diagram for the variable pitch tool, which is optimized for 200 RPM ($\Delta P = 22.5^\circ$), is demonstrated in Figure 5.13. According to this figure, in 200 RPM, the stability limit increases from 0.12mm to 0.65mm in comparison with the normal end mill.

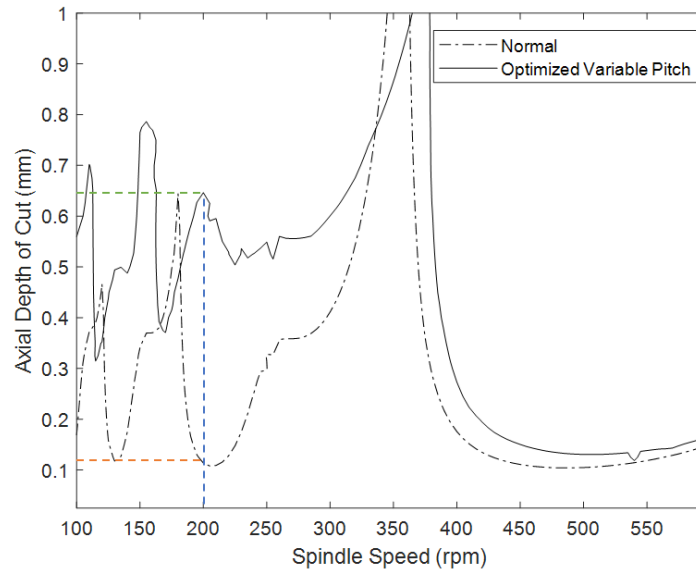


Figure 5.13. Stability lobes for variable pitch 3-flute end mill optimized for 200RPM

The results show that it is possible to suppress chatter vibration in robot modes for low spindle speeds where the range of feasible spindle speed depends on the chatter frequency and maximum value of the possible pitch variation (Figure 5.14).

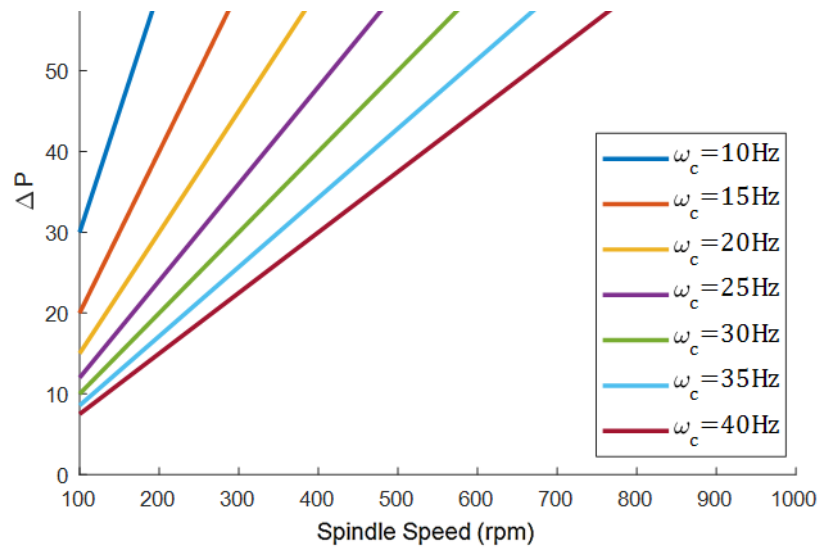


Figure 5.14. Variation of the optimum pitch for each spindle speed in different chatter frequencies

Moreover, in robotic milling at low spindle speeds using cutters with higher diameters

can improve the dynamic performance of the process. The use of tools with larger diameters makes it possible to manufacture higher pitch variations on the tool due to higher free spaces available between edges. In addition, the larger diameter of the tool makes it possible to cut with low spindle speeds when higher cutting speeds are needed.

5.1.3. Application of The Crest-cut End Mills in Robotic Milling

As illustrated in previous chapters, crest-cut end mills can improve the dynamic performance of the milling processes. The effect of the use of these tools in the dynamics of robotic milling will be investigated in this section. The conditions which are used in section 5.1.1 (half immersion milling of AL7075 using four flute end mill with 30° helix angle) are repeated here with different crest-cut tools, and the results were compared with normal end mills.

In Figure 5.15, the effect of the crest-cut tools on the stability limits for the condition described in section 5.1.1 and Table 5.1 is illustrated.

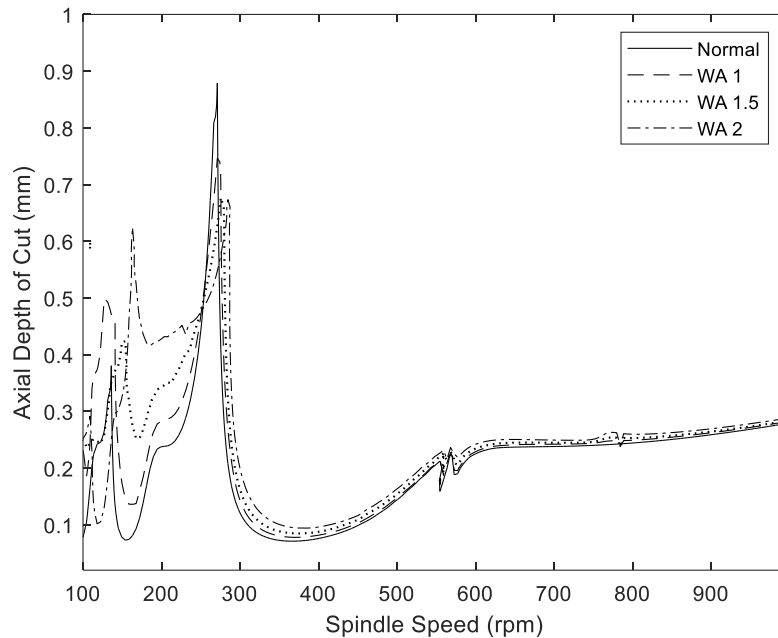


Figure 5.15. Stability lobes for crest-cut end mills with different wave amplitudes (half immersion)

As shown in the figure, the crest-cut end mill affects the stability limits in very low spindle speed. The reason is that robotic milling in a given condition is stable in a very low depth of cuts and the variation of edge shape is not significant in this area. Therefore, crest-cut tools act like variable pitch end mill (if there is not linear part at the beginning of the edges) with small pitch variation. According to Figure 5.14, low pitch variations do not affect the process with low natural frequencies, or the effects are only significant in low values of spindle speed.

In order to increase the effect of crest-cut end mills, the cutting conditions are changed, and the width of cut decreased to 0.1 of the tool diameter. As a result, stable cutting depths and the effect of edge shape variation should be increased.

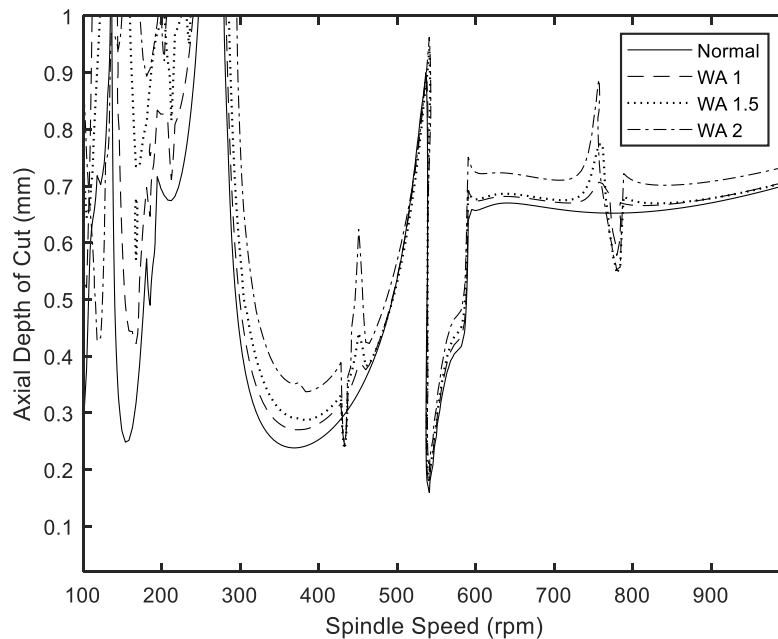


Figure 5.16. Stability lobes for crest-cut end mills with different wave amplitudes (0.1 immersion)

As shown in Figure 5.16, using crest-cut end mills is more significant in the low width of cuts, and we can increase the range of spindle speed for improvement. However, they do not affect all the areas where the robot modes are active.

These results show that in robotic milling, using the crest-cut end mills does not make an advantage for half immersion conditions where the stable depth of cuts is low. By

decreasing the width of cut, we can obtain higher stable depths, and greater part of the tool is engaged in the process. Therefore wavy part of edges can affect the stability diagram. While the affected spindle speed range is not wide enough and we cannot increase the stability limits for all the areas where robot mode is active. To sum up, using crest-cut end mills are effective in robotic milling when the process has low radial depth of cuts (like profiling) and spindle speeds; otherwise, these tools do not have any advantage against normal end mills. It is worth mentioning that all of these results are for the area where robot modes are active; otherwise, all of the results for normal milling in chapter 3 are valid for robotic milling as well.

5.2. Application of Special Tools in Thin Wall Machining

Flexible structure milling is in high demand in the machining sector, especially in the aeronautic and aerospace industries (Yang et al. 2016; Wan, Zhang, and Huang 2013). This part investigates the milling of the highly flexible cantilevered Ti6Al4V plates. This section's results can be used in a variety of industries, including jet engine manufacturers who produce blisks, impellers, and turbine blades using multi-axis milling procedures. The production time of these part are very high and increasing the productivity of these operations results in consuming time and money.

As discussed before, in normal milling, workpiece dynamics are frequently overlooked since their contribution is insignificant in comparison to that of the cutting tool, particularly for long slender end mills (Ioannis Minis et al. 1990; Altıntaş and Budak 1995; E. Budak, Ozturk, and Tunc 2009). Therefore, the flexibility of the end mill is dominant during the roughing process of the thin walls, and the results obtained in the previous sections can be used in this stage. On the other hand, the flexibility of the structure (workpiece) is dominant in the finishing step, and the tool can be assumed rigid (Figure 5.17)(E. Budak and Altıntaş 1998b).

In this section, the effect of using special end mills on the machining of the thin-walls is studied, and the variation of the stability lobe diagrams is investigated.

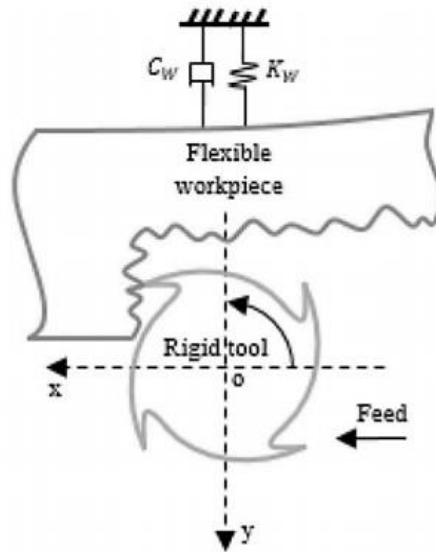


Figure 5.17. Simplified model of the thin wall machining

5.2.1. Case Study: Thin-wall milling

In this section, a thin-wall (cantilever plate) of Ti6Al4V with the dimension of the $150 \times 50 \times 3\text{mm}$ is used in simulations to extract stability lobe diagrams. The results of the FEM analysis, which was done to calculate modal parameters of the thin-wall are shown in Figure 5.18.

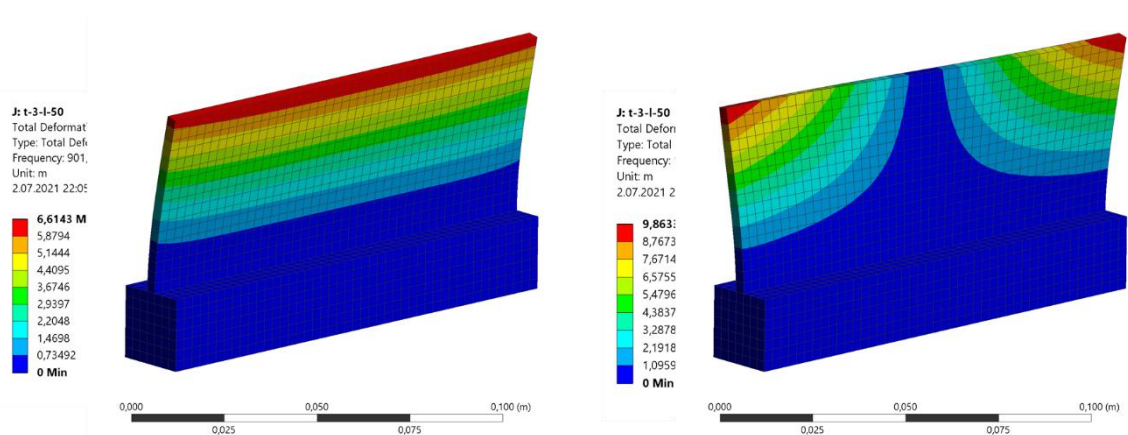


Figure 5.18. FEM results of the modal analysis of the thin-wall a)1st mode b)2nd mode

According to the obtained results by the FEM analysis, modal parameters and FRF of the

thin-wall is obtained in its corner as follow (in the calculation the value of the ζ is assumed as 5%). According to the obtained results, there are two main and dominant mode in the system (Table 5.2).

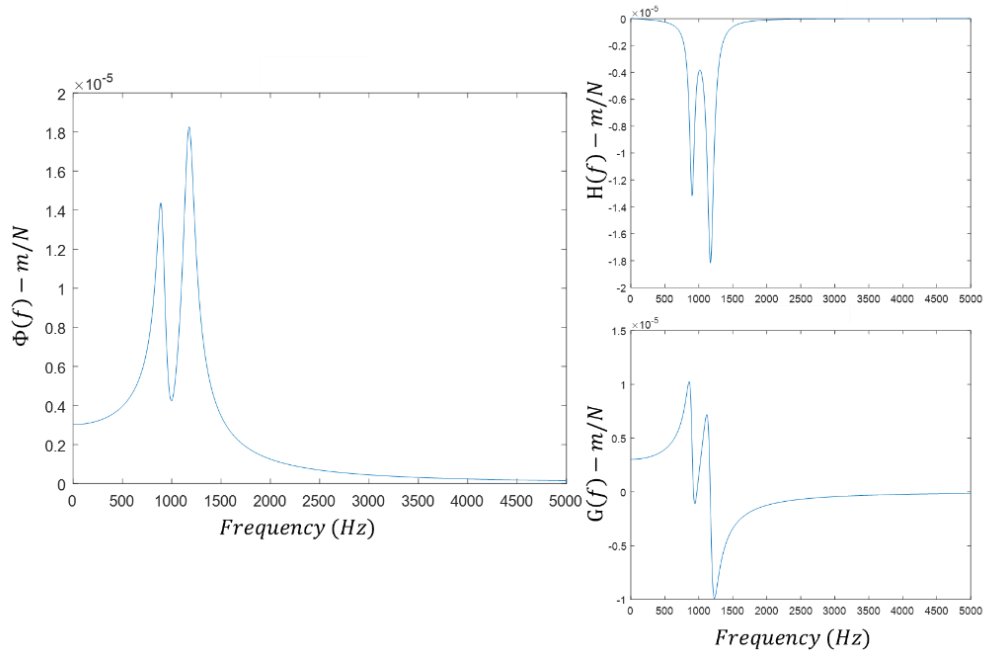


Figure 5.19. Frequency response function of thin-wall and its real and imaginary parts

Table 5.2. Modal parameters of the thin-wall

	ω_n (Hz)	K (N/m)
1st mode	902	8.073e05
2nd mode	1174	5.60e05

The plate is down-milled by a four fluted, 30° helical end mill. 4 different tools whose properties are illustrated in Table 3.3 are used in simulations. The first end mill is a typical end mill. The second and third ones are variable pitch tools optimized for 2700 RPM (85 m/min, which is recommended for cutting of Ti6Al4V) considering the first and second mode of the thin-wall, respectively, using the method presented in (E. Budak 2003a). The last tool is semi-crest-cut end mill which was selected considering the discussions in section 3.5.

Table 5.3. Crest-cut end mill parameters in the chatter test

No.	Type	R_t	N_t	γ	ΔP	w_l	w_a
1	Standard	5 mm	4	30°	-	-	-
3	Semi-crest-cut				-	-	-
4	Variable Pitch				9°	-	-
5	Variable Pitch				7°	2 mm	15 mm

The obtained stability diagram for the standard end mill (Tool 1) is shown in the following figure for each mode of the plate.

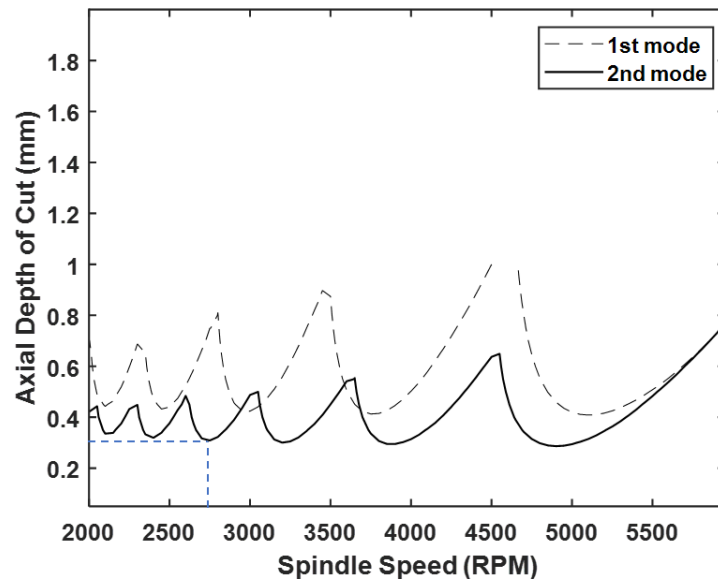


Figure 5.20. Stability diagram for the standard end mill (Tool 1 of Table 3.3)

As shown in Figure 5.20, the second mode is dominant, and according to the diagram, the maximum stable cut using the standard end mill is about 0.3 mm.

In the following figures, the stability of the process using two optimum variable pitch end mills are illustrated. Figures show the stability lobe diagram using optimized tools for the first and second modes at 2700 RPM, respectively.

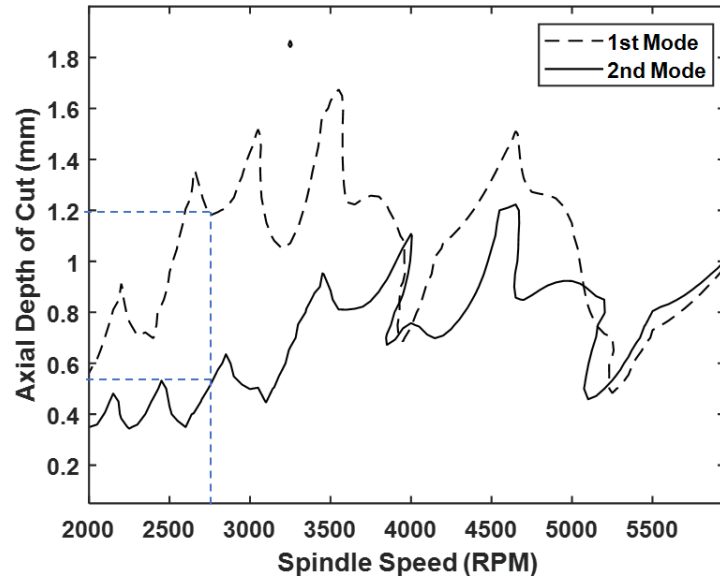


Figure 5.21. Stability diagram for the variable pitch end mill (Tool 2 of Table 3.3)

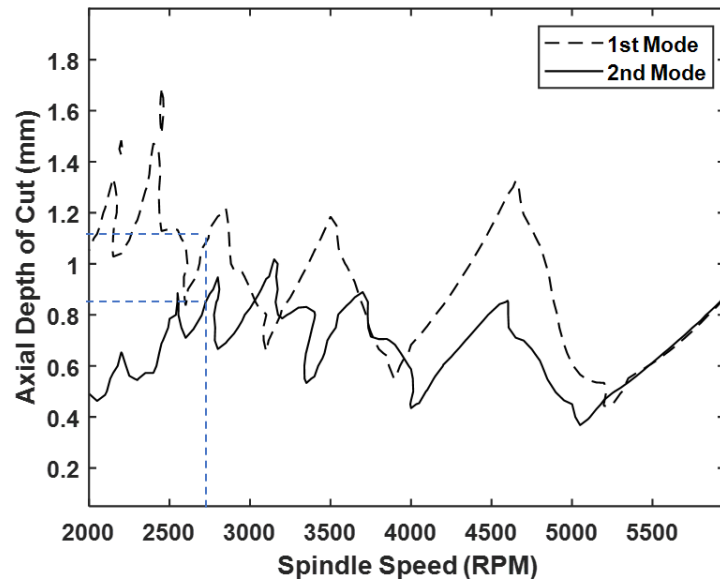


Figure 5.22. Stability diagram for the variable pitch end mill (Tool 3 of Table 3.3)

The results show that the variable pitch tool considering the second mode is much better performance in terms of stability. Because the second mode, as demonstrated in Figures 5.19 and 5.20, is the dominant mode in the corner of the thin-wall plate. The stability limit using Tool 3 is about 0.85 mm.

Figures 5.24 and 5.25 show the stability limits using semi crest-cut tool (Tool 4) considering both modes.

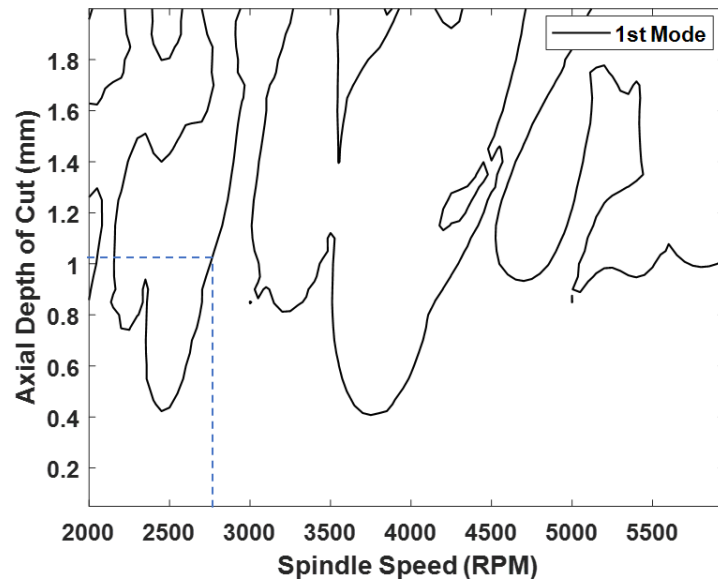


Figure 5.23. Stability diagram for the semi-crest-cut tool (Tool 4) – 1st mode

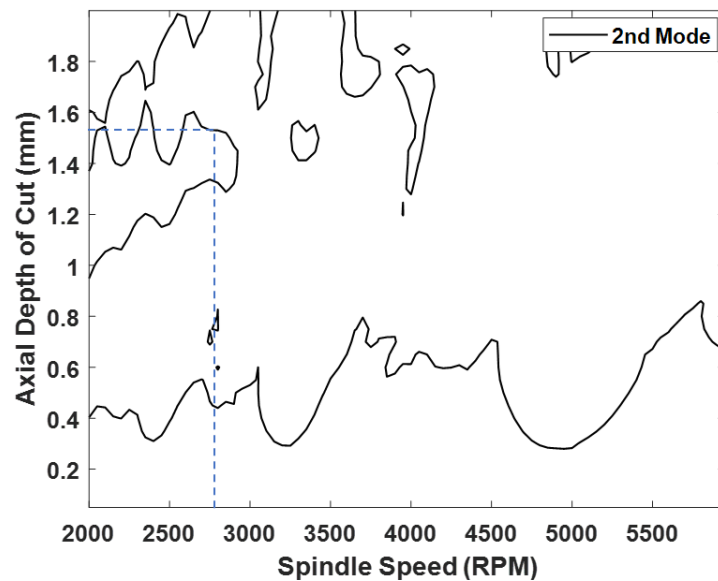


Figure 5.24. Stability diagram for the semi-crest-cut tool (Tool 4) – 2nd mode

The results show that, in spite of other tools, the first mode is the dominant mode for stability in the study range. The stability lobe diagrams at each speed have multiple margins, and the stability condition changes after each margin. This interesting observation motivates us to look into the results in a much wider range. The obtained

stability lobe diagrams shows the great potential of using semi-crest-cut end mills in thin-wall machining.

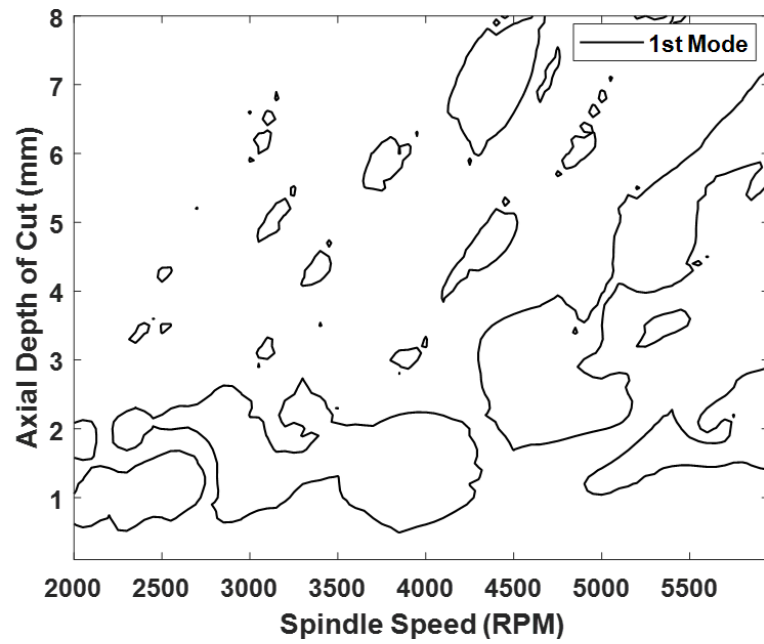


Figure 5.25. Stability diagram for the semi-crest-cut tool (Tool 4) – 1st mode

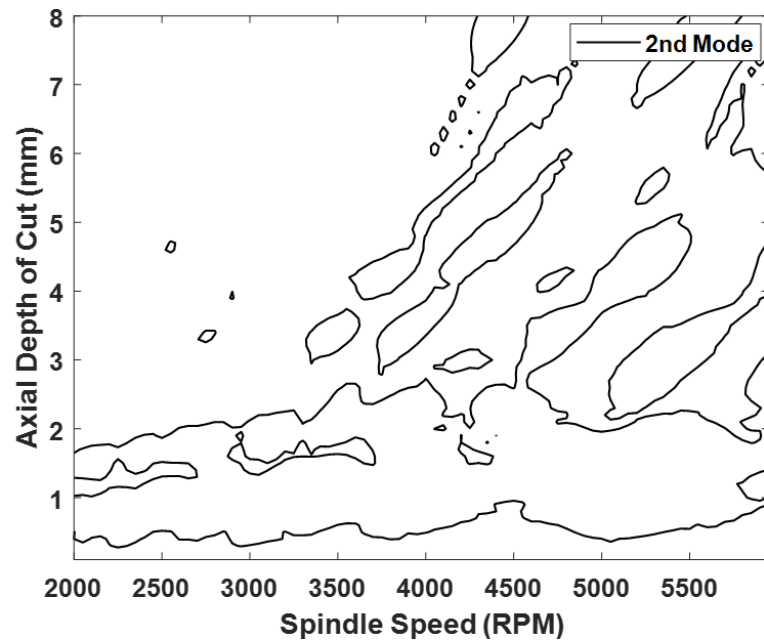


Figure 5.26. Stability diagram for the semi-crest-cut tool (Tool 4) – 2nd mode

The process is almost stable for depths between 2mm and 8mm at 2000 RPM – 3500 RPM, according to the obtained results, and the process can be done in all of these areas

from a stability viewpoint. The maximum axial depth of the cut can, however, be limited by machinability, cutting forces, tool, and workpiece deflections.

The main reason for this improvement is that by increasing the axial depth of cut, different parts of the wavy edges are engaged in the cut, effectively disrupting the regenerative chatter mechanism.

5.3. Application of Serrated End Mills on Turn-Milling Process

The geometric models of serrated tools were detailed in-depth in chapter 4, and the mechanics of these tools were investigated for the 3-axis milling process. The geometry and mechanics of the turn-milling process with standard tools were examined in detail by Berenji et al. (Rahimzadeh Berenji et al. 2019). These two models are combined in order to predict the cutting forces of the turn-milling process with serrated tools. In the following parts, the necessary changes in the formulation of chapter 4 will be discussed.

5.3.1. Force Calculation of Turn-Milling with Serrated Tools

As discussed in chapter 4, chip thickness calculation has great importance in the prediction of the cutting forces, and its calculation should be modified considering the kinematics of the turn-milling process. The interface between the tool and the workpiece is identified in this approach, and this interface is accepted as the chip area. The element-shaped discs mentioned in the preceding sections are used to split these chip regions into parts. The method described in 4.2.1 is used to divide chip areas with some modifications. Equation (4.32) is modified as follow considering the formulation in (Rahimzadeh Berenji et al. 2019):

$$W(i, j, \varphi_{ij}) = \max \left\{ \min \left\{ R_{im} + \frac{k(2\pi n_w)^0}{n_t N \cos(\beta) \cos(\theta_x)} \cdot (R_w - a_p + i \cdot dz) \right\} \right\} \quad (5.15)$$

$$m = \begin{cases} k - j & \text{if } k - j > 0 \\ k - j + M & \text{if } k - j \leq 0 \end{cases} \quad k = 1, 2, \dots, M$$

Moreover, the depth of cut is changed in each angular position, and it should be calculated in each angular step:

$$a_{pr}(\varphi_{ij}) = \sqrt{R_w^2 - (R_t \sin(\varphi_{ij} + \theta_x) + e)^2} - (R_w - a_p) \quad (5.16)$$

Then, for each element at each axial height, the differential forces are computed.

$$\begin{aligned} dF_a(i, j, \varphi) &= q(\varphi_{ij}) \cdot g(\varphi_{ij}) [K_{ae} + K_{ac}(i, j) h_{ij}(\varphi_{ij})] dz \\ dF_r(i, j, \varphi) &= q(\varphi_{ij}) \cdot g(\varphi_{ij}) [K_{re} + K_{rc}(i, j) h_{ij}(\varphi_{ij})] dz \\ dF_t(i, j, \varphi) &= q(\varphi_{ij}) \cdot g(\varphi_{ij}) [K_{te} + K_{tc}(i, j) h_{ij}(\varphi_{ij})] dz \end{aligned} \quad (5.17)$$

The $g(\varphi_{ij})$ function in the following formula returns 1 when the element is between start and exit angle, and it is 0 when it is not cut. At each element's angular location, the $q(\varphi_{ij})$ function takes the values 1 when cutting and 0 when not cutting, according to the permissible chip height stated in Equation (5.16). In the next step, these differential forces are transferred to tool coordinates, and the total forces can be obtained by summing up differential forces in tool coordinate (Equations (4.36) and (4.37)).

5.3.2. Experimental Verification

Experiments were carried out on the Mori Seiki NTX2000 CNC machine using a rotary dynamometer to validate the proposed force model of turn-milling with serrated end mills (Figure 5.27). The tool and workpiece material used in the force measurement experiments was carbide and AL7075, respectively. The serration type of the tool was a trapezoid, and the geometrical parameters are indicated in Table 5.4.



Figure 5.27. The experiment setup for validating the force model of turn-milling with serrated tools

Table 5.4. The geometrical parameters of the end mill used in experiments

Type of Tool	Tool Dia.	Cutting Angles	Serration Type	Serration Wave Parameters
Endmill	16mm	$\alpha = 5^\circ$ $\lambda = 38^\circ$	Trapezoidal	$L1 = 0.7, L2 = 0.3$ $A = 0.5, \alpha = \beta = 30$ $R1 = R2 = R3 = R4 = 0.3$

Experiments at similar cutting speeds and different eccentricity and feed rates were performed to validate the proposed model (Table 5.5). The proposed force model and the experiments in the Figures have a high degree of agreement. At various eccentricity and feed values, the proposed model yields a satisfactory fit.

Table 5.5. Cutting parameters of experiments

Test	D_t	D_w	V_c	n_t	n_w	a_w	F	e
1	16 mm	122 mm	200 m/min	3979 RPM	8 RPM	3 mm	24 mm/min	4 mm
2						3 mm	24 mm/min	2 mm
3						6 mm	48 mm/min	4 mm

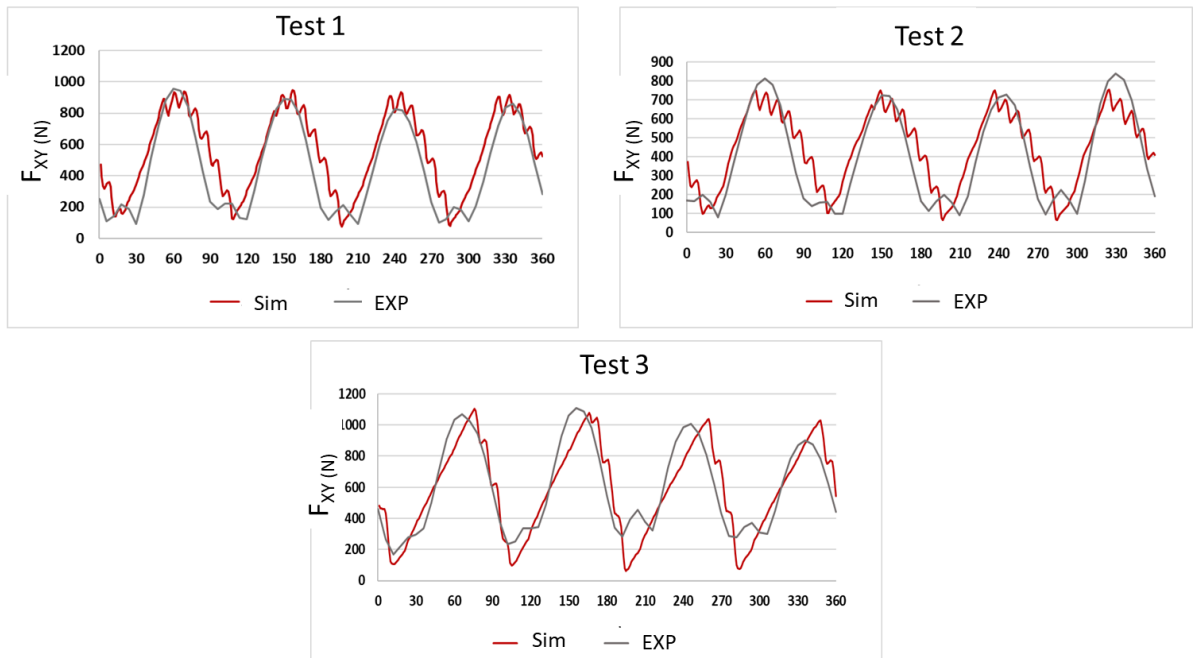


Figure 5.28. Comparison between test results and simulations

5.4. Conclusions

In this chapter, the application of the special end mills and their effectiveness in robotic milling, thin-wall machining, and turn-milling process are investigated. The specific contributions and conclusions are listed in the following.

- Variable pitch tools have a positive impact on the robotic milling process, increasing stability limits and productivity. However, because of the low natural frequency of the robots' structure and manufacturing limitations for variable pitch tools, these tools are only effective at low spindle speeds. As a result, in operations involving tools with larger diameters (like face milling), the use of the tools is recommended. This recommendation is based on the fact that in constant cutting speed, larger diameter tools correspond to lower spindle speeds; additionally, as the tool diameter increases, the manufacturing limitation of variable pitch tools decreases.
- Pitch variations produced by crest cut end mills are insufficient to affect the stability limit of the robotic milling process due to the low natural frequencies of the robot's structure. As a result, these tools are not recommended to use in robotic milling to diminish chatter vibrations at low frequencies.
- Semi-crest-cut tools can increase the stability limits in the milling of thin walls. These tools introduce new stable areas after unstable axial heights by engaging the larger parts of the wavy edges in cut, and this phenomenon results in disrupting the chatter mechanism.
- Turn-milling forces with serrated tools are predicted and confirmed with experimental results. Considering cutter-workpiece engagement and local cutting force coefficients, accurate cutting force predictions are obtained.

References

- Ahn, Chang Wook. 2006. *Practical Genetic Algorithms. Studies in Computational Intelligence*. Vol. 18. John Wiley & Sons. https://doi.org/10.1007/11543138_2.
- Aksu, Burak, Ceren Çelebi, and Erhan Budak. 2016. “An Experimental Investigation of Oblique Cutting Mechanics.” *Machining Science and Technology* 20 (3): 495–521. <https://doi.org/10.1080/10910344.2016.1196458>.
- Altıntaş, Y., and E. Budak. 1995. “Analytical Prediction of Stability Lobes in Milling.” *CIRP Annals - Manufacturing Technology* 44 (1): 357–62. [https://doi.org/10.1016/S0007-8506\(07\)62342-7](https://doi.org/10.1016/S0007-8506(07)62342-7).
- Altıntaş, Y., S. Engin, and E. Budak. 1999. “Analytical Stability Prediction and Design of Variable Pitch Cutters.” *Journal of Manufacturing Science and Engineering, Transactions of the ASME* 121 (2): 173–78. <https://doi.org/10.1115/1.2831201>.
- Altintas, Y., A. Spence, and J. Tlustý. 1991. “End Milling Force Algorithms for CAD Systems.” *CIRP Annals - Manufacturing Technology* 40 (1): 31–34. [https://doi.org/10.1016/S0007-8506\(07\)61927-1](https://doi.org/10.1016/S0007-8506(07)61927-1).
- Armarego, E. J.A., and C. J. Epp. 1970. “An Investigation of Zero Helix Peripheral Up-Milling.” *International Journal of Machine Tool Design and Research* 10 (2): 273–91. [https://doi.org/10.1016/0020-7357\(70\)90011-9](https://doi.org/10.1016/0020-7357(70)90011-9).
- Armarego, E. J.A., and R. C. Whitfield. 1985. “Computer Based Modelling of Popular Machining Operations for Force and Power Prediction.” *CIRP Annals - Manufacturing Technology* 34 (1): 65–69. [https://doi.org/10.1016/S0007-8506\(07\)61725-9](https://doi.org/10.1016/S0007-8506(07)61725-9).
- Armarego, E J A, and Robert Hallows Brown. 1969. “The Machining of Metals.” *Wear* 14 (4): 305. [https://doi.org/10.1016/0043-1648\(69\)90131-8](https://doi.org/10.1016/0043-1648(69)90131-8).
- Arnold, R. N. 1946. “Cutting Tools Research: Report of Subcommittee on Carbide Tools: The Mechanism of Tool Vibration in the Cutting of Steel.” *Proceedings of the Institution of Mechanical Engineers* 154 (1): 261–84. https://doi.org/10.1243/pime_proc_1946_154_037_02.
- Astakhov, Viktor P. 1998. “Metal Cutting Mechanics.” *Metal Cutting Mechanics*.

- <https://doi.org/10.1201/9781466571778>.
- Bellen, Alfredo, and Marino Zennaro. 2007. *Numerical Methods for Delay Differential Equations*. Numerical Methods for Delay Differential Equations. Oxford university press. <https://doi.org/10.1093/acprof:oso/9780198506546.001.0001>.
- Brown, R. H., and E. J.A. Armarego. 1964. "Oblique Machining with a Single Cutting Edge." *International Journal of Machine Tool Design and Research* 4 (1): 9–25. [https://doi.org/10.1016/0020-7357\(64\)90006-X](https://doi.org/10.1016/0020-7357(64)90006-X).
- Budak, E. 2003a. "An Analytical Design Method for Milling Cutters with Nonconstant Pitch to Increase Stability, Part 2: Application." *Journal of Manufacturing Science and Engineering, Transactions of the ASME* 125 (1): 35–38. <https://doi.org/10.1115/1.1536656>.
- . 2003b. "An Analytical Design Method for Milling Cutters with Nonconstant Pitch to Increase Stability, Part I: Theory." *Journal of Manufacturing Science and Engineering, Transactions of the ASME* 125 (1): 29–34. <https://doi.org/10.1115/1.1536655>.
- Budak, E., and Y. Altıntaş. 1998a. "Analytical Prediction of Chatter Stability in Milling—Part I: General Formulation." *Journal of Dynamic Systems, Measurement and Control, Transactions of the ASME* 120 (1): 22–30. <https://doi.org/10.1115/1.2801317>.
- . 1998b. "Analytical Prediction of Chatter Stability in Milling—Part II: Application of the General Formulation to Common Milling Systems." *Journal of Dynamic Systems, Measurement and Control, Transactions of the ASME* 120 (1): 31–36. <https://doi.org/10.1115/1.2801318>.
- Budak, E., Y. Altıntaş, and E. J.A. Armarego. 1996. "Prediction of Milling Force Coefficients from Orthogonal Cutting Data." *Journal of Manufacturing Science and Engineering, Transactions of the ASME* 118 (2): 216–24. <https://doi.org/10.1115/1.2831014>.
- Budak, E., E. Ozturk, and L. T. Tunc. 2009. "Modeling and Simulation of 5-Axis Milling Processes." *CIRP Annals - Manufacturing Technology* 58 (1): 347–50. <https://doi.org/10.1016/j.cirp.2009.03.044>.
- Budak, E, and L Kops. 2000. "Improving Productivity and Part Quality in Milling of Titanium Based Impellers by Chatter Suppression and Force Control." *CIRP Annals* 49 (1): 31–36.

- Budak, Erhan, Emre Ozlu, Hayri Bakioglu, and Zahra Barzegar. 2016. "Thermo-Mechanical Modeling of the Third Deformation Zone in Machining for Prediction of Cutting Forces." *CIRP Annals - Manufacturing Technology* 65 (1): 121–24. <https://doi.org/10.1016/j.cirp.2016.04.110>.
- Budak, Erhan, L Taner Tunç, Salih Alan, and H Nevzat Özgüven. 2012. "Prediction of Workpiece Dynamics and Its Effects on Chatter Stability in Milling." *CIRP Annals* 61 (1): 339–42.
- Campomanes, Marc L. 202AD. "Kinematics and Dynamics of Milling with Roughing Tools." *Metal Cutting and High Speed Machining*, 129–40.
- Comak, Alptunc, and Erhan Budak. 2017. "Modeling Dynamics and Stability of Variable Pitch and Helix Milling Tools for Development of a Design Method to Maximize Chatter Stability." *Precision Engineering* 47: 459–68. <https://doi.org/10.1016/j.precisioneng.2016.09.021>.
- Cordes, Marcel, Wolfgang Hintze, and Yusuf Altintas. 2019. "Chatter Stability in Robotic Milling." *Robotics and Computer-Integrated Manufacturing* 55: 11–18. <https://doi.org/10.1016/j.rcim.2018.07.004>.
- Devor, R. E., W. A. Kline, and W. J. Zdeblick. 1980. "Mechanistic Model for the Force System in End Milling With Application To Machining Airframe Structures." In *Manufacturing Engineering Transactions*, 297–230. Dearborn: Society of Manufacturing Engineers.
- Diekmann, Odo, Stephan A Van Gils, Sjoerd M V Lunel, and Hans-Otto Walther. 2012. *Delay Equations: Functional-, Complex-, and Nonlinear Analysis*. Vol. 110. Springer Science & Business Media.
- Dombovari, Zoltan, Yusuf Altintas, and Gabor Stepan. 2010. "The Effect of Serration on Mechanics and Stability of Milling Cutters." *International Journal of Machine Tools and Manufacture* 50 (6): 511–20. <https://doi.org/10.1016/j.ijmactools.2010.03.006>.
- Dombovari, Zoltan, and Gabor Stepan. 2012. "The Effect of Helix Angle Variation on Milling Stability." *Journal of Manufacturing Science and Engineering, Transactions of the ASME* 134 (5): 51015–16. <https://doi.org/10.1115/1.4007466>.
- Engin, S., and Y. Altintas. 2001. "Mechanics and Dynamics of General Milling Cutters. Part II: Inserted Cutters." *International Journal of Machine Tools and Manufacture* 41 (15): 2213–31. [https://doi.org/10.1016/S0890-6955\(01\)00046-3](https://doi.org/10.1016/S0890-6955(01)00046-3).

- Fu, H. J., R. E. DeVor, and S. G. Kapoor. 1984. "A Mechanistic Model for the Prediction of the Force System in Face Milling Operations." *Journal of Manufacturing Science and Engineering, Transactions of the ASME* 106 (1): 81–88. <https://doi.org/10.1115/1.3185915>.
- Gonul, Bora, Omer Faruk Sapmaz, and Lutfi Taner Tunc. 2019. "Improved Stable Conditions in Robotic Milling by Kinematic Redundancy." *Procedia CIRP* 82: 485–90. <https://doi.org/10.1016/j.procir.2019.04.334>.
- Grabowski, R., B. Denkena, and J. Köhler. 2014. "Prediction of Process Forces and Stability of End Mills with Complex Geometries." *Procedia CIRP* 14: 119–24. <https://doi.org/10.1016/j.procir.2014.03.101>.
- Hahn, R.S. 1953. "Metal-Cutting Chatter and Its Elimination." *Trans. ASME* 75 (6): 1073. <http://scholar.google.com/scholar?hl=en&btnG=Search&q=intitle:Metal+Cutting+Chatter+and+Its+Elimination#0>.
- Hastings, W. F., P. Mathew, and P. L. Oxley. 1980. "Machining Theory for Predicting Chip Geometry, Cutting Forces Etc. From Work Material Properties and Cutting Conditions." *Proceedings of The Royal Society of London, Series A: Mathematical and Physical Sciences* 371 (1747): 569–87. <https://doi.org/10.1098/rspa.1980.0097>.
- Hayasaka, Takehiro, Atsushi Ito, and Eiji Shamoto. 2017. "Generalized Design Method of Highly-Variied-Helix End Mills for Suppression of Regenerative Chatter in Peripheral Milling." *Precision Engineering* 48: 45–59. <https://doi.org/10.1016/j.precisioneng.2016.11.004>.
- Hosseini, A., B. Moetakef-Imani, and H. A. Kishawy. 2011. "Mechanistic Modelling for Cutting with Serrated End Mills - A Parametric Representation Approachg." *Proceedings of the Institution of Mechanical Engineers, Part B: Journal of Engineering Manufacture* 225 (7): 1019–32. <https://doi.org/10.1177/2041297510393522>.
- Iglesias, Alex, Zoltan Dombovari, German Gonzalez, Jokin Munoa, and Gabor Stepan. 2019. "Optimum Selection of Variable Pitch for Chatter Suppression in Face Milling Operations." *Materials* 12 (1): 112.
- Inspurger, Tamas. 2010. "Full-Discretization and Semi-Discretization for Milling Stability Prediction: Some Comments." *International Journal of Machine Tools and Manufacture* 50 (7): 658–62. <https://doi.org/10.1016/j.ijmactools.2010.03.010>.
- Inspurger, Tamás, and Gábor Stépán. 2002. "Semi-Discretization Method for Delayed

- Systems.” *International Journal for Numerical Methods in Engineering* 55 (5): 503–18. <https://doi.org/10.1002/nme.505>.
- . 2004. “Updated Semi-Discretization Method for Periodic Delay-Differential Equations with Discrete Delay.” *International Journal for Numerical Methods in Engineering* 61 (1): 117–41. <https://doi.org/10.1002/nme.1061>.
- . 2011. *Semi-Discretization for Time-Delay Systems: Stability and Engineering Applications. Applied Mathematical Sciences (Switzerland)*. 1st ed. Vol. 178. Springer-Verlag New York. <https://doi.org/10.1007/978-1-4614-0335-7>.
- Junz Wang, J. J., and C. S. Yang. 2003. “Angle and Frequency Domain Force Models for a Roughing End Mill with a Sinusoidal Edge Profile.” *International Journal of Machine Tools and Manufacture* 43 (14): 1509–20. [https://doi.org/10.1016/S0890-6955\(03\)00163-9](https://doi.org/10.1016/S0890-6955(03)00163-9).
- Kahles, J F. 1987. “Machinability Data Requirements for Advanced Machining Systems.” *CIRP Ann.* 36 (2): 523–29.
- Kline, W. A., R. E. DeVor, and J. R. Lindberg. 1982. “The Prediction of Cutting Forces in End Milling with Application to Cornering Cuts.” *International Journal of Machine Tool Design and Research* 22 (1): 7–22. [https://doi.org/10.1016/0020-7357\(82\)90016-6](https://doi.org/10.1016/0020-7357(82)90016-6).
- Knight, Winston A., and Geoffrey Boothroyd. 2019. *Fundamentals of Metal Machining and Machine Tools. Fundamentals of Metal Machining and Machine Tools*. Vol. 28. Crc Press. <https://doi.org/10.1201/9780429114243>.
- Koca, R., and E. Budak. 2013. “Optimization of Serrated End Mills for Reduced Cutting Energy and Higher Stability.” *Procedia CIRP* 8: 570–75. <https://doi.org/10.1016/j.procir.2013.06.152>.
- Koca, R. 2012. “Mechanics, Dynamics and Optimization of Special End Mills.” *Faculty of Engineering and Natural Sciences*. Istanbul/TURKEY: M. Sc. Thesis, Sabanci University.
- Koenigsberger, F., and A. J.P. Sabberwal. 1961. “An Investigation into the Cutting Force Pulsations during Milling Operations.” *International Journal of Machine Tool Design and Research* 1 (1–2): 15–33. [https://doi.org/10.1016/0020-7357\(61\)90041-5](https://doi.org/10.1016/0020-7357(61)90041-5).
- Koenigsberger, F, and J Tlustý. 1967. “Machine Tool Structure-Vol. 1: Stability Against Chatter.” Pergamon Press.

- Lazoglu, I., and S. Y. Liang. 1997. "Analytical Modeling of Force System in Ball-End Milling." *Machining Science and Technology* 1 (2): 219–34. <https://doi.org/10.1080/10940349708945648>.
- Lee, P., and Y. Altıntaş. 1996. "Prediction of Ball-End Milling Forces from Orthogonal Cutting Data." *International Journal of Machine Tools and Manufacture* 36 (9): 1059–72. [https://doi.org/10.1016/0890-6955\(95\)00081-X](https://doi.org/10.1016/0890-6955(95)00081-X).
- Merchant, M. Eugene. 1944. "Basic Mechanics of the Metal-Cutting Process." *Journal of Applied Mechanics* 11 (3): A168–75. <https://doi.org/10.1115/1.4009380>.
- Merdol, S. D., and Y. Altintas. 2004. "Mechanics and Dynamics of Serrated Cylindrical and Tapered End Mills." *Journal of Manufacturing Science and Engineering, Transactions of the ASME* 126 (2): 317–26. <https://doi.org/10.1115/1.1644552>.
- Merdol, S. Doruk, and Yusuf Altintas. 2002. "Mechanics and Dynamics of Serrated End Mills." *ASME International Mechanical Engineering Congress and Exposition, Proceedings*. New Orleans: IMECE2002. <https://doi.org/10.1115/IMECE2002-39114>.
- Michiels, Wim, and Silviu-Iulian Niculescu. 2007. *Stability and Stabilization of Time-Delay Systems: An Eigenvalue-Based Approach*. SIAM.
- Minis, I., and R. Yanushevsky. 1993. "A New Theoretical Approach for the Prediction of Machine Tool Chatter in Milling." *Journal of Manufacturing Science and Engineering, Transactions of the ASME* 115 (1): 1–8. <https://doi.org/10.1115/1.2901633>.
- Minis, Ioannis, Rafael Yanushevsky, Abel Tembo, and Robert Hocken. 1990. "Analysis of Linear and Nonlinear Chatter in Milling." *CIRP Annals - Manufacturing Technology* 39 (1): 459–62. [https://doi.org/10.1016/S0007-8506\(07\)61096-8](https://doi.org/10.1016/S0007-8506(07)61096-8).
- No, Timothy, Michael Gomez, Ryan Copenhaver, Juan Uribe Perez, Christopher Tyler, and Tony L. Schmitz. 2019. "Force and Stability Modeling for Non-Standard Edge Geometry Endmills." *Journal of Manufacturing Science and Engineering, Transactions of the ASME* 141 (12). <https://doi.org/10.1115/1.4045057>.
- Olgac, Nejat, and Rifat Sipahi. 2007. "Dynamics and Stability of Variable-Pitch Milling." *JVC/Journal of Vibration and Control* 13 (7): 1031–43. <https://doi.org/10.1177/1077546307078754>.
- Opitz, H, E U Dregger, and H Roese. 1966. "Improvement of the Dynamic Stability of the Milling Process by Irregular Tooth Pitch." In *Proceedings of the Adv. MTDR*

Conference, 7:213.

- Ortín, Tomás. 2010. *Differential Geometry. Gravity and Strings*. Dover Publications. <https://doi.org/10.1017/cbo9780511616563.003>.
- Ozlu, Emre, Erhan Budak, and A Molinari. 2009. “Analytical and Experimental Investigation of Rake Contact and Friction Behavior in Metal Cutting.” *International Journal of Machine Tools and Manufacture* 49 (11): 865–75. <https://doi.org/https://doi.org/10.1016/j.ijmactools.2009.05.005>.
- Özlü, Emre, Arash Ebrahimi Araghizad, and Erhan Budak. 2020. “Broaching Tool Design through Force Modelling and Process Simulation.” *CIRP Annals* 69 (1): 53–56. <https://doi.org/10.1016/j.cirp.2020.04.035>.
- Rahimzadeh Berenji, K., Umut Karagüzel, Emre Özlü, and E. Budak. 2019. “Effects of Turn-Milling Conditions on Chip Formation and Surface Finish.” *CIRP Annals* 68 (1): 113–16. <https://doi.org/10.1016/j.cirp.2019.04.067>.
- Sabberwal, A.J.P. 1961. “Chip Section and Cutting Force during the Milling Operation.” *Annals of CIRP* 10 (3): 197–203.
- Sanz, Markel, Alex Iglesias, Jokin Munoa, and Zoltan Dombovari. 2020. “The Effect of Geometry on Harmonically Varied Helix Milling Tools.” *Journal of Manufacturing Science and Engineering, Transactions of the ASME* 142 (7). <https://doi.org/10.1115/1.4046901>.
- Shirase, Keiichi, Masaki Sano, Masatoshi Hirao, and Takeshi Yasui. 1999. “Analysis and Suppression of Chatter Vibration in End Milling Operation (1st Report) - Analysis of Chatter Vibration for Irregular Tooth Pitch End Mill Using Time Domain Cutting Simulation.” *Seimitsu Kogaku Kaishi/Journal of the Japan Society for Precision Engineering* 65 (3): 465–69.
- Sims, N. D., B. Mann, and S. Huyanan. 2008. “Analytical Prediction of Chatter Stability for Variable Pitch and Variable Helix Milling Tools.” *Journal of Sound and Vibration* 317 (3–5): 664–86. <https://doi.org/10.1016/j.jsv.2008.03.045>.
- Slavicek, Jan. 1965. “The Effect of Irregular Tooth Pitch on Stability of Milling.” In *Proceedings of the 6th MTDR Conference*, 1:15–22.
- Taylor, Fred W. 1907. *The Art of Cutting Metals. Scientific American*. Vol. 63. American society of mechanical engineers. <https://doi.org/10.1038/scientificamerican01121907-25942supp>.
- Tehranizadeh, Faraz, and Erhan Budak. 2017. “Design of Serrated End Mills for

- Improved Productivity.” In *Procedia CIRP*, 58:493–98.
<https://doi.org/10.1016/j.procir.2017.03.256>.
- Tehranizadeh, Faraz, Recep Koca, and Erhan Budak. 2019. “Investigating Effects of Serration Geometry on Milling Forces and Chatter Stability for Their Optimal Selection.” *International Journal of Machine Tools and Manufacture* 144.
<https://doi.org/10.1016/j.ijmactools.2019.103425>.
- Thusty, J., and F. Ismail. 1981. “Special Aspects of Chatter in Milling.” *American Society of Mechanical Engineers (Paper)* 105: 24–32.
- Thusty, J., F. Ismail, and W. Zaton. 1983. “Use of Special Milling Cutters Against Chatter.” *Manufacturing Engineering Transactions*. University of Wisconsin : Technical Report.
- Thusty, J., and P. MacNeil. 1975. “Dynamics of Cutting Forces in End Milling.” *Ann CIRP* 24 (1): 21–25.
- Thusty, J, F Ismail, and W Zaton. 1982. “Milling Cutters with Irregular Pitch.” McMaster Engineering: Technical Report.
- Thusty, J, and M Polacek. 1963. “The Stability of the Machine Tool Against Self-Excited Vibration in Machining.” *ASME Int. Res. in Production* 1: 465–74.
<https://doi.org/citeulike-article-id:4000165>.
- Tobias, Stephen Albert. 1965. *Machine-Tool Vibration*. J. Wiley.
- Turner, Sam, Doruk Merdol, Yusuf Altintas, and Keith Ridgway. 2007. “Modelling of the Stability of Variable Helix End Mills.” *International Journal of Machine Tools and Manufacture* 47 (9): 1410–16.
<https://doi.org/10.1016/j.ijmactools.2006.08.028>.
- VANHERCK, P. 1968. “Increasing Milling Machine Productivity By Use of Cutters With Non-Constant Cutting-Edge Pitch.” *Advances in Machine Tool Design and Research 1967*. <https://doi.org/10.1016/b978-0-08-012629-6.50017-1>.
- Wan, Xiao Jin, Yan Zhang, and Xin Da Huang. 2013. “Investigation of Influence of Fixture Layout on Dynamic Response of Thin-Wall Multi-Framed Work-Piece in Machining.” *International Journal of Machine Tools and Manufacture* 75: 87–99.
<https://doi.org/10.1016/j.ijmactools.2013.09.008>.
- Yang, Yun, Wei Hong Zhang, Ying Chao Ma, and Min Wan. 2016. “Chatter Prediction for the Peripheral Milling of Thin-Walled Workpieces with Curved Surfaces.” *International Journal of Machine Tools and Manufacture* 109: 36–48.

<https://doi.org/10.1016/j.ijmachtools.2016.07.002>.

Zhang, Z., L. Zheng, Z. Li, D. Liu, L. Zhang, and B. Zhang. 2003. "A Cutting Force Model for a Waved-Edge End Milling Cutter." *International Journal of Advanced Manufacturing Technology* 21 (6): 403–10. <https://doi.org/10.1007/s001700300047>.